TOWARD ACTIVE CONTROL OF NOISE
FROM HOT SUPERSONIC JETS

Quarterly Progress Report No. 5

1 AUG 2012 – 31 OCTOBER 2012

Nathan E. Murray (PI)
Aeroacoustics Research Group
National Center for Physical Acoustics
University of Mississippi
University, MS 38677
(662) 915-3190
nmurray@olemiss.edu

Contract: N00014-11-1-0752

Executive Summary

Enhancements to the PIV seeding system in the NCPA Anechoic Jet Laboratory were completed and standard 3-component PIV measurements were acquired on the jet centerline. Auburn U. collaborators traveled to U. Miss. to support a Plenopic PIV measurement of the jet. UT Austin collaborators submitted an abstract to the 2013 AIAA Aeroacoustics meeting which discusses our efforts to evaluate noise source indicators. Also, the UT Austin collaborators submitted a manuscript to *J. Fluid Mech.* on nonlinear distortion of the acoustic waveforms – work that was largely completed during year one. Finally, CRAFT Tech made significant progress on completing the LES simulations of the 4 jet configurations of interest. The time resolved data is being made available to the group for development of noise source indicator calculations. Also, CRAFT Tech has made advancements in their beamforming framework in the computational domain. Finally, NCPA hosted a site visit from stakeholders including B. Henderson (ONR), J. Bridges (NASA), and A. Aubert (NAVAIR). The visit included a summary presentation of year one accomplishments, an update on current program status and results, and a tour of the NCPA facilities.

November 14, 2012

Contents

1 Project Objectives and Status

1.1 Objectives Overview

Overall, the research effort has two primary objectives:

1. Acquire high-fidelity, time-resolved, synchronous flow-field and acoustic data on a laboratory scale, hot, supersonic, shock-containing jet.
2. Advance the understanding of noise source indicators for these complex flows.

1.2 Project Status

During the first year of the program the focus was largely on the first of the primary objectives. This involved a joint experimental effort support by all the collaborators as well as simultaneous development of a computational simulation of the jet conditions used in the experiment. As the program now enters year two, the focus shifts more to the second primary objective while efforts to acquire data are ongoing.

The year one efforts resulted in several accomplishments. Cold jet Mach 3 experiments were conducted in the UT Austin facility allowing mapping of the acoustic field out to 140 jet diameters. This led to a greater understanding of the effects of nonlinear distortion in supersonic jet noise. The results have been submitted to *J. Fluid Mech.* for publication (see Appendix G). In the NCPA Anechoic Jet Facility, characteristic measurements were made for the hot, shock-containing jet including single point pitot probe profiles, near-field pressure,

and far-field ($55D_j$) acoustics. The experimental work of the first year culminated in a joint experiment that synchronized the near/far-field acoustic data with flow field measurements acquired using Auburn's MHz PIV system. However, this first experiment uncovered deficiencies in the PIV seeding system and the high-speed camera that rendered the majority of the data unusable. These deficiencies have been addressed and improvements will enable a success in the year two experiments. In parallel with the experimental efforts, a computational simulation was performed by CRAFT Tech that matched the nozzle geometry, initial conditions, and boundary conditions of the laboratory experiment. No other data from the experiment was provided to the simulation allowing for a "blind" comparison between the two. Comparisons of the jet total pressure profiles and far field acoustic pressures have shown very good agreement. In addition to the simulation itself, the framework for deploying a beamforming array in the computational domain was established and will be used as an array design tool for future experimental measurements.

An updated project chart is shown in Figure 1 which details the WBS items from the SOW and the completion percentages as of the end of the reporting period. Key items of note are highlighted in the chart. First, the end date for WBS 1.4 has been extended to the end of the project period based on the exploratory nature of the research into noise indicators. Second, the temperature profiles, WBS 2.1.4, were not completed during year one due to the temperature probe failing in the hot jet. We are planning to improve the design of the probe and perform these measurements during year 2. Efforts into documenting the experimental uncertainties, WBS 3.3, have fallen behind schedule and will receive greater focus to bring this task back on schedule.

2 Activity for Current Reporting Period

During the current reporting period, the focus has been on (a) initiating the exploration of noise source indicators using the data from the computational simulation, (b) addressing the deficiencies in the time-resolved PIV system, (c) completing the compilation of time-resolved data from the computational simulations, (d) acquiring standard 3-component PIV data, and (e) initiating planning of year two experimental efforts. These were discussed in depth with government stakeholders during a site visit held at the NCPA on 2 November 2012 (see Section 4). The discussions at the meeting will not be repeated here. Rather, the presentation material has been included for reference as Appendices A-C.

In summary of the discussions at the technical interchange meeting, the primary accomplishments during the current reporting period are summarized below:

1. The PIV seeding system was successfully updated in the NCPA Anechoic Jet Laboratory. This system allows for injection of a pH balanced ethanol solution carrying 0.3 micron alumina power directly into the propane burner thereby seeding the jet flow.

2. Standard 3-component PIV measurements were acquired using the new seeding system. The acquisition plane was oriented on the jet symmetry plane, and image data were acquired in three regions successively downstream of one another. Seed density and image quality look very good. Analysis of the image data is currently ongoing.

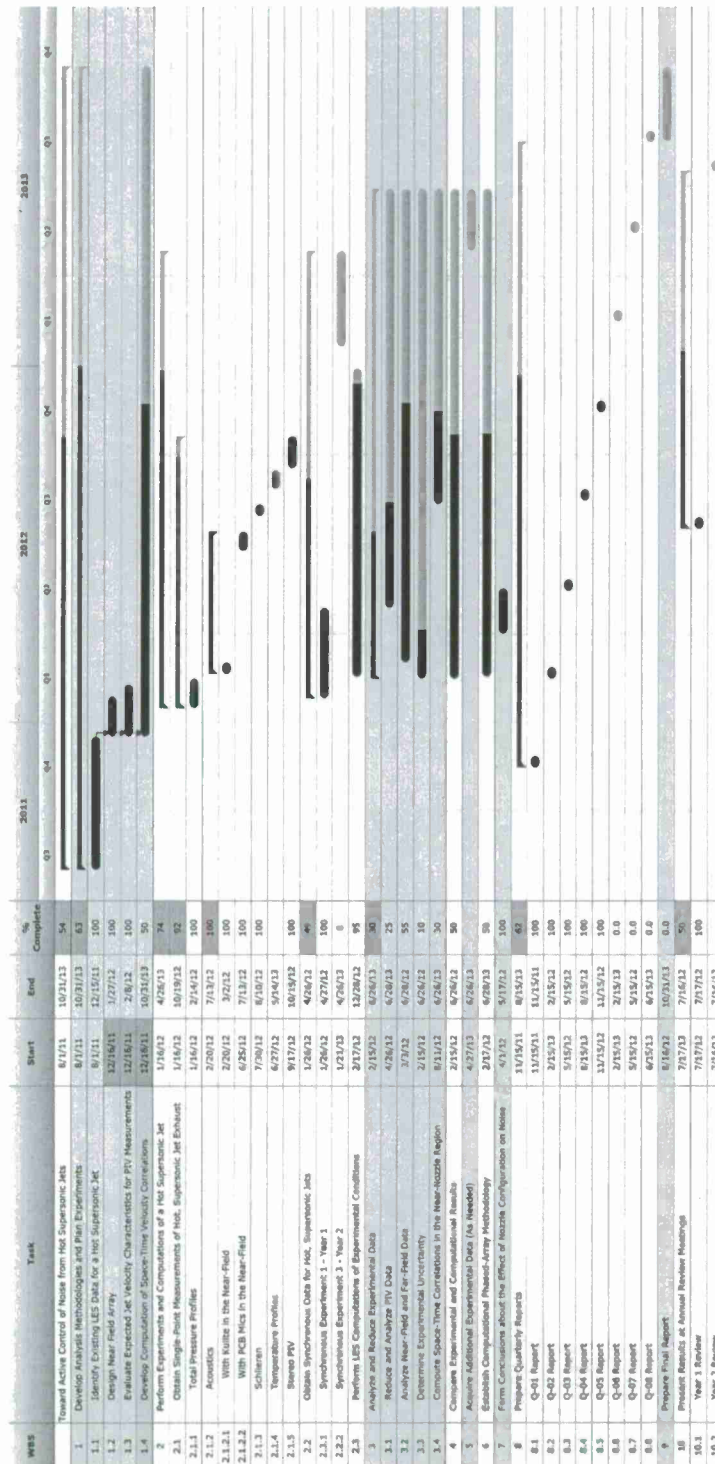| WBS	Task	Start	End	% Complete
	Toward Active Control of Noise from Hot Supersonic Jets	8/1/11	10/31/13	54
1	Develop Analysis Methodologies and Plan Experiments	8/1/11	10/31/13	63
1.1	Identify Existing LES Data for a Hot Supersonic Jet	8/1/11	12/15/11	100
1.2	Design Near-Field Array	12/16/11	1/27/12	100
1.3	Evaluate Expected Jet Velocity Characteristics for PIV Measurements	12/16/11	2/6/12	100
1.4	Develop Computation of Space-Time Velocity Correlations	12/16/11	10/31/13	50
2	Perform Experiments and Computations of a Hot Supersonic Jet	1/16/12	4/26/13	74
2.1	Obtain Single-Point Measurements of Hot, Supersonic Jet Exhaust	1/16/12	10/19/12	92
2.1.1	Total Pressure Profiles	1/16/12	2/14/12	100
2.1.2	Acoustics	2/20/12	7/13/12	100
2.1.2.1	With Kulite in the Near-Field	2/20/12	3/2/12	100
2.1.2.2	With PCB Mics in the Near-Field	6/25/12	7/13/12	100
2.1.3	Schlieren	7/30/12	8/10/12	100
2.1.4	Temperature Profiles	4/27/12	5/14/13	100
2.1.5	Stereo PIV	9/17/12	10/19/12	100
2.2	Obtain Synchronous Data for Hot, Supersonic Jets	1/26/12	4/26/12	46
2.3.1	Synchronous Experiment 1 - Year 1	1/26/12	4/27/12	100
2.2.2	Synchronous Experiment 3 - Year 2	1/23/13	4/26/13	0
2.3	Perform LES Computations of Experimental Conditions	2/17/12	12/28/12	95
3	Analyze and Reduce Experimental Data	2/15/12	6/26/13	50
3.1	Reduce and Analyze PIV Data	4/26/12	4/26/13	25
3.2	Analyze Near-Field and Far-Field Data	3/3/12	4/26/12	55
3.3	Determine Experimental Uncertainty	2/15/12	4/26/13	10
3.4	Compute Space-Time Correlations in the Near-Nozzle Region	8/11/12	6/26/13	30
4	Complete Experimental and Computational Results	2/15/12	6/26/13	50
5	Acquire Additional Experimental Data (As Needed)	4/27/13	6/26/13	
6	Establish Computational Phased-Array Methodology	2/07/12	6/28/13	98
7	Form Conclusions about the Effect of Nozzle Configuration on Noise	4/1/12	5/17/12	100
8	Prepare Quarterly Reports	11/15/11	8/15/13	63
8.1	Q-01 Report	11/15/11	11/15/11	100
8.2	Q-02 Report	2/15/12	2/15/12	100
8.3	Q-03 Report	5/15/12	5/15/12	100
8.4	Q-04 Report	8/15/12	8/15/12	100
8.5	Q-05 Report	11/15/12	11/15/12	100
8.6	Q-06 Report	2/15/13	2/15/13	0.0
8.7	Q-07 Report	5/15/12	5/15/12	0.0
8.8	Q-08 Report	6/25/13	6/15/13	0.0
9	Prepare Final Report	8/16/12	10/31/13	0.0
10	Present Results at Annual Review Meetings	7/17/13	7/16/12	50
10.1	Year 1 Review	7/17/12	7/17/12	100
10.2	Year 2 Review	7/16/13	7/16/12	100

Figure 1. Project chart showing WBS items and current completion status as of the end of the reporting period.

3. Compilation of all the time-resolved data from the computational simulations is approximately 95% complete. This data is being shared within the collaborative team to facilitate exploration of noise source indicators. Analysis methodologies developed will later be applied to experimental data during the year two efforts.

4. Comparisons between the experiment and the computational simulation have been performed showing very good agreement. Additional work is needed to detail the uncertainty in the measurements to ground the comparisons.

5. The high-speed Cordin camera used for Auburn's MHz PIV system has been sent back to Cordin. They are working to eliminate the focusing and image acquisition problems that hampered the year one experiments. At the same time, other options for optical acquisition of flow-field data are being explored. Contact has been made with the sellers of the Kirana camera. Dr. Thurow is seeking the opportunity to get Specialised Imaging, Inc., to demo the camera at the NCPA during the year two experiments allowing for acquisition of time-resolved data.

6. Flow-field data was acquired using Auburn's Plenoptic PIV data in the region near the nozzle exit (1-3 jet diameters downstream from the jet exit). Plenoptic imaging provides for full-field reconstruction of a 3-space region from a single image. The laser system was used to illuminate a volume approximately 1.5 inches on a side. Both image quality and illumination levels looked very good. Auburn is now processing the data to determine the feasibility of further use of this method to obtain jet velocity data.

3 Technical/Cost Status & Problem Areas

None

4 Publications, Meetings, and/or Travel

- On 2 November 2012, NCPA hosted the government stakeholders for a site visit. Those in attendance included B. Henderson (ONR), J. Bridges (NASA), and A. Aubert (NAVAIR) and presentations were given by NCPA (N. Murray) and CRAFT Tech (P. Panickar) covering year one accomplishments and current efforts. Presentation material has been included for reference as Appendices A-C. Also, the meeting minutes are attached in Appendix D.

- A conference paper titled "Localization of Acoustic Sources in Shock-Containing Jet Flows Using Phased Array Measurements" was accepted for presentation at the 2013 AIAA Aerospace Sciences Meetings. The abstract for the paper is included here as Appendix E.

- A conference paper titled, "Acoustic Source Indicators using LES in a Fully Expanded and Heated Supersonic Jet," was submitted for presentation at the 2013 AIAA Aeroacoustics conference. The abstract is included here as Appendix F.

- Dr. Tinney, along with students Baars and Wochner, submitted the manuscript, "Nonlinear Distortion of Acoustic Waveforms from High-Speed Jets," to *J. Fluid Mech.* This paper represents work conducted at UT Austin under year one of this program. As such, the manuscript is included here as Appendix G.

5 Planned Activities for Next Reporting Period

- Continue analysis of noise source indicators using the computational simulation data.

- Complete analysis of the 3-component PIV data.

- Complete the conference paper "Localization of Acoustic Sources in Shock-Containing Jet Flows Using Phased Array Measurements" and present it at the 2013 AIAA Aerospace Sciences Meeting.

- Bring the uncertainty analysis efforts up to date.

- Finalize arrangements for year 2 experimental efforts to be conducted in Spring 2013.

Appendix A: NCPA TIM – Status Update

Overview Program Status and Plans

U. Miss Technical Interchange Meeting

N00014-11-1-0752
Office of Naval Research
Arlington, VA 22203-1995
Contract Monitor: Brenda Henderson

Prepared By:
Nathan E. Murray
National Center for Physical Acoustics (NCPA)
University of Mississippi
University, MS 38677
(662) 915-3190
nmurray@olemiss.edu

1 November 2012

THE UNIVERSITY OF MISSISSIPPI
NATIONAL CENTER FOR PHYSICAL ACOUSTICS

N00014-11-1-0752 :: Technical Interchange Meeting :: Status Update   Page 2

AGENDA

▷ Overview Program Status and Plans

▷ Progress Since Year End Meeting

▷ Break

▷ Progress on Computational Efforts and Source Identification

▷ Discussion of Broader Impact

▷ Tour of NCPA Facilities and Demo Jet Lab Operation

▷ Lunch (sandwiches provided)

▷ NCPA Capabilities in Acoustic Propagation

▷ Closing Discussions

THE UNIVERSITY OF MISSISSIPPI
NATIONAL CENTER FOR PHYSICAL ACOUSTICS

OBJECTIVES

▷ Exp. Characterization of Hot, Shock-Containing, Supersonic Jets

– Temporal characterization of the development of large-scale structures

– Synchronous pressure measurements in the hydrodynamic periphery

– Simultaneous far-field acoustic measurements

▷ Advance Understanding of Relevant Noise Sources

▷ Quantify Linear and Non-Linear Coherence/Propagation

▷ Advance Computational Modeling and Noise Source Localization

THE UNIVERSITY OF MISSISSIPPI

NATIONAL CENTER FOR PHYSICAL ACOUSTICS

YEAR 1 ACCOMPLISHMENTS

▷ Cold Jet Mach 3 Experiments at UT Austin

▷ Single Point Probe Measurements of NCPA Jet

▷ Near/Far-Field Acoustic Measurements at NCPA

▷ First Joint Experiment HDR/MHz PIV with Acoustics

▷ CFD Simulations of NCPA Configuration Validated with Exp. Data

▷ Computational Beamforming Framework Established

THE UNIVERSITY OF MISSISSIPPI

NATIONAL CENTER FOR PHYSICAL ACOUSTICS

YEAR 1 ACCOMPLISHMENTS

THE UNIVERSITY OF MISSISSIPPI
NATIONAL CENTER FOR PHYSICAL ACOUSTICS

YEAR 1 ACCOMPLISHMENTS

▷ Largely Student Led Effort

– Students in Residence at U. Miss. for joint experimental efforts.

▷ Comp. Exp. at U. T. Austin

– NCPA supplied UT Austin with a Mach 3 nozzle geometry for cold jet studies complementing the experiments at NCPA.
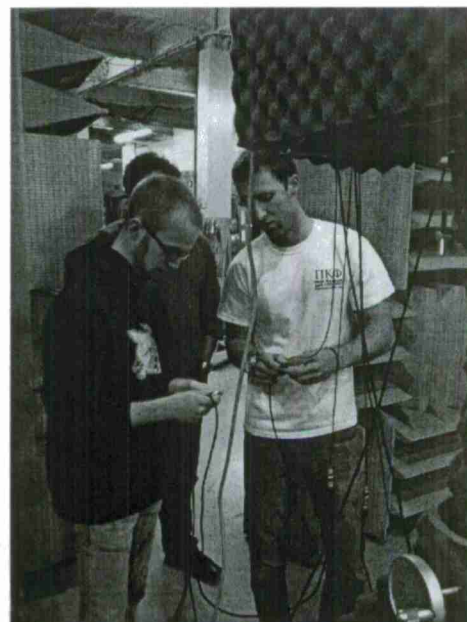
THE UNIVERSITY OF MISSISSIPPI
NATIONAL CENTER FOR PHYSICAL ACOUSTICS

YEAR 1 ACCOMPLISHMENTS

RELATED PUBLICATIONS AND CONFERENCE PRESENTATIONS

▷ Baars, Tinney, Murray, Jansen & Panickar, "The Effect of Heat on Turbulent Mixing Noise in Supersonic Jets." In 49th *AIAA Aerospace Sciences Meeting and Exhibit*, Paper AIAA-2011-1029, Orlando, FL, 2011.

▷ Baars, Tinney, & Wochner, "Nonlinear Noise Propagation from a Fully Expanded Mach 3 Jet." In 50th *AIAA Aerospace Science Meeting and Exhibit*, Paper AIAA-2012-1177, Nashville, TN, 2012.

▷ Murray, Lyons, Tinney, Donald, Baars, Thurow, Haynes & Panickar, "A Laboratory Framework for Synchronous Near/Far-Field Acoustics and MHz PIV in High-Temperature, Shock-Containing, Jets." *Proceedings of the Internoise 2012/ASME NCAD Meeting*, Paper ASME/NCAD-1270, New York, NY, 2012 [invited].

▷ Baars, Tinney & Wochner, "Nonlinear Distortion of Acoustic Waveforms from High-Speed Jets." *Journal of Fluid Mechanics* [submitted].

▷ Panickar, Sinha & Murray, "Localization of Acoustic Sources in Shock-Containing Jet Flows Using Phased Array Measurements." In 51st *AIAA Aerospace Sciences Meeting and Exhibit*, [abstract accepted].

▷ Fiévet, Tinney, Murray, Lyons & Panickar, "Acoustic Source Indicators Using LES in a Fully Expanded and Heated Supersonic Jet." In 19th *AIAA/CEAS Aeroacoustics Conference*, [abstract submitted].

THE UNIVERSITY OF MISSISSIPPI

NATIONAL CENTER FOR PHYSICAL ACOUSTICS

PLANS FOR YEAR 2

▷ Implement a pH-Balanced Fluid-Based Seeder System √

▷ Acquire Additional Characteristic Data

   – Schlieren Imaging √

   – Standard 3-Component PIV √

   – Additional Probe Based Measurements: Total Temperature

▷ Complete Final CFD Iterations (98% complete)

▷ Address Software & Optics Issues with Camera System

   – Camera currently with Cordin to solve software issues.

▷ Perform a Second Joint Experiment

   – Plans in place for Spring 2013

▷ Focus on Data Analysis and Noise Source Characterization

THE UNIVERSITY OF MISSISSIPPI

NATIONAL CENTER FOR PHYSICAL ACOUSTICS

PLANS FOR YEAR 2

COMMENTS ON JOINT EXPERIMENT

▷ Conducting Analysis of CFD Data to Inform Exp. Plans

▷ Exploring Options for Flow Field Measurement

- Plenoptic PIV for Volumetric Velocity Measurements
  * Significant for computing Lighthill stress gradient tensor components.
- Alternate camera for HDR PIV:
  * Kirana Ultra High Speed Video Camera
  * 2 MHz maximum at full-frame with 180 frames per capture
  * Seeking to arrange a demo with the company in Spring 2013.

THE UNIVERSITY OF MISSISSIPPI

NATIONAL CENTER FOR PHYSICAL ACOUSTICS

Appendix B: NCPA TIM – Current Progress

Discussion of Current Progress

U. Miss Technical Interchange Meeting

N00014-11-1-0752
Office of Naval Research
Arlington, VA 22203-1995
Contract Monitor: Brenda Henderson

Prepared By:
Nathan E. Murray
National Center for Physical Acoustics (NCPA)
University of Mississippi
University, MS 38677
(662) 915-3190
nmurray@olemiss.edu

2 November 2012

THE UNIVERSITY OF MISSISSIPPI
NATIONAL CENTER FOR PHYSICAL ACOUSTICS

N00014-11-1-0752 :: Technical Interchange Meeting :: Year 2 Progress to Date   Page 2

OVERVIEW OF CURRENT EFFORTS

▷ Work on Noise Source Indicators

– Developing Application of Seiner's Approach

– Time Dependent Approach

▷ Addressing Limitations in Year 1 Experiment

– PIV Seeding System Update

– Cordin Camera Updates

– Exploring Other Flow Measurement Options (Plenoptic PIV)

▷ Experimental Characterization of the Jet Flow

– Schlieren Visualization

– Standard 3-Component PIV for Comparison to CFD and HDR-PIV

▷ Beamforming Analysis Applied to CFD Data

THE UNIVERSITY OF MISSISSIPPI
NATIONAL CENTER FOR PHYSICAL ACOUSTICS

WORK ON NOISE SOURCE INDICATORS

"What are you planning to do with this experimental data you are collecting with MHz PIV?"

▷ Methods for Identifying Noise Source Generation

– Resolving Time Derivatives of the Stress Tensor
– Resolving Phase Differences in the Strain & Rotation Rate Tensors

▷ Resolving Time Derivatives of the Stress Tensor

$$I(y) = \frac{x_i x_j x_k x_l}{16\pi^2 a_\infty^5 \rho_0 x^4} \int_V \frac{\partial^4}{\partial \tau^4} \langle T_{ij} T'_{kl} \rangle \, d\vec{r} \tag{1}$$

– Resolving 4th-order time derivatives of 2-point correlations like $\langle u_i u_j u'_k u'_l \rangle$
– What sample rate is necessary?
– Only now at a point where we can use the CFD to start evaluation.

▷ Side Note

– $1\,\mu s$ intra-frame spacing typical at these flow speeds (MHz rate)
– MHz-PIV system allows selectable inter-pair spacing *up to* MHz rate

THE UNIVERSITY OF MISSISSIPPI
NATIONAL CENTER FOR PHYSICAL ACOUSTICS

WORK ON NOISE SOURCE INDICATORS

SEINER'S "RATIONAL" APPROACH

▷ Recognizing Source is Double Divergence of Velocity Stress

$$\frac{\partial}{\partial x_j}(u_i u_j) = -\varepsilon_{ijk} u_j \omega_k + \frac{\partial}{\partial x_i}\left(\frac{1}{2} u_j u_j\right) \tag{2}$$

$$\frac{\partial^2 (u_i u_j)}{\partial x_i \partial x_j} = -\varepsilon_{ijk}(s_{ij}\omega_k + r_{ij}\omega_k) + \left(\frac{\partial u_i}{\partial x_j}\right)\left(\frac{\partial u_i}{\partial x_j}\right) \tag{3}$$

– s_{ij} – Strain Rate Tensor
– r_{ij} – Rotation Rate Tensor

▷ Seiner Postulates

– Tennekes & Lumley (1972) suggest that s_{ij} and r_{ij} terms should cancel.
– BUT – Seiner notes that instantaneously the phase differences between the terms would cause them to be significant.

THE UNIVERSITY OF MISSISSIPPI
NATIONAL CENTER FOR PHYSICAL ACOUSTICS

WORK ON NOISE SOURCE INDICATORS

SEINER'S "RATIONAL" APPROACH

▷ Is Compressibility An Issue?

- Seiner's approach falls into the broader vortex methods category:
  * Requires that $\nabla \cdot \vec{V} = 0$.
- We are currently evaluating this claim to discern the applicability of the approach to the current data.

$$\frac{\partial}{\partial x_j}(u_i u_j) = 2 \left(\frac{\partial u_i}{\partial x_j} \frac{\partial u_j}{\partial x_i} - \frac{\partial u_i}{\partial x_i} \frac{\partial u_j}{\partial x_j} \right) \qquad (4)$$

$$\frac{\partial}{\partial x_j}(u_i u_j) = 2 \left(\frac{\partial u_i}{\partial x_j} \frac{\partial u_j}{\partial x_i} - \left(\frac{1}{\rho} \frac{D\rho}{Dt} \right)^2 \right) \qquad (5)$$

- Compute (5) from time resolved CFD and compare to full Lighthill T_{ij} to determine relevance of compressibility in using Siener's Approach as a noise source indicator.

THE UNIVERSITY OF MISSISSIPPI
NATIONAL CENTER FOR PHYSICAL ACOUSTICS

WORK ON NOISE SOURCE INDICATORS

PRELIMINARY RESULTS TO DATE

▷ Calculation of the "Noise Source Indicator"
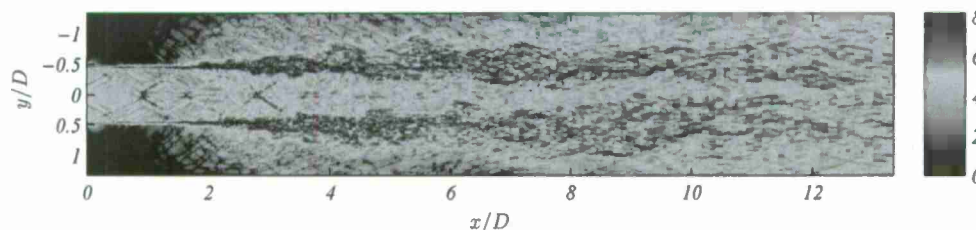
- Above: Instantaneous Snapshot of the Indicator for the Pressure Matched Jet
- Next: Compute full $\frac{\partial^2}{\partial x_i \partial x_j} T_{ij}$ to Compare

▷ What of the Phase Relationship?

THE UNIVERSITY OF MISSISSIPPI
NATIONAL CENTER FOR PHYSICAL ACOUSTICS

WORK ON NOISE SOURCE INDICATORS

NEXT STEP – STRAIN AND ROTATION RATE PHASE

▷ Note the Tensor Products are Scalar Quantities:

$$\frac{\partial^2(u_i u_j)}{\partial x_i \partial x_j} = -\varepsilon_{ijk}(s_{ij}\omega_k + r_{ij}\omega_k) \tag{6}$$

$$= S(\vec{x},t) + R(\vec{x},t) \tag{7}$$

▷ Transform to Fourier Space to Evaluate Phase

$$\hat{G}(\vec{x},f) = \hat{S}(\vec{x},f) + \hat{R}(\vec{x},f) \tag{8}$$

$$\psi(\vec{x},f) = \tan^{-1}\frac{\Im[\hat{G}]}{\Re[\hat{G}]} \tag{9}$$

▷ Evaluate Coupling to Acoustic Propagation

– In what f range are $\hat{S}$ and $\hat{R}$ out of phase?

– How does this couple to acoustically propagating wave numbers?

THE UNIVERSITY OF MISSISSIPPI

NATIONAL CENTER FOR PHYSICAL ACOUSTICS

PREPARATIONS FOR YEAR 2 EXPERIMENT

PIV SEEDING SYSTEM UPDATE

▷ Upgrades to Seed System to Employ pH-Balanced Ethanol Solution

– Funded by NAVAIR program.

– Mark Wernet provided details.

– Built setup to test seed delivery in propane nozzle.

– Installed and tested new system with standard PIV setup.

THE UNIVERSITY OF MISSISSIPPI

NATIONAL CENTER FOR PHYSICAL ACOUSTICS

PREPARATIONS FOR YEAR 2 EXPERIMENT

PIV SEEDING SYSTEM UPDATE
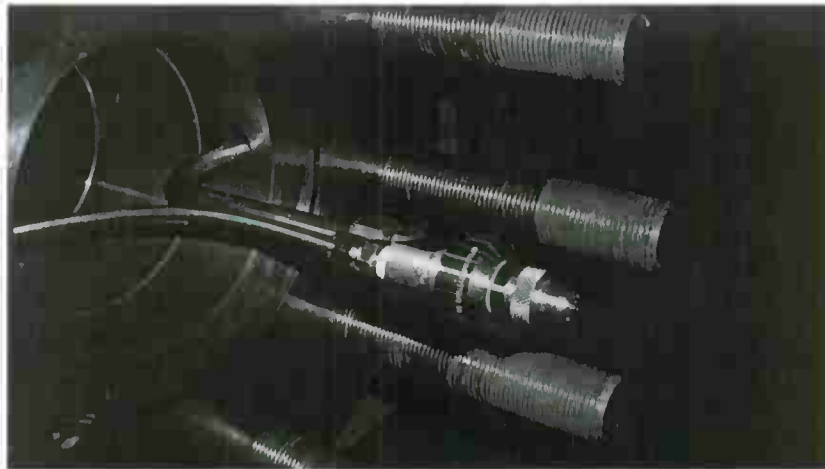
Both propane and ethanol/seed solution injected into burner through a single spray nozzle.

THE UNIVERSITY OF MISSISSIPPI
NATIONAL CENTER FOR PHYSICAL ACOUSTICS

PREPARATIONS FOR YEAR 2 EXPERIMENT

PIV SEEDING SYSTEM UPDATE

Burner uses a flame holder similar in design to that in the Boeing LSAF facility.

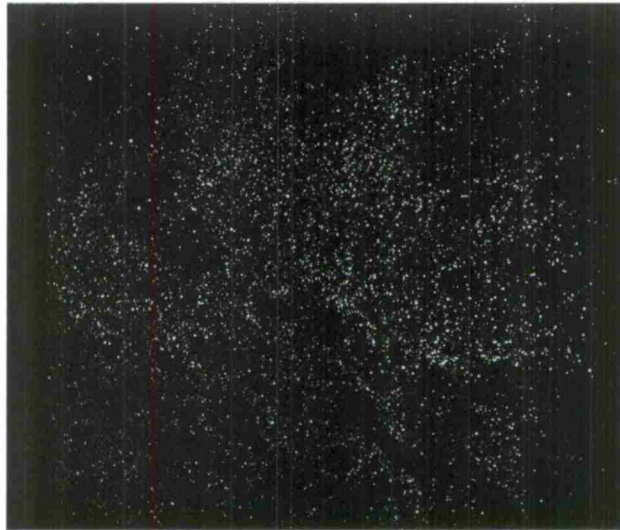THE UNIVERSITY OF MISSISSIPPI
NATIONAL CENTER FOR PHYSICAL ACOUSTICS

PREPARATIONS FOR YEAR 2 EXPERIMENT

PIV SEEDING SYSTEM UPDATE

Much improved results as evidenced by recent PIV measurements.

THE UNIVERSITY OF MISSISSIPPI
NATIONAL CENTER FOR PHYSICAL ACOUSTICS

PREPARATIONS FOR YEAR 2 EXPERIMENT

CORDIN CAMERA UPDATES

▷ Story on the Cordin Camera

- Took delivery on camera 2 weeks prior to moving system to U. Miss.
- Focus depends on each of the 8 internal units being precisely aligned.
  * One of the units found so out of focus that none of the image were useful.
- Software limitations caused the camera to crash repeatedly and loose image data.
- Auburn focused on and completed a suite of data analysis methods to analyze the image data.

▷ Current Status

- Cording currently addressing the two main issues: focus & software.

▷ Exploring Other Flow Measurement Options:

- Alternate camera options – Kirana
- Plenoptic PIV – Volumetric 3-component PIV (not time resolved)

THE UNIVERSITY OF MISSISSIPPI
NATIONAL CENTER FOR PHYSICAL ACOUSTICS

EXPERIMENTAL CHARACTERIZATION OF THE JET

▷ Measurements for Characterization and Validation

- Schlieren Photography
  * Measure spread rate, shock cell spacing, etc.
- 3-Component Planar PIV
  * Validate improved seed system in preparation for Spring 2013 experiments.
  * Acquire single- and two-point statistics for comparison to CFD and HDR-PIV.
  * Use data to evaluation two-point statistics for noise source terms.

SCHLIEREN PHOTOGRAPHY

▷ PCO.Edge camera for image acquisition

▷ Xenon spark lamp for illumination (micro-sec pulse width)

▷ 6-inch parabolic mirrors for collimation

▷ Folded Z-planform optical arrangement

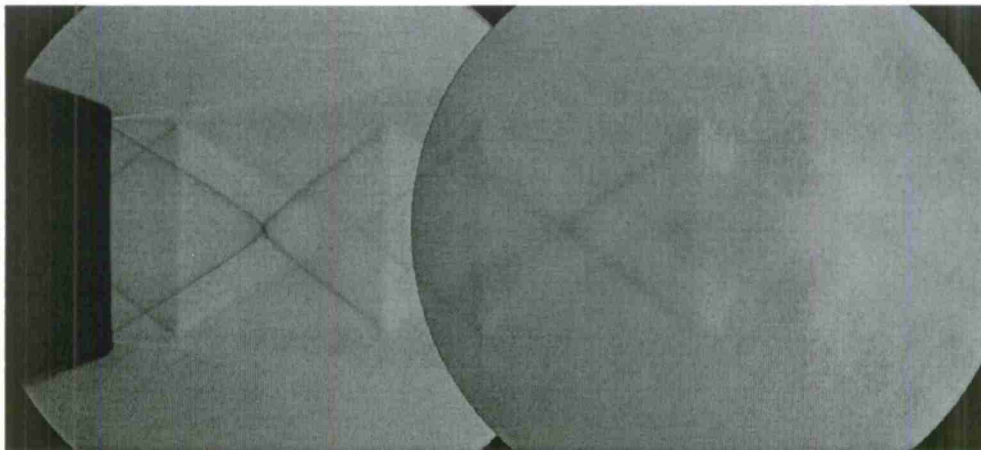THE UNIVERSITY OF MISSISSIPPI
NATIONAL CENTER FOR PHYSICAL ACOUSTICS

EXPERIMENTAL CHARACTERIZATION OF THE JET

SCHLIEREN – PRESSURE MATCHED WITH CENTERBODY

▷ $M_j = 1.74$, $T_j = 1350\,°F$

THE UNIVERSITY OF MISSISSIPPI
NATIONAL CENTER FOR PHYSICAL ACOUSTICS

EXPERIMENTAL CHARACTERIZATION OF THE JET

SCHLIEREN – OVER-EXPANDED WITH CENTERBODY
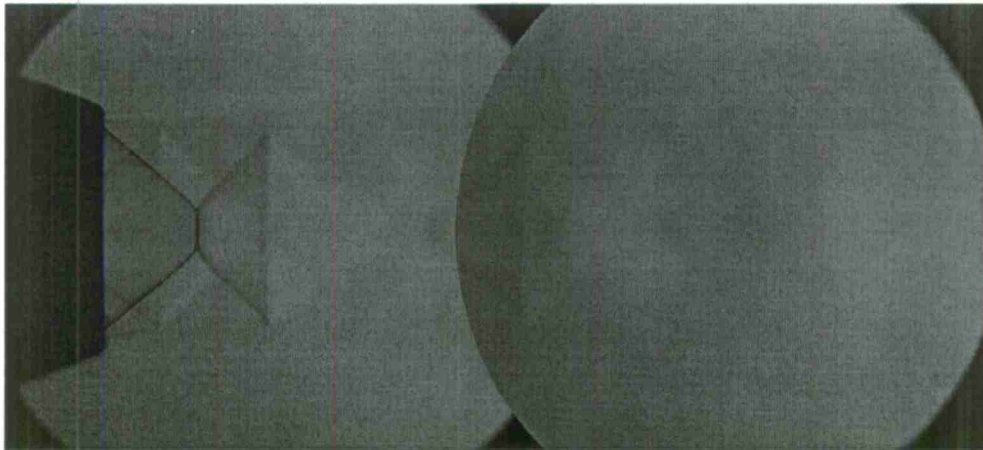
▷ $M_j = 1.55$, $T_j = 1350\,°\text{F}$

THE UNIVERSITY OF MISSISSIPPI
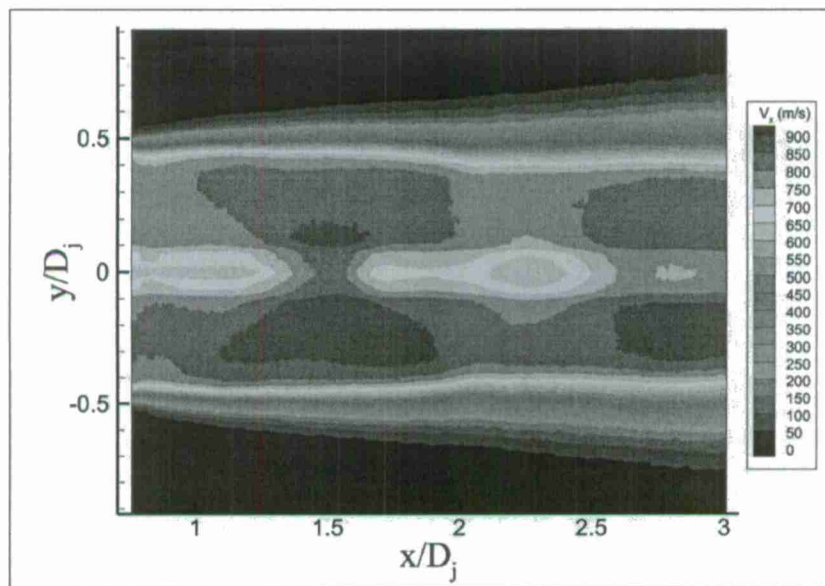NATIONAL CENTER FOR PHYSICAL ACOUSTICS

EXPERIMENTAL CHARACTERIZATION OF THE JET

PIV MEASUREMENTS – PRELIMINARY RESULTS

THE UNIVERSITY OF MISSISSIPPI
NATIONAL CENTER FOR PHYSICAL ACOUSTICS

Appendix C: NCPA TIM – CFD Efforts Status Review

TOWARD ACTIVE CONTROL OF NOISE FROM HOT SUPERSONIC JETS

Contract No. N00014-11-1-0752
Office of Naval Research (ONR)
Contract Monitor: Joseph Doychak, joseph.doychak@navy.mil, 703-696-7646

Program Status Review
November 2nd, 2012
Attendees: Brenda Henderson, James Bridges, Allan Aubert, NCPA, CRAFT Tech

Prepared By:
Praveen Panickar, James Erwin and Raj Sinha
Combustion Research & Flow Technology, Inc. (CRAFT Tech)
6210 Keller's Church Road, Pipersville, PA 18947
Phone: 215-766-1520/Fax: 215-766-1524
sinha@craft-tech.com

CRAFT Tech

SUMMARY OF CRAFT TECH'S RESPONSIBILITIES

- Hybrid RANS-LES (HRLES) simulations of experimental configurations,

- Comparison between experimental measurements and CFD simulations,

- Develop phased array methodology in the CFD domain and determine locations of acoustic sources,

- Provide time-resolved flowfield data to aid in experimental planning.

CRAFT Tech

• Page 1 • Prev • Next • Last • Full Screen • Close

CURRENT STATUS OF CFD SIMULATIONS

- HRLES simulations for four conic nozzle configurations in progress:

    - Conic nozzle with centerbody operating at pressure matched condition,
    - Conic nozzle with centerbody operating at overexpanded condition,
    - Conic nozzle without centerbody operating at pressure matched condition,
    - Conic nozzle without centerbody operating at overexpanded condition.

- Mean-flow and farfield acoustic calculations for 3 configurations available; continuing iterations for the fourth configuration as well as for phased-array calculations and to obtain the time-resolved flowfield.

- Using supercomputing resources from the Department of Defence High Performance Computing Modernization Program (DoD HPCMP) for simulations; NAVY: CRAY XT5 system, 'Einstein', ERDC: CRAY XE6 system, 'Garnet', and ORS: CRAY XE6 system 'Chugach' and 'Copper'.

- Simulations take $\sim$220k CPU hours per configuration, and $\sim$15k CPU hours for post processing.

- Generate $\sim$120 gigabytes of data per configuration.

CRAFT Tech

• Page 2 • Prev • Next • Last • Full Screen • Close

GRID TOPOLOGY

- 6.3 million grid points within the nozzle and in the jet flow,
- Primary goal of calculations is to validate and provide guidance for experimental measurements and establish post processing methodology for beamforming calculations.
- Grid resolution will be refined in next round of calculations:
  - Increased grid resolution in near nozzle regions and within the shear layer will improve calculations of exit turbulent structures,
  - Improved prediction of jet flow features such as potential core length and shear layer development,
  - Improved prediction of spectral characteristics, especially at higher frequencies.

CRAFT Tech

HRLES SIMULATION RESULTS - MEAN FLOW

CONIC NOZZLE WITH CENTERBODY, PRESSURE MATCHED OPERATION

u_bar: 100 271 442 613 784 955
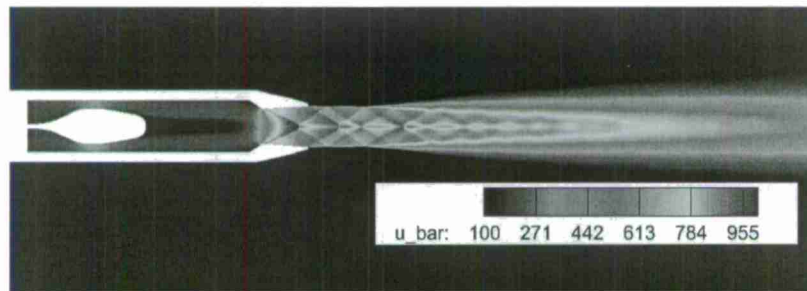
- Time resolved simulations: CFD timestep = 5.0e-8 seconds,
- Wake from centerbody clearly seen
- Double-diamond shock cell structure due to shocks downstream of the sharp throat and at the nozzle exit can also be clearly seen.

CRAFT Tech

Top: Overexpanded operation, bottom: Pressure matched operation.

Pressure matched operation.
Top: With centerbody, bottom: Without centerbody.

HRLES SIMULATION - MEAN FLOW

MEAN PRESSURE

Mean pressure for jet from conic nozzle with centerbody

Top: Overexpanded operation, bottom: Pressure matched operation.

HRLES SIMULATION - MEAN FLOW

MEAN PRESSURE

Mean pressure for jet from conic nozzle with and without centerbody

Pressure matched operation.
Top: With centerbody, bottom: Without centerbody.

HRLES SIMULATION - FLUCTUATING FLOW

STREAMWISE VELOCITY

RMS U velocity for jet from conic nozzle with centerbody

Top: Overexpanded operation, bottom: Pressure matched operation.

HRLES SIMULATION - FLUCTUATING FLOW

STREAMWISE VELOCITY

RMS U velocity for jet from conic nozzle with and without centerbody

Pressure matched operation.
Top: With centerbody, bottom: Without centerbody.

HRLES SIMULATION - FLUCTUATING FLOW

PRESSURE

RMS pressure for jet from conic nozzle with centerbody

Top: Overexpanded operation, bottom: Pressure matched operation.
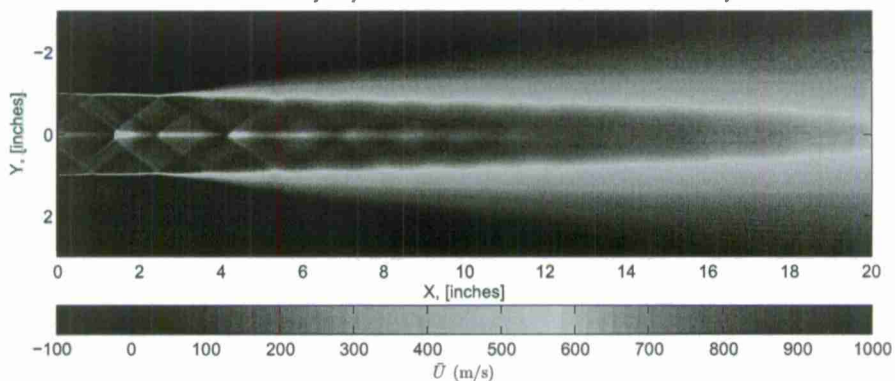
Page 11 • Prev • Next • Last • Full Screen • Close

HRLES SIMULATION - FLUCTUATING FLOW

PRESSURE

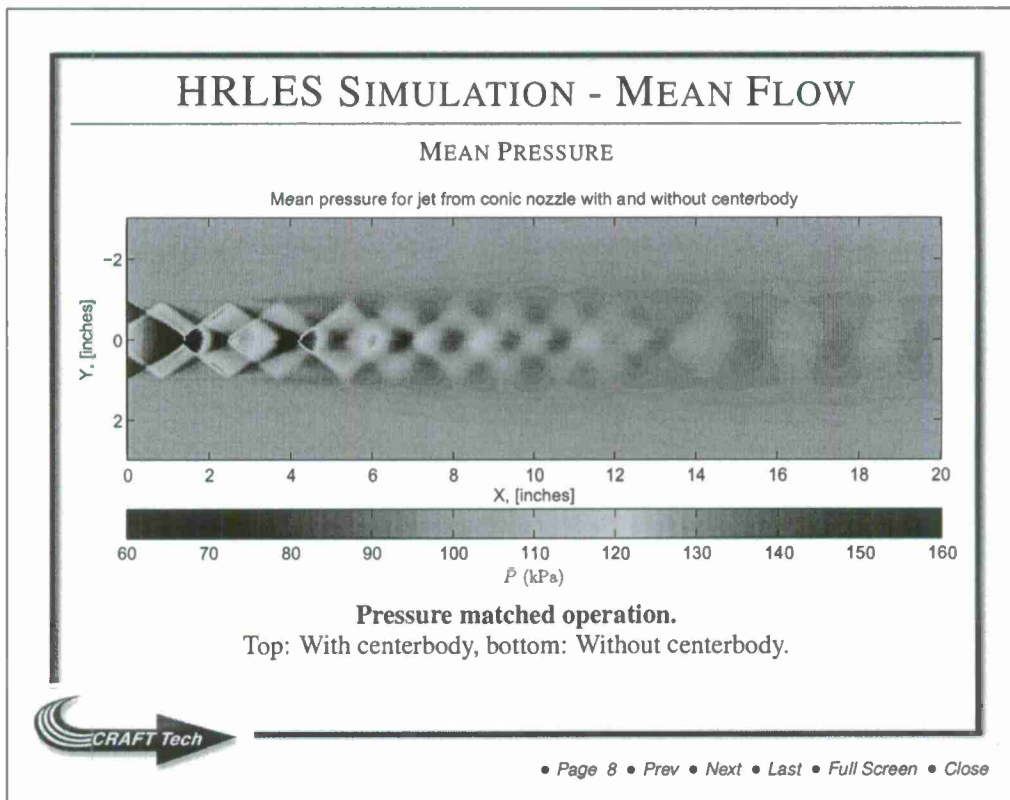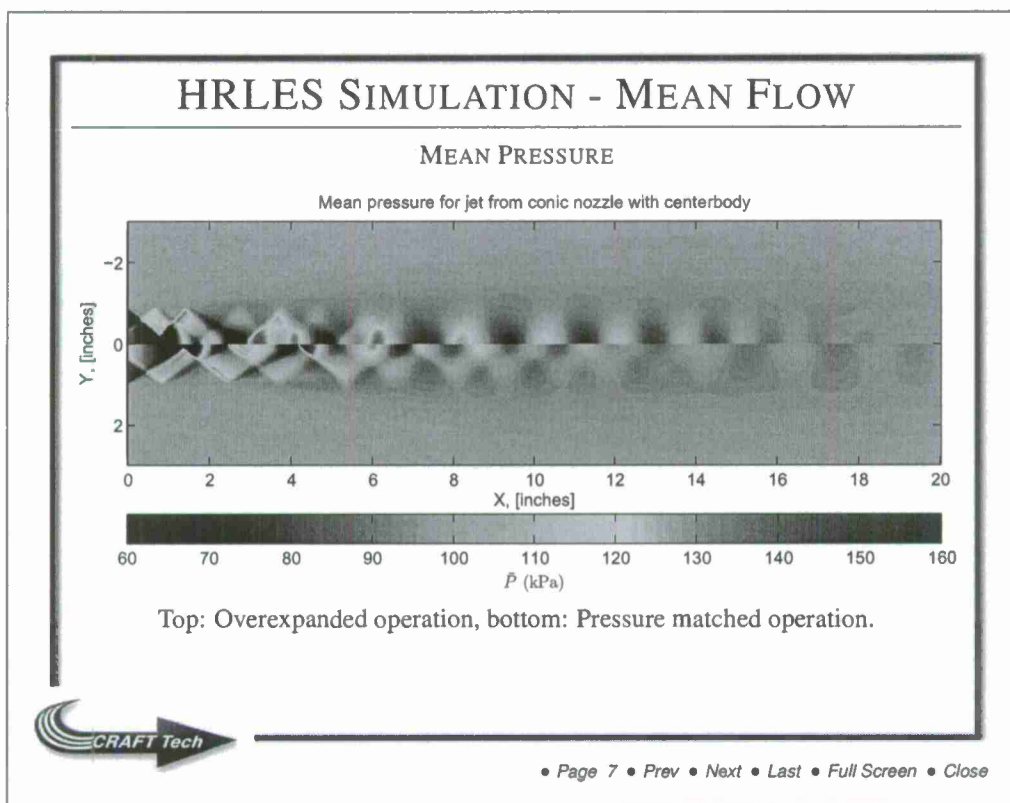RMS pressure for jet from conic nozzle with and without centerbody
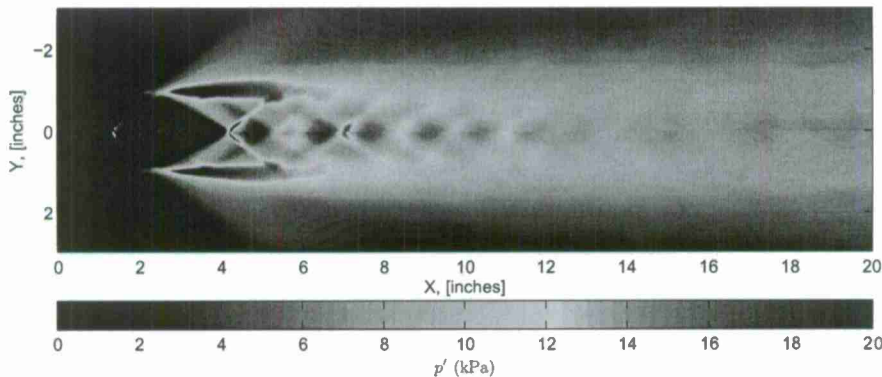
Pressure matched operation.
Top: With centerbody, bottom: Without centerbody.

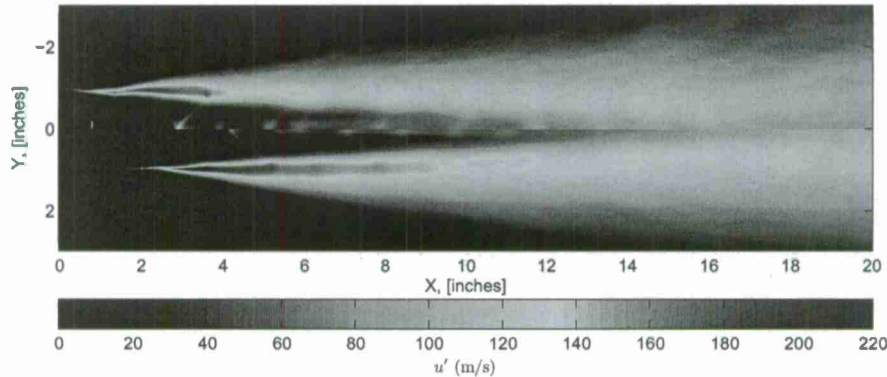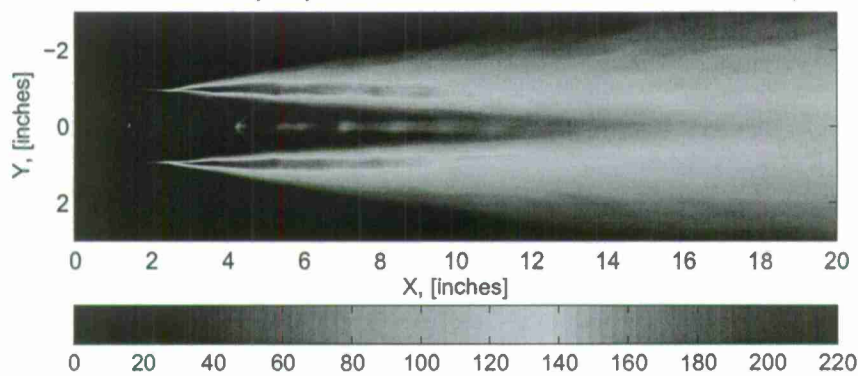Page 12 • Prev • Next • Last • Full Screen • Close

HRLES SIMULATION - MEAN FLOW COMPARISON

CONIC NOZZLE WITH CENTERBODY, PRESSURE MATCHED OPERATION
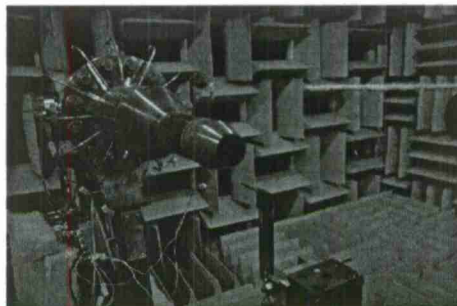
- Uncertainty with regards to actual position of pitot probe in supersonic flow,

- Size of probe is of the order of the size of the slip plane,

- PIV data can hopefully reduce these uncertainties and allow for better comparison between experiments and simulations.

● Page 13 ● Prev ● Next ● Last ● Full Screen ● Close

HRLES SIMULATION - MEAN FLOW COMPARISON

CONIC NOZZLE WITH CENTERBODY, PRESSURE MATCHED OPERATION
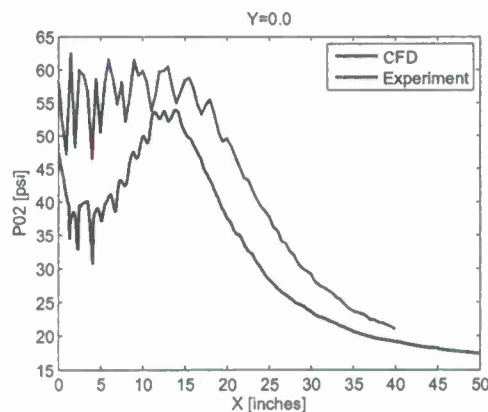
- Discrepancy in experimental and CFD data may be due to uncertainty associated with experimental data...

● Page 14 ● Prev ● Next ● Last ● Full Screen ● Close

HRLES SIMULATION - MEAN FLOW COMPARISON

CONIC NOZZLE WITH CENTERBODY, PRESSURE MATCHED OPERATION
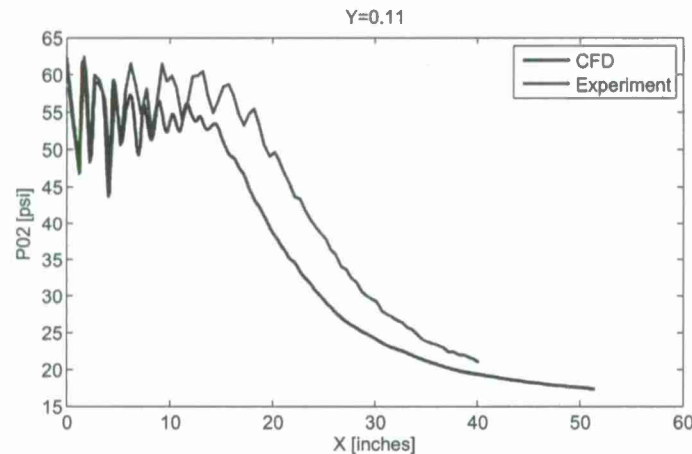
HRLES SIMULATION - FARFIELD ACOUSTICS
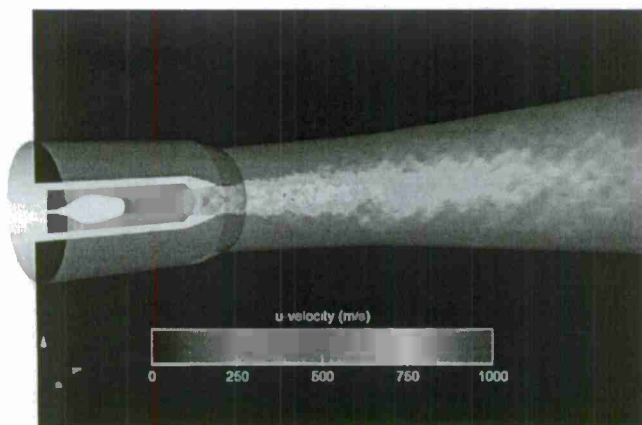
- CFD iterations run with an acoustic data surface (ADS) in place; the time resolved data recorded on this ADS is used as an input to compute the noise at the farfield microphone locations using the Ffowcs-Williams and Hawkings (FW-H) method.

HRLES SIMULATION - FARFIELD ACOUSTICS

Conic nozzle with centerbody – pressure matched operation
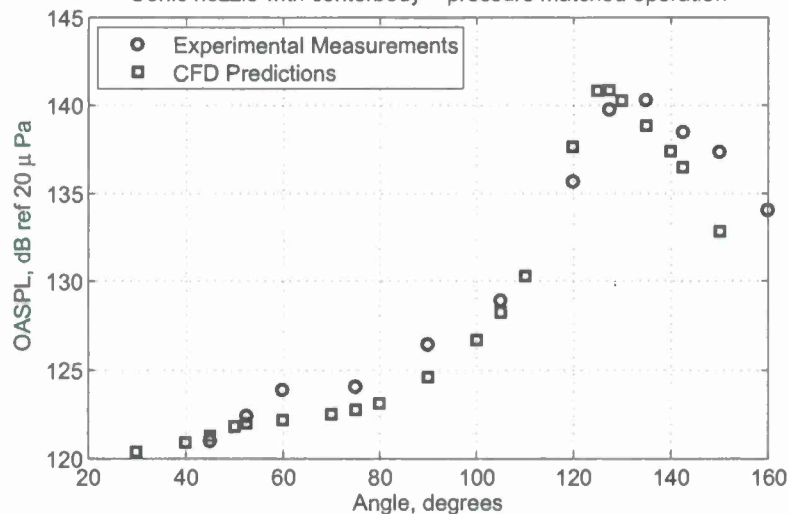
HRLES SIMULATION - FARFIELD ACOUSTICS

Conic nozzle with centerbody – overexpanded operation
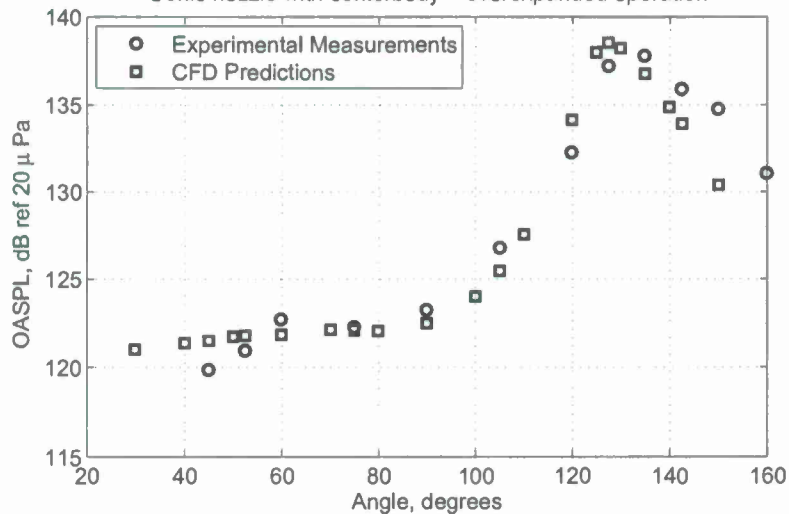
HRLES SIMULATION - FARFIELD ACOUSTICS

Conic nozzle without centerbody – pressure matched operation

HRLES SIMULATION - SPECTRA

Conic nozzle with centerbody – pressure matched operation

HRLES Simulation - Spectra

Conic nozzle with centerbody – pressure matched operation

Legend:
- Experimental Measurement, θ=90.0°
- CFD Prediction, θ=90.0°

• Page 21 • Prev • Next • Last • Full Screen • Close

HRLES Simulation - Spectra

Conic nozzle with centerbody – pressure matched operation

Legend:
- Experimental Measurement, θ=60.0°
- CFD Prediction, θ=60.0°
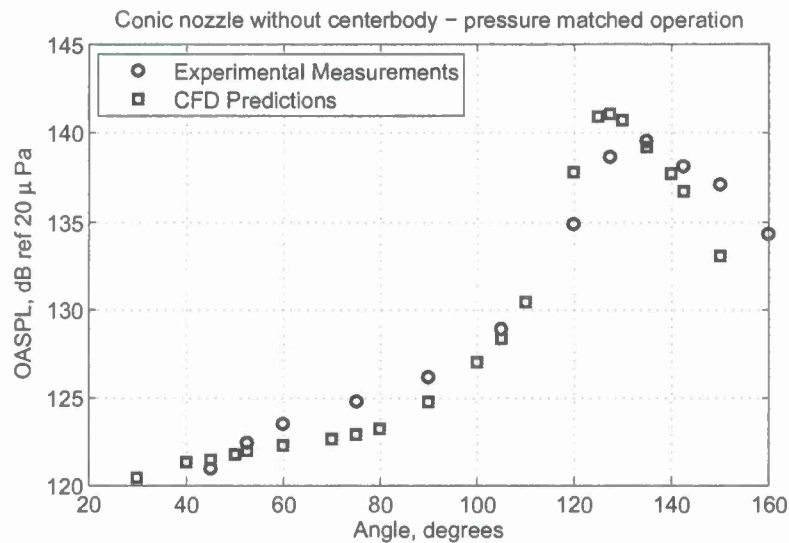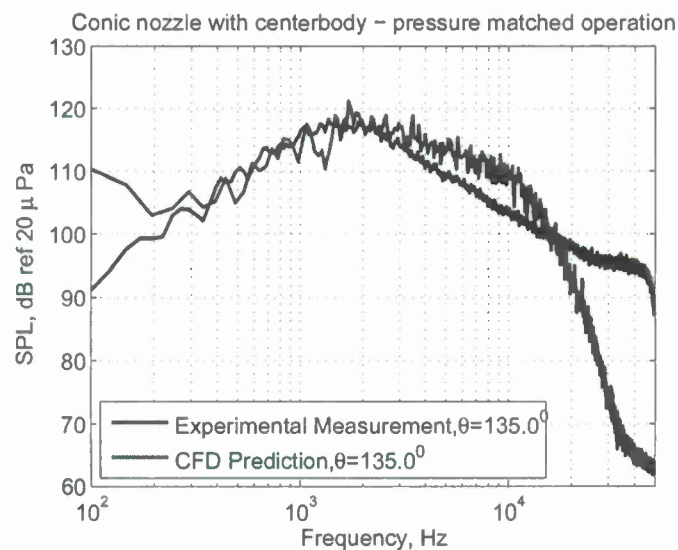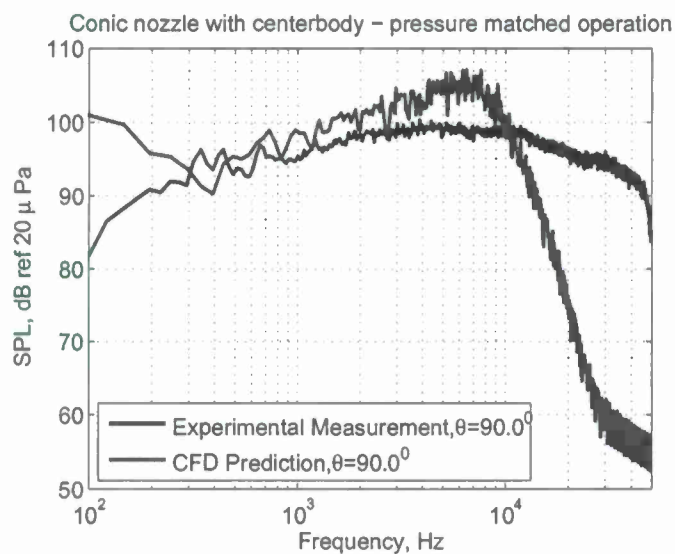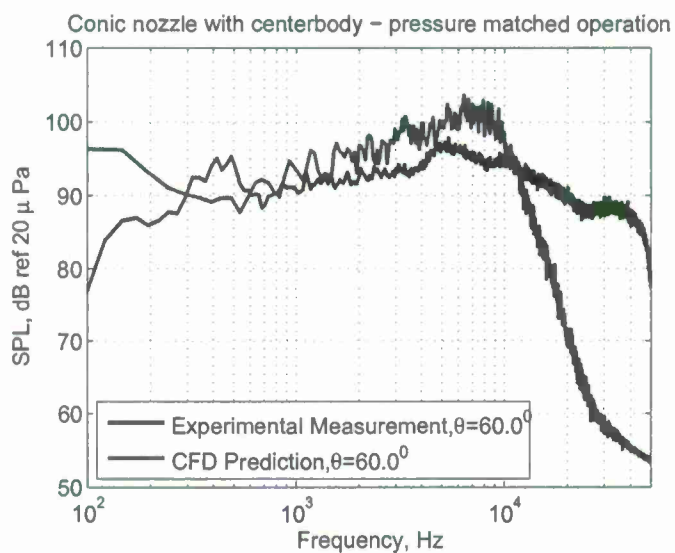
• Page 22 • Prev • Next • Last • Full Screen • Close

INSIGHTS FROM INITIAL CFD CALCULATIONS

- First pass grid does a good job of capturing overall farfield acoustic properties and spectral characteristics at lower frequencies.

- Agreement in comparison of centerline profiles between experiments and CFD within bounds of experimental uncertainty and numerical assumptions.

- Next step: apply grid refinement techniques and perform calculations on improved grid.

CRAFT Tech

PHASED ARRAY CALCULATIONS

PROS AND CONS OF PHASED ARRAY CALCULATION IN CFD DOMAIN

- Use acoustic data surface and Ffowcs-Williams Hawking method to calculate time resolved data at desired microphone location; these locations may not be feasible in a laboratory setting due to spatial or flowfield restrictions.

- Allows for rapidly reconfigurable phased arrays of different designs that can be used to simultaneously "view" the jet flowfield,

  - Can use different phased array design for different frequencies of interest without associated costs of building and setting up a new array.

- Allows for use of many more microphones than practically feasible in experimental work.

- The challenge lies in obtaining 'enough' ensembles in order to sufficiently resolve cross-correlation estimates between the microphones.

CRAFT Tech

EXPERIMENTAL PHASED ARRAY STUDY

EFFECT OF NUMBER OF ENSEMBLES

- Linear array of 32 microphones with logarithmically varying spacing between them,

- Selected configuration of cold, overexpanded jet from a conic nozzle with a centerbody,

- Sample rate = 100 kHz, 1024×1024 samples acquired.

- Traditional delay-and-sum (DAS) beamforming calculations.

CRAFT Tech
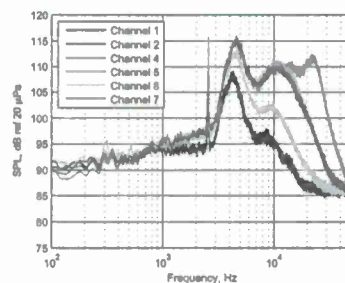
EXPERIMENTAL PHASED ARRAY STUDY

128 ENSEMBLES

- Blocksize of 8192 points, $\Delta f = 12.21$ Hz...

CRAFT Tech
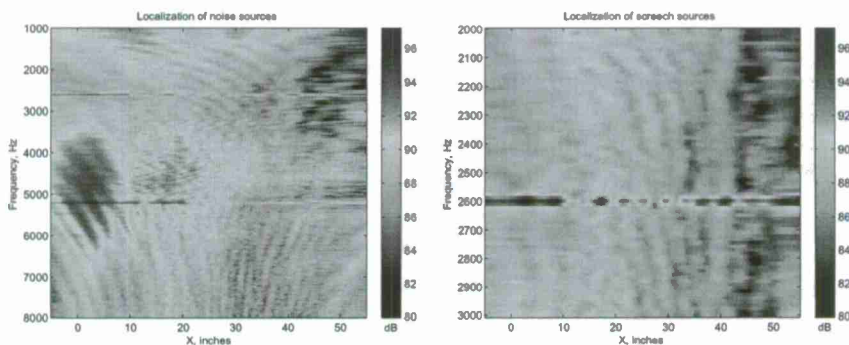
EXPERIMENTAL PHASED ARRAY STUDY

8 ENSEMBLES

- Blocksize of 4096 points, $\Delta f = 24.41$ Hz...
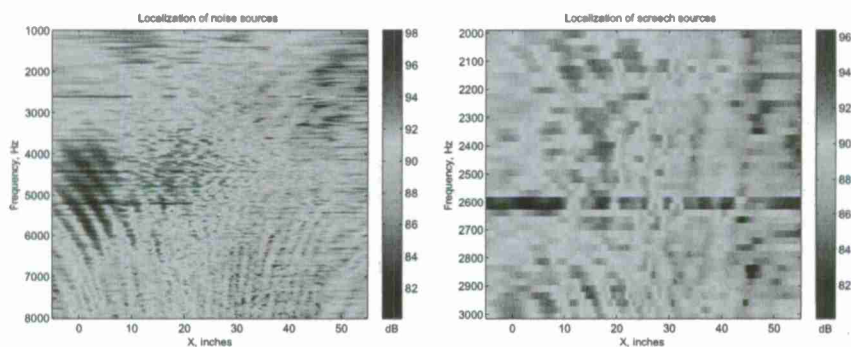
EXPERIMENTAL PHASED ARRAY STUDY

4 ENSEMBLES

- Blocksize of 4096 points, $\Delta f = 24.41$ Hz...
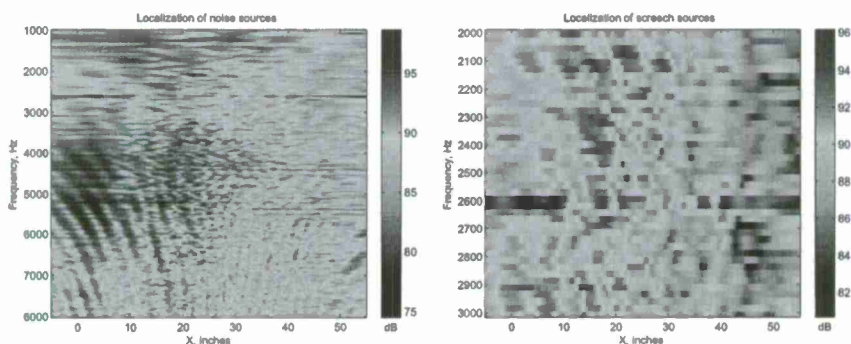
- Prefer between 4-8 ensembles.

EXPERIMENTAL RESULTS

CONIC NOZZLE WITH CENTERBODY, PRESSURE MATCHED OPERATION

Localization of noise sources
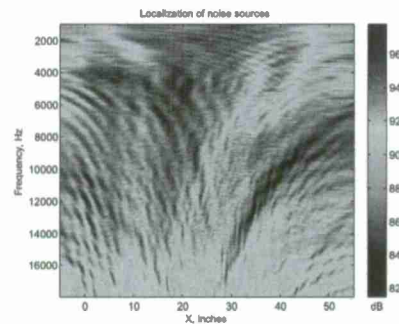
- Experimental beamforming studies of the linear array seem to indicate noise sources up to 30 inches downstream of the jet at a range of frequencies.

- At higher frequencies, there seem to be a secondary region of sources at higher axial locations.

CRAFT Tech

PHASED ARRAY DESIGN

- Three types of array design considered:

  - Microphones arranged in concentric circles (8 microphones per arm, 5 arms + one microphone at center = total 41 microphones),

  - 2D log-spiral arrangement of microphones (9 microphones per arm, 5 arms = total 45 microphones),

  - Microphones arranged in a spiral cage array (31 microphones per arm, 5 arms = total 155 microphones),

CRAFT Tech
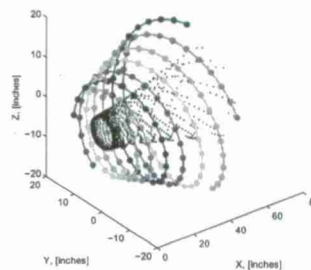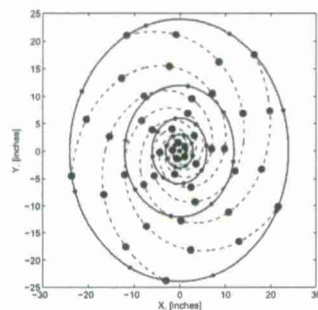
CFD PHASED ARRAY METHODOLOGY

- Using FWH method, obtain time resolved, fluctuating pressure data at phased array microphone locations,

- Calculate and save cross-spectral matrices (CSM) at each narrowband frequency, $G_f(m, n)$, where m and n are microphone indices and f is the narrowband frequency,

    - Hanning window applied in time domain,
    - 6 bins containing 4096 points each, frequency resolution, $\Delta f = 48.83$ Hz,
    - Diagonal elements of the CSM are deleted (reduces self noise from microphones),

- Perform classical beamforming (a.k.a delay-and-sum beamforming) calculations in the $X - Y$ (streamwise-vertical) plane with spatial resolution of $\Delta x = \Delta y = 0.25$ inches.

- Array offset for 2D phased arrays = 72 inches.

- Beamforming results presented in 1/3rd octave bands by summing beamforming results at each constituent narrowband frequency between the high and low frequency limits of that band.

CRAFT Tech

CFD OCTAVE BAND BEAMFORMING RESULTS

2 KHZ CENTER FREQUENCY, SPIRAL CAGE ARRAY

CRAFT Tech
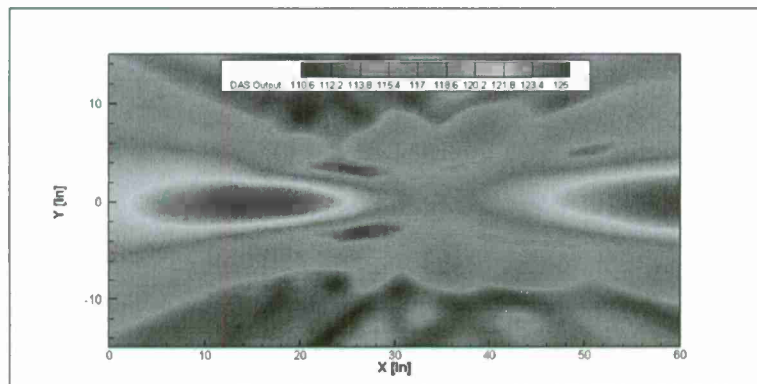
CFD OCTAVE BAND BEAMFORMING RESULTS

3.15 kHz CENTER FREQUENCY, SPIRAL CAGE ARRAY
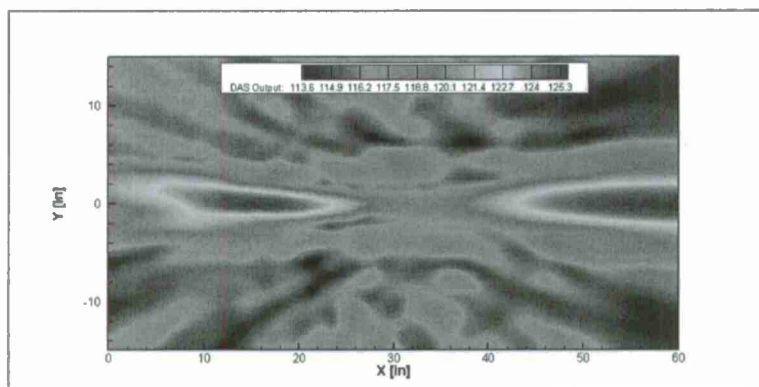
CFD OCTAVE BAND BEAMFORMING RESULTS

5 kHz CENTER FREQUENCY, 2D CIRCULAR AND SPIRAL ARRAYS
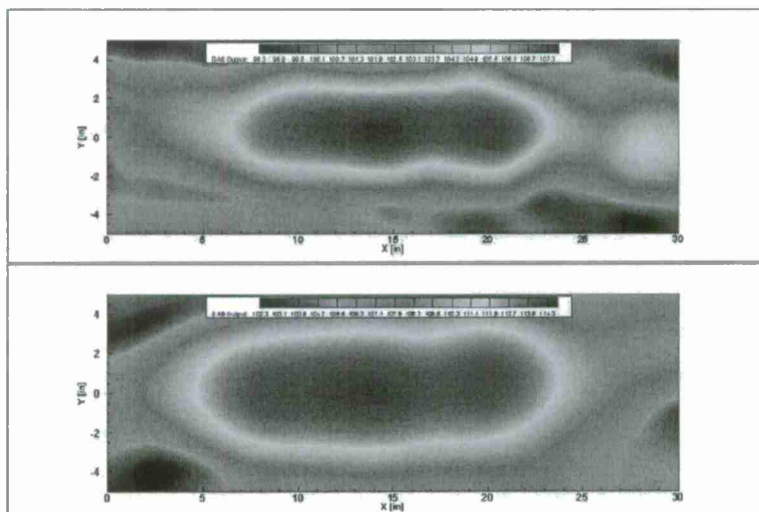
CFD Octave Band Beamforming Results

8 kHz Center Frequency, 2D Circular and Spiral Arrays

CRAFT Tech
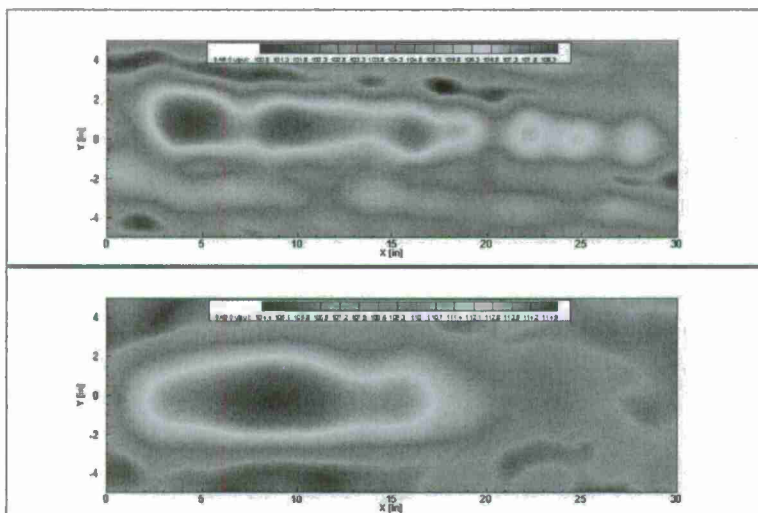
• Page 35 • Prev • Next • Last • Full Screen • Close

CFD Octave Band Beamforming Results

10 kHz Center Frequency, 2D Circular and Spiral Arrays

CRAFT Tech
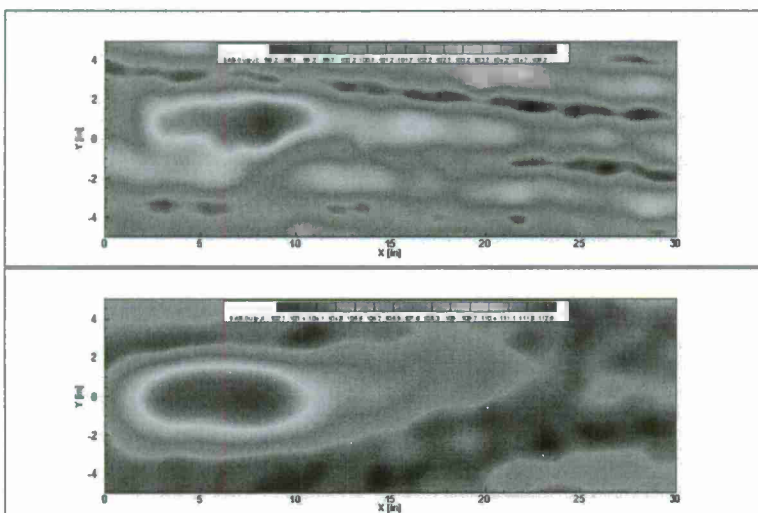
• Page 36 • Prev • Next • Last • Full Screen • Close

CFD OCTAVE BAND BEAMFORMING RESULTS

12.5 kHz CENTER FREQUENCY, 2D CIRCULAR AND SPIRAL ARRAYS

CRAFT Tech
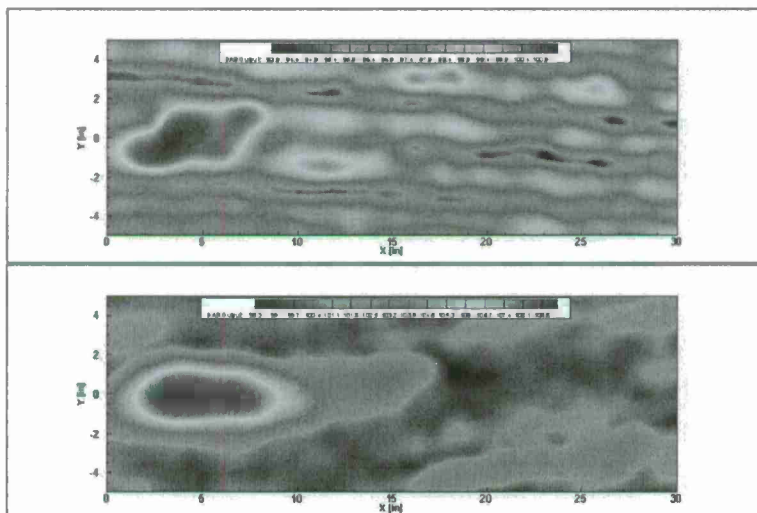
• Page 37 • Prev • Next • Last • Full Screen • Close

CFD OCTAVE BAND BEAMFORMING RESULTS

16 kHz CENTER FREQUENCY, 2D CIRCULAR AND SPIRAL ARRAYS

CRAFT Tech
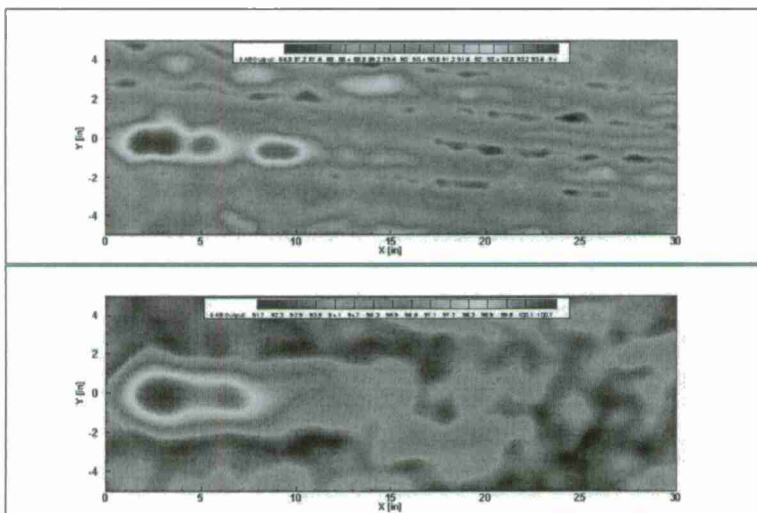
• Page 38 • Prev • Next • Last • Full Screen • Close

INSIGHTS FROM CFD BEAMFORMING

- DAS beamforming shows the presence of acoustic sources that appear to move closer to the jet exit as the 1/3rd octave band center frequency is increased.
  - At the lower frequency the source region extends as much as 12-15 nozzle diameters downstream of the nozzle exit,
  - At the higher frequencies, the sources appear as distinct packets, probably corresponding to the shock cell pattern.
- Results are in broad agreement with experimental beamforming studies conducted with the linear array of microphones.
- Results emphasize the feasibility of beamforming calculations on CFD simulations as a viable technique to study acoustic source characteristics of various jet configurations.
- Results are in qualitative agreement with references showing experimental beamforming studies on hot, shock-containing jets (Brooks, Humphreys and Plassman (AIAA Paper 2010-3780), and Podboy, Bridges and Henderson (2010 NASA TM)).

EFFECT OF ARRAY POINT SPREAD FUNCTION
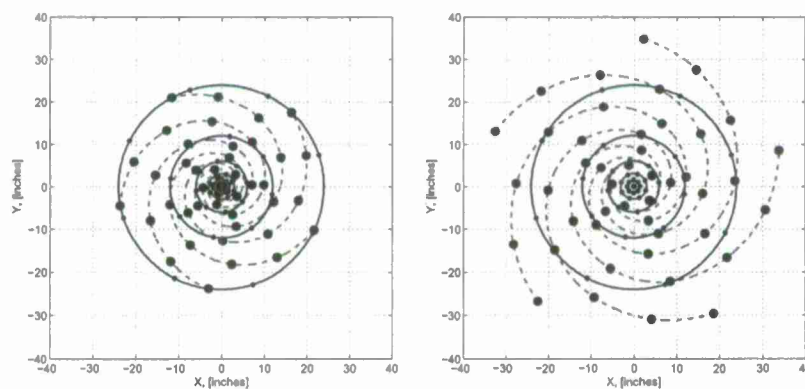
CFD OCTAVE BAND BEAMFORMING RESULTS

8 kHz CENTER FREQUENCY, 2D SPIRAL ARRAYS
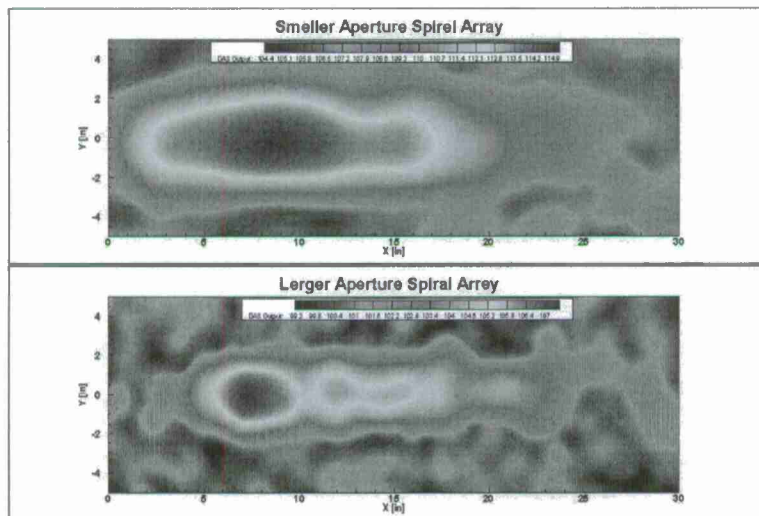
* Page 41 * Prev * Next * Last * Full Screen * Close

CFD OCTAVE BAND BEAMFORMING RESULTS

16 kHz CENTER FREQUENCY, 2D SPIRAL ARRAYS
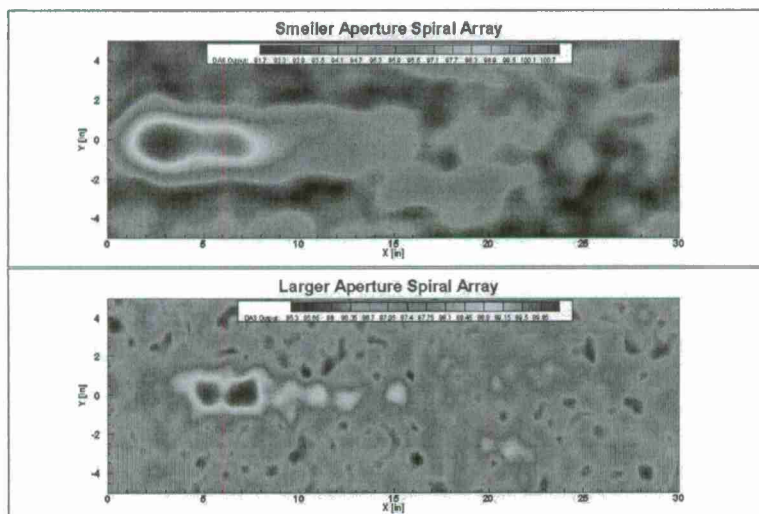
* Page 42 * Prev * Next * Last * Full Screen * Close

FOCUS OF FUTURE STUDIES

- Perform beamforming calculations in a 3D volume rather than on a steering plane in order to determine the volumetric source distribution for a given configuration,

  - This could be important for source localization in a non-axisymmetric nozzle configuration such as rectangular or beveled nozzle exit geometrics.

- Compare source locations and characteristics of remaining jet configurations,

- Metrics for comparing configurations:

  - Integrated acoustic level in a predefined area,
  - Location of peak noise for a given band as a function of beamforming frequency,

- Develop methods to overcome point spread function dependency of results in the traditional DAS method,

  - DAMAS (Brooks and Humphreys, 2004),
  - CLEAN-SC (Sijitsma, 2007)
  - Generalized inverse beamforming, (Zavala, 2010 and Dougherty, 2011),

CRAFT Tech

TEMPORALLY RESOLVED CFD DATA

- One of the objectives of the current program is to *experimentally* acquire time-resolved near-nozzle velocity data.

- This data will be used to provide estimates of farfield noise intensity based on Lighthill's equation,

- Can also be used to evaluate terms involved in Seiner's ''rational'' approach to jet noise such as the strain and rotation rate tensors and the phase difference between them.

- Data from LES simulations will be used to provide insight into flowfield characteristics involved in the making the measurements,

- Calculations will be used to determine effect of discrepancies between experimental and CFD simulations, thereby guiding requirements for future simulations.

CRAFT Tech
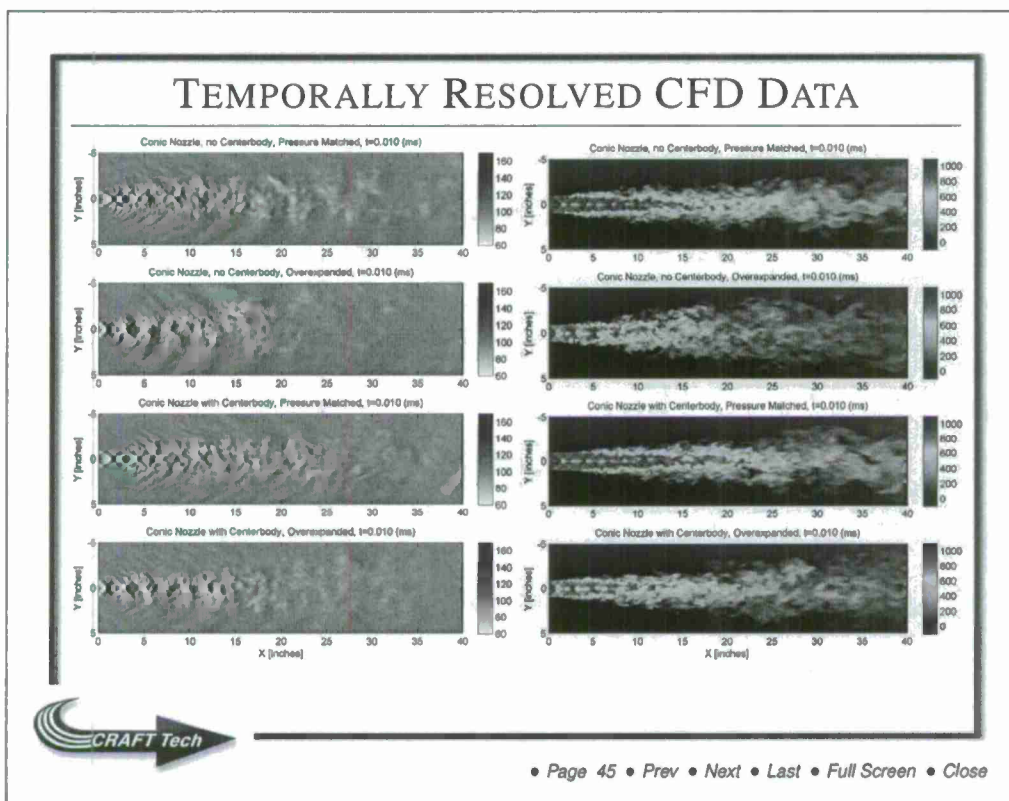
Appendix D: NCPA TIM – Meeting Minutes

Meeting Notes from the ONR Technical Interchange Meeting

Location: National Center for Physical Acoustics (NCPA), The University of Misslssippi, Oxford, MS

Date: November 2, 2012

Attendees: Brenda Henderson (NASA), James Bridges (NASA), Allan Aubert (Navy), Raj Sinha (CRAFT), James Erwin (CRAFT), Praveen Panickar (CRAFT), Nathan Murray (NCPA), Bernie Jansen (NCPA), Marta Panickar (NCPA), Greg Lyons (NCPA).

The meeting started at 8.15 am. Lunch orders from Jimmy Johns were put In by each attendee.

Meeting began with Nathan giving an overview presentation of the project and first year accomplishments. Allan: *Does NCPA plon to buy Auburn's system?* Nathan: *No, we ore currently submitting white popers for o number of joint colloborotions ond we would like to cultivote the colloborotion with them.* Questions were asked about the alternate camera by Kirana, for example what the image resolution was.

Nathan switching to "Discussion of Current Progress"
Brenda pointed out that this project is an effort jointly sponsored by NASA and ONR, not just ONR. It is also NASA funded, just lead by ONR. The benefit of this for NASA is that they don't have to do any management, but they still get to see all the results coming out of the work. Brenda also noted that there are hlgher expectations for this project In year 2. In addition, NCPA and collaborators should be aware that the quarterly reports are more visible than they might think. They get viewed by a number of interested people from Navy and NASA. The year 2 progress will be monitored in more detail, including external committees from academia. Nathan: *When is our yeor 2 review?* Brenda: *Most likely in July, becouse I will review oll reports ot once, ond NCPA is kind of in the middle botch.*

 Back to Nathan's presentation. Brenda: *If you hove 1 MHz PIV with 16 fromes, if you decrease the Hz, do you increose the number of fromes?* Nathan: *No, still only 16 fromes, but better time resolution?* Brenda p.3: *These ore the theoreticol sources or noise, right? Remember thot we ore looking to find octuol sources, not theoreticol.* Nathan: *yes, theoreticol, which hove been used over the yeors. This is our storting point.* p.4 *other ideos – use Seiner's opprooch ond include compressibility foctors ond include phose differences.* Brenda: *Will estimotion errors couse you problems here?* James B.: *Jordon wrote the poper obout their computotionol opprooch with 9 terms, they were ot Moch 1.3 but low Reynold's number. I don't think they considered computotion errors.* Nathan & Raj: *This is the moin poper thot drives our work, but we hope to improve on it with better resolution.* Nathan: *We hope to determine whot couples into the propogotion even if we connot resolve how it hoppens.* Brenda liked that idea and agreed with it. Discussion on updating the PIV system. Allan: *Con you give me o refresher on how your PIV works.* Nathan explained it. Brenda: *Are you going to seed the ombient?* Nathan: *There ore enough porticles in the freestreom thot the whole field gets fed, so no.* James B.: *If you seed your ombient, you don't need thot much light.*

Nathan talklng about the Cordin camera issues.

Talking about Schlieren images. Brenda: *I don't think I ever saw a slip plane in Schlieren.* James B.: *What's your up/down symmetry?* Nathan: *Our setup has a centerbody for more realistic conditions.* James B.: *We usually don't see symmetry in our data, bottom part is usually slower. Symmetric results are usually "fake."*

Nathan ended at 9.25 am. Break.

CRAFT's presentation (Praveen and James) started at 9.40 am. Praveen began the presentation. Brenda: *In your CFD grid setup for the case with centerbody, is the centerbody supported by the struts?* Raj/Praveen: *Just the centerbody, suspended in the air, levitating.* Brenda: *Looking at the image, is the very blunt centerbody similar to what they have in an actual engine?* Nathan/Raj: *Yes, this is modeled from 404 class engines.* Allan stated that he liked the image in the presentation where top is overexpanded and bottom matched condition. Brenda was surprised that centerbody had little effect on the mean streamwise velocity results. James B. suggested how to improve the plots. Allan: *What if we actually put a rotating engine/turbine stage in, what would that do?* Nathan: *Dean Lang tested a swirling flow and it did little to impact acoustics.*

Brenda mentioned that the next meeting will most likely be in DC and presenters should remember that the audience in likely to have questions, so prepare presentations accordingly.

Allen suggested that error bars on the experimental OASPL comparison would be very useful. Brenda: *Would the 160 deg microphone be affected by the recirculation?* Nathan: *Yes, that one would be possibly since we observe soot on it.* Brenda: *Looking at the computational spectra, do you filter some frequencies when calculating OASPL?* James E.: *No, we observed that filtering has little effect (maybe 0.1 dB).* Allan: *So, CRAFT will increase their resolution from 6 to 20 million?* Raj/James W.: *Yes, but it's not only about the resolution, but also where you implement it on the grid.* Brenda: *How is CRAFT improving its model?* Raj: *In many ways, resolution, one major one is to improve the grid near and inside the nozzle. Thus far the grid in the nozzle was very coarse.*

Phase Array Study. Brenda: *What are the physical locations of the seven linear microphones?* Nathan explained how the spiral array fits into the project, that CFD is trying to find which array design is best, and may be implemented in year 3. James B.: *When presenting this to people, most don't know the arrays so more background/images would be useful.* Nathan: *So for CFD/beamforming is only showing us that jets make noise. Our hope is that we can build the "best" array for this particular application and implement in the experimental work.* Praveen's part ended at 10.55 am. James E. took over. Nathan: *This section is really to bring up a discussion.* Brenda: *A segue from BRC effort?* Raj: *Yes.*

Brenda: *NAVY has two problems: carrier hearing noise and community (Oceana problem), so free jet is important for community noise.*

CRAFT's presentation ended at 11.35 am. Raj and James E. left the meeting to catch their flight. NCPA led a lab tour of the Anechoic Jet Laboratory and the Tri-Sonic Wind Tunnel Facility. Attendees observed a jet run at the Anechoic Jet Laboratory.

Lunch

12.15 pm conversation during lunch with Roger Waxler and Richard Raspet from NCPA. Allan: *Prototypes of chevrons to be put on aircrofts for testing are coming in few weeks for us to test. All our research currently concentrates on a limited number of feet from the aircraft on the deck.* They plan on

using the next aircraft noise testing standard. On the deck, the most exposure the personnel has is when the aircraft is at mil power, just sitting for about 30 seconds, when all checks are being performed. Allan requested some relevant information/references about what Waxler/Raspet do. Nathan promised to compile it and send it to Allan. Allan said that in their testing they plan on using four meteorological stations starting at 6 inches to 30 ft. They plan on (the new standard calls for it) 1 second sampling data across a range of altitudes, speeds, etc. Allan expressed that he is very happy to actually talk to someone who knows about the field. He asked that Raspet provides him with information about good references that Allan can use in his research.

Raspect and Waxler left around 12.45. Nathan called that it was the end of the scheduled agenda with some time left for questions/conversations/open dialogue.

James B.: *NASA has an interest in this and while they know it is about supersonic aircraft, but they are really interested in the civilian aircrafts, at least for now, important is LES and validation of the LES. How this research can apply to commercial aircrofts.* Brenda: *Elevated broadband is the big problem.* James B.: *We should make sure we share lessons learned and any problematic situations since they will not be published in journals, but are very beneficial.*

James B.: *Coming up with a practice of simulating a shear layer, inside the nazzle, would be great.* Nathan: *we would like to build a nozzle with an optical access, so we can measure what is happening inside.* Brenda: *Measurements within a rectangular nozzle are being done at Virginia Tech over the next couple of months, one side of the nozzle will have an optical access.* Allen: *what are your ultimate goals in this program?* Questions were raised about the purpose/aim of the beamforming undertaking. James B.: *It might show you an equivalent source, not actual source.*

Allan was very glad we brought GE into the NAVAIR project for consulting on whether the shape can be manufactured.

Brenda: *This kind of presentation is much more beneficial for us than you visiting us. Coming here is very, very useful.*

The meeting ended at 2 pm.

Appendix E: 2013 AIAA Aerospace Sciences Meeting Abstract (accepted)

Localization of Acoustic Sources in Shock-Containing Jet Flows Using Phased Array Measurements

Praveen Panickar* and Neeraj Sinha†

Combustion Research and Flow Technology, Inc. (CRAFT Tech), Pipersville, PA-18947, USA

Nathan E. Murray‡ and Gregory Lyons§

National Center for Physical Acoustics, The University of Mississippi, University, MS-38677, USA

I. Background and Motivation

Noise from supersonic jets fall primarily into two categories, either turbulent mixing noise or shock noise. Of these two, turbulent mixing noise is comprised of two sources, both of which are broadband in nature: (a) the eddy Mach wave radiation which propagates downstream relative to the jet flow direction, and (b) fine scale turbulence which is omni-directional. On the other hand, shock noise can be either narrowband (also called jet screech) or broadband (called broadband shock associated noise, or BSAN), and propagates towards the sideline or upstream directions relative to the jet flow. Shock noise most commonly occurs when a convergent-divergent nozzle is operated at off-design conditions. However, jets exhausting from military nozzles typically contain shocks even when operated at design conditions; this is primarily because the internal contour of these nozzles are not shaped in order to ensure a smooth flow of the jet. Jet noise contributes significantly to noise-induced hearing loss, structural degradation of airframes, and restrictions to maintenance, testing, and training schedules due to noise pollution of communities surrounding military installations.

To this end it is imperative to gain a better understanding of jet noise generation mechanisms in a turbulent flow. Such an understanding is essential if one is to construct predictive models for jet noise. One approach that has been considered is the beamforming technique using a phased array of microphones.[1] This technique has been shown to provide an estimate of the distribution of noise sources in a flow. Reports on the use of beamformed phased arrays in aeroacoustics in general and jet noise in particular was conducted by many researchers including Brooks and his coworkers[2-4] at NASA Langley, Bridges and his coworkers[5,6] at NASA Glenn, Papamoschou, Morris and McLaughlin[7] to name a few. Recently Dougherty[8] developed a new generalized inverse beamforming method for jet noise and demonstrated its effectiveness in mapping coherent sources and extrapolating directivity patterns using a 2D phased array system.

All the reports referenced in the previous paragraph are based on experimental studies; to this date, the authors are unaware of phased array calculations being conducted on simulated data. Working with simulated data removes many of the encumbrances that are present while working in an experimental facility. For instance, in an experimental facility, one is restricted by the size and placement of microphones that

---

*Research Scientist, AIAA Member.
†Technical Director, AIAA Associate Member.
‡Research Scientist and Research Assistant Prof. of Mech. Engineering, AIAA Member.
§Graduate Research Assistant, AIAA Member.

American Institute of Aeronautics and Astronautics

comprise the phased array system. It is not possible to use a phased array system to interrogate a cross plane of the jet unless one resorts to a cage array, in which case care has to be taken that the microphones are not damaged by the flow; this can make the aperture of the phased array larger than what would be practically required depending on the frequency of interest. Additionally, moving the system and setting it up at a different location takes a long time since each move requires a recalibration. These difficulties are not present when simulated data is used for phased array calculations; the phased array can be located anywhere in the flowfield. Practical limitations present in experimental testing such as size of the phased array and the number of microphones available for use are also not present when looking at simulated data. The major limitation when using simulated data is the cost involved with getting time resolved data; generally speaking, though, this difficulty be overcome by using large supercomputing clusters working in parallel to provide time resolved data at a reasonably fast rate.

II.   Experimental Facilities and Computational Capabilities

All the experiments described in this paper will be performed at the Anechoic Jet Laboratory (AJL) at the University of Mississippis National Center for Physical Acoustics. This is a small purpose facility built for the study of high-temperature, supersonic jet noise.[9] The facility was designed with upstream and downstream "stagnation" chambers through which ambient air is pulled by a 10,000 SCFM fan. The air is allowed to percolate into the 19-by-20-by-8 foot chamber (wedge tip to wedge tip) through 50% porosity sliding panels achieving approximately 1 ft/s in the anechoic section (without jet flow). The aspiration of the chamber results in a very even temperature distribution throughout the room and allows the jet entrainment to be less effected by the enclosed space. The jet rig utilizes a propane burner system that can be used to heat the air to a temperature of up to 1500 ^{0}F. Air is supplied from an 1100 hp Ingersoll-Rand Centac compressor through a desiccant dryer system yielding at maximum 5000 SCFM of dry air at 125 psia enabling continuous operation. The propane combustor is housed upstream of the nozzle section and is followed by a ceramic flow conditioner and settling chamber upstream of the main contraction. The nozzle assembly which includes a centerbody housing and the nozzle section. When the centerbody was not used, a straight extension tube was put in its place so that the nozzle exit remained in the same location for all test configurations.

The phased array system consists of 32 exponentially spaced Kulite pressure transducers (type XT-140, dynamic range=0-100 psia), mounted on a stainless steel rod. This array was positioned 60.96 cm (24 inches) below the nozzle exit and offset 7.64 cm (2.94 inches) in the axial direction; the downstream end of the rod was inclined at an angle of 15^0 to the nozzle axis. Digitized fluctuating pressure data from the array was recorded and stored on a National Instruments PXIe (PCI eXtensions for Instrumentation-express) system. The PXIe system has four PXIe-4331 cards(8 channels, 24 bits of resolution, 102.4 kHz maximum sample rate). 1048576 dynamic data points were acquired at 100 kHz per run. For a given configuration, at least 10 such runs of data were recorded. Spectral data was calculated by dividing the data in a given run into blocks of 8192 points each; this yielded a frequency resolution of 12.21 Hz. Depending on the number of files used to do the spectral calculations, the number of ensembles that were averaged ranged from 128 (only one file used) to 1280 (all ten files used).

The computational simulations were performed using CRAFT Tech's CRAFT CFD® program which is structured Navier-Stokes solver that uses an upwind differencing scheme that is fifth order accurate in space and a four stage Runge-Kutta algorithm for time marching. The code is highly parallelized using domain decomposition, with close to linear speed-up parallel performance on several large supercomputers for very large grids. The calculations were performed using a hybrid RANS-LES (HRLES) model. The primary advantage of using HRLES is the ability to include the internal nozzle in the jet noise simulations.

By including the internal nozzle it becomes possible to smoothly transition the subgrid eddy viscosity from within the nozzle boundary layer to the LES. From a strictly flow physics point of view, HRLES simulations show faster breakdown of the laminar shear layer past the nozzle exit. This leads to the creation of smaller scale structures that are a significant contributor to overall noise levels in the sideline and upstream directions, but not in the downstream direction. In the downstream direction, the primary component of noise is due to turbulent mixing and this component is captured with sufficient accuracy by the traditional LES method. Thus, the hope is that by using HRLES, one can improve noise predictions in the sideline and upstream directions and show better agreement with that seen in experiments. The LES grid for the current initiative contains approximately 7 million cells and extends $80R_j$ (R_j is the nozzle radius) in the axial (X) direction and had a radius of $30R_j$ at it's widest extent. Downstream of this, there is a buffer zone that extends a further $40R_j$ in order to damp out unwanted reflections at the LES flow boundaries. Finally, in order to propagate the nearfield acoustics to the farfield, the Ffowcs-Williams and Hawkings (FWH) equation is used. This propagated solution consists of an integration on a fictitious surface surrounding the noise generating mechanisms of the flow. This is achieved by recording the flow variables on this fictitious surface, called the acoustic data surface (ADS) which is located at predetermined constant LES grid levels, with the desired time resolution.

III.   Configurations and Objectives

The current work involves a combined experimental and computational initiative in order to examine and understand the inner nozzle and near nozzle flow conditions and their impact on jet noise. To this end, we shall examine two nozzle geometries. The first consists of a straight walled convergent-divergent section, which we shall refer to as the conic nozzle, and the second consists of 12 identical faceted segments which can be assembled to form the convergent-divergent section of the nozzle. Figure 1 shows a photograph of these two configurations. Both nozzle geometries have the same throat-to-exit area ratio and hence the same 'design' operating condition; however, the experimental facility allows us to operate these nozzles at any desired operating condition. Finally, each of these configurations can be operated with or without the centerbody housing upstream of the nozzle section. Out of all the available configurations to choose from, we select the following six:

1. Faceted nozzle WITHOUT centerbody operating at OVEREXPANDED conditions ($M_j = 1.55$),

2. Conic nozzle WITHOUT centerbody operating at OVEREXPANDED conditions ($M_j = 1.55$),

3. Conic nozzle WITH centerbody operating at OVEREXPANDED conditions ($M_j = 1.55$),

4. Faceted nozzle WITHOUT centerbody operating at CORRECTLY EXPANDED conditions ($M_j = 1.74$),

5. Conic nozzle WITHOUT centerbody operating at CORRECTLY EXPANDED conditions ($M_j = 1.74$),

6. Conic nozzle WITH centerbody operating at CORRECTLY EXPANDED conditions ($M_j = 1.74$),

where M_j is the fully expanded jet Mach number.

The primary objective of the current work will be to investigate the feasibility of performing phased array calculations on simulated jet data. This feasibility will be gaged by comparing results from experimental and computational phased array calculations on the same configuration (configurations 3 and 6 above). The primary objective will be broken up into smaller sub-objectives as follows:

- Acquire fluctuating pressure data on a linear phased array for configurations 3 and 6 in the anechoic jet laboratory at the NCPA.

American Institute of Aeronautics and Astronautics

Approved for Public Release – Distribution is Unlimited
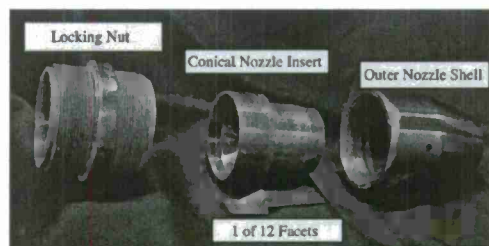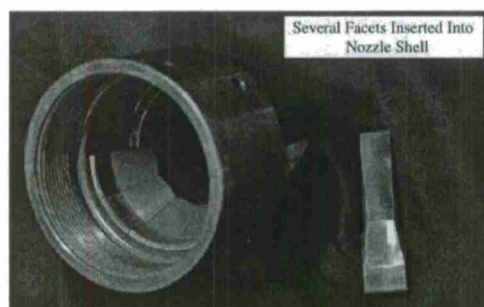
(a) Nozzle parts

(b) Faceted nozzle parts

Figure 1. Photographs of the modular nozzle showing the conical and faceted inserts that will be used in the current study.

- Perform high-fidelity HRLES simulations of the six configurations enumerated in the beginning of this subsection and obtain adequate time-resolved data on the ADS.

- Using FWH equations, propagate the acoustics on the ADS to microphone locations on the linear array that was used in the experimental measurements.

- Compare mean flow characteristics of experimental and computational configurations to ensure agreement.

- Perform phased array calculations of the experimental and computational configurations and compare the source localization results provided by both methods.

Following the successful completion of the primary objective, phased array calculations for the remaining configurations will be performed using different phased array designs and locations. The experiments and computational measurements will be performed on heated jets with stagnation temperature of 1005 K (1350 ^{0}F) unless specified otherwise.

IV. Preliminary Results

The initial round of experiments were conducted on the conic nozzle configuration with the centerbody in place. The nozzles were operated at both overexpanded as well as off design conditions at cold and heated conditions and fluctuating pressure data was recorded by the linear phased array system. Initial processing for the cold temperatures have begun and figure 2 show sample spectra and cross-correlations coefficients calculated for the first six microphones in the array for the cold jet operated at overexpanded conditions.

The spectra clearly show the presence of both shock noise components. The screech tone can be clearly seen
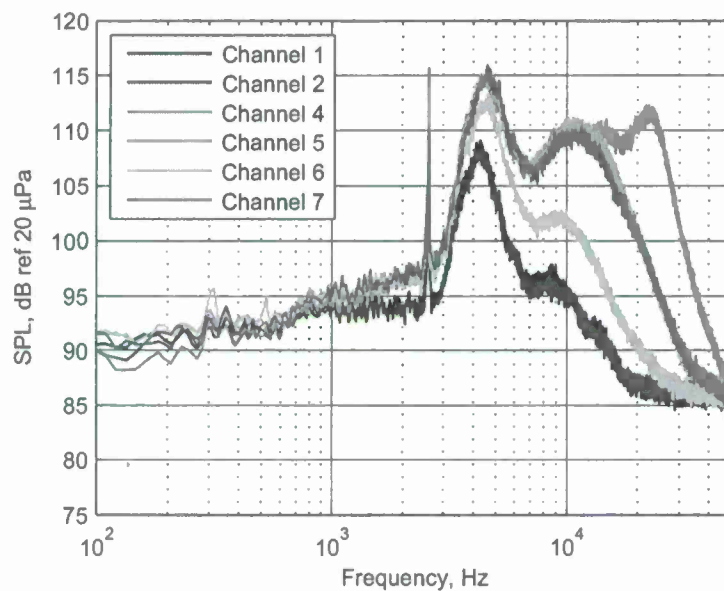
(a) Spectra
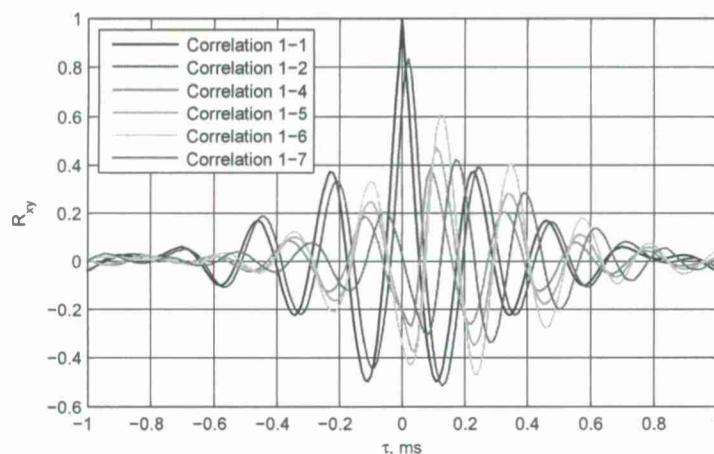
(b) Cross correlation coefficients

Figura 2. (a) Spectra and (b) cross corralation coefficents for the first six sensors in tha experimental linear phased array. Cold jet, overexpanded pressure, $M_j = 1.55$.

at approximately 2.6 kHz and the broadband shock noise hump is seen at higher frequencies between 4 and 5 kHz. In contrast, as shown in figure 3, for heated jets operating at the same overexpanded pressure the presence of screech tones can no longer be clearly discerned. Additionally, it can be seen that the broadband hump has moved to higher frequencies and the correlations between the sensors has reduced. This points to

a fundamental change in the acoustic sources that we shall examine using phased array calculations.

Corresponding to the experimental configuration described above, time resolved HRLES computations have been completed. Figure 4 shows the mean streamwise velocity, pressure and temperature in the XZ (streamwise-vertical) plane. The presence of the centerbody introduces a wake that can be clearly seen downstream of the centerbody inside the nozzle. The shock generated at the sharp throat is clearly visible and it's extent outside of the jet can also be seen. Additionally, the shock generated at the nozzle exit and the propagation of these two shock trains within the jet column can also be seen in these figures. Figure 5 shows the fluctuating component of the streamwise velocity at various distances downstream of the jet. As expected, as long as the potential core persists, most of fluctuating velocity is concentrated in the shear layer and there is very little fluctuation within the core. Figure 6 shows the decay of the streamwise velocity along the axial direction for the conic nozzle configuration with the centerbody. Assuming the potential core to extend axially to a point where the streamwise velocity is 50% of it's value at the nozzle exit, the length of the potential core is calculate to be 25.5 inches when the nozzle is operated at fully expanded conditions.

V.   Future Work

Computations for the remainder of the configurations discussed in §III are currently underway. The results from these computations will be compared to experimentally measured jet characteristics in order to ensure agreement in the gross characteristics between the computational and experimental datasets. It should be kept in mind that these computations are being performed with an ADS in place which will facilitate calculations of time resolved pressure data at target microphone locations in a predesigned phased array. For the initial feasibility calculations, the locations of the computational microphones will correspond to those used for the experimental study. Following this feasibility study, detailed calculations regarding the source locations for the various jet configurations at the different operating conditions will be carried out. In the final paper we shall present results on how the source localization of the jet changes with change in nozzle geometry and operating conditions.

VI.   Acknowledgements

References

[1]Dougherty, R. P., *Aeroacoustic Measurements*, chap. 2, Experimental Fluid Mechanics, Springer, 2001, pp. 62–97.

[2]Humphreys, W. M., Brooks, T. F., Hunter, W. W., and Meadows, K. R., "Design and use of microphone directional arrays for aeroacoustic measurements," *American Institute of Aeronautics and Astronautics Paper 1998-0471*, 1998.

[3]Brooks, T. F. and Humphreys, W. M., "A deconvolution approach for the mapping of acoustic sources (DAMAS) determined from phased microphone arrays," *Journal of Sound and Vibration*, Vol. 294, 2006, pp. 856–879.

[4]Brooks, T. F., Humphreys, W. M., and Plassman, G. E., "DAMAS Processing for a Phased Array Study in the NASA Langley Jet Noise Laboratory," *American Institute of Aeronautics and Astronautics Paper 2010-3780*, 2010.

[5]Agboola, F. A. and Bridges, J. E., "Jet Noise Source Localization Using Linear Phased Array," *NASA Technical Memorandum–2004-213041*, 2004.

[6]Podboy, G. G., Bridges, J. E., and Henderson, B. S., "Phased Array Noise Source Localization Measurements of an F404 Nozzle Plume at Both Full and Model Scale," *NASA Technical Memorandum–2010-216636*, 2010.

[7]Papamoschou, D., Morris, P. J., and McLaughlin, D. K., "Beamformed Flow-Acoustic Correlations in a Supersonic Jet," *AIAA Journal*, Vol. 48, 2010, pp. 2445–2453.

American Institute of Aeronautics and Astronautics

[8]Dougherty, R. P., "Improved Generalized Inverse Beamforming for Jet Noise," *American Institute of Aeronautics and Astronautics Paper 2011-2769*, 2011.

[9]Ponton, M., Seiner, J., Ukeiley, L., and Jansen, B., "A new anechoic chamber design for testing high-temperature jet flows," *American Institute of Aeronautics and Astronautics Paper 2001-2190*, 2001.
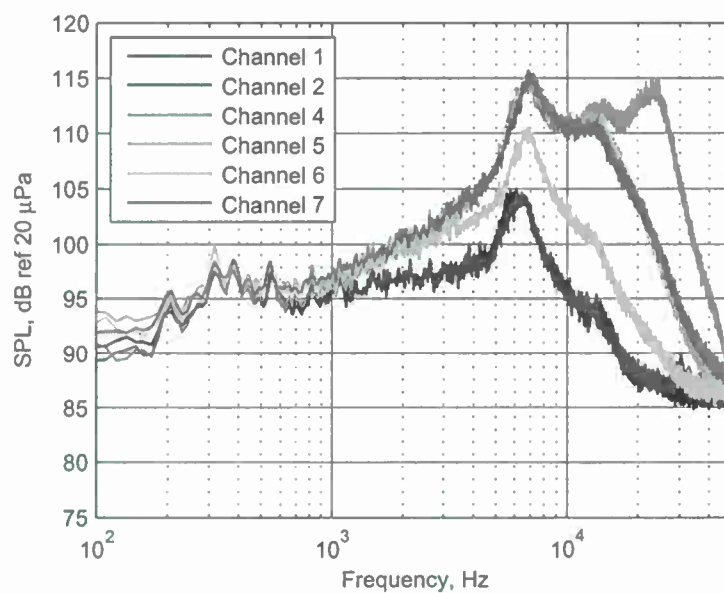
(a) Spectra
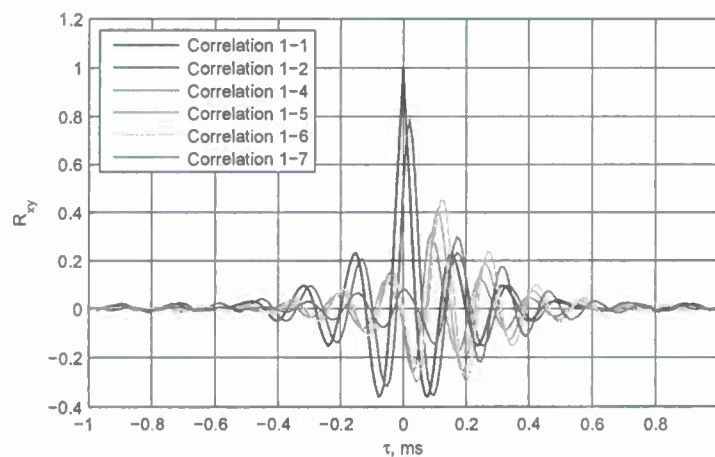
(b) Cross correlation coefficients

Figure 3. (e) Spectra and (b) cross correlation coefficients for the first six sensors in the experimental linear phased array. Heeted jet, $T_j = 1005$ K, ovarexpanded pressure, $M_j = 1.55$.

8 of 10

(a)

(b)

(c)
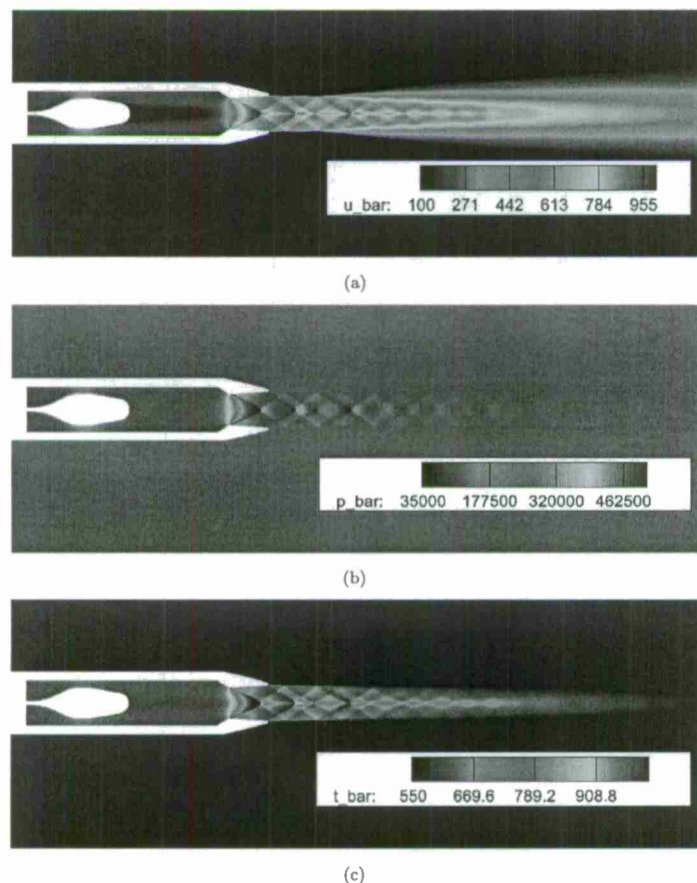
Figure 4. Mean streamwise velocity, pressure and temperature contours (top, middle and bottom, respectively) in the streamwise-vertical (XZ) plane for the conic nozzle with the centerbody configuration with a centerbody.

9 of 10

American Institute of Aeronautics and Astronautics
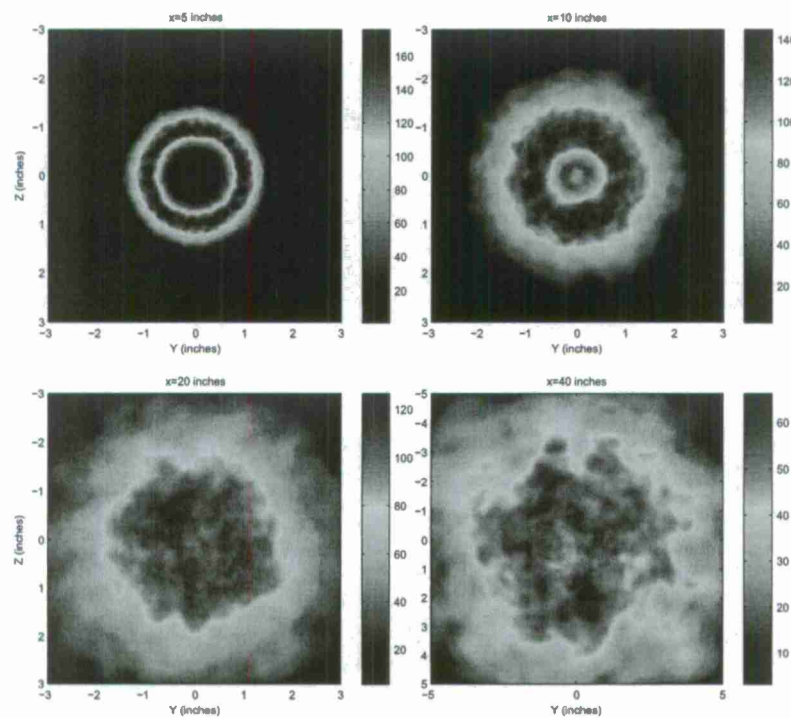
Figure 5. Contours of tha fluctuating component of the streamwise velocity in the YZ (cross-) plana at constent axial stations computed by HRLES for the conic nozzle with the centerbody.
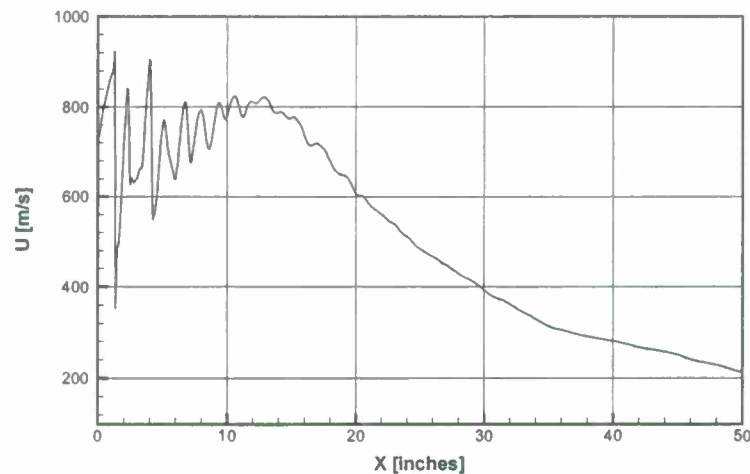
Figure 6. Decay of the streamwise velocity along the nozzle axis for the conic nozzle configuretion with the centerbody operating at correctly expanded conditions.

10 of 10

American Institute of Aeronautics and Astronautics

Appendix F: Abstract Submitted to 2013 AIAA Aeroacoustics Meeting

Acoustic source indicators using LES in a fully expanded and heated supersonic jet.

Romain Fiévet[*] and Charles E. Tinney[†]

Aerospace Eng. and Eng. Mechanics, The University of Texas at Austin, Austin, TX 78712, USA

Nathan E. Murray[‡] and Gregory Lyons[§]

National Center for Physical Acoustics, University of Mississippi, University, MS 38677, USA

Praveen Panickar[¶]

Combustion Research and Flow Technology Inc., Pipersville, PA 18947, USA

A Large Eddy Simulation of a fully expanded heated supersonic jet flow is examined using acoustic source indicators based on vortex dynamics. This is done in an effort to explore the utility of such methods for guiding future experimental measurements where both a spatial and temporal capturing of the velocity field is realized. The accuracy of this rational approach is determined by a detailed comparison with the full Lighthill stress tensor, the findings of which will be the focus of the full paper.

I. Introduction

Capturing sources of noise in high speed jet flows continues to be a difficult proposition despite well over a half century of research.[7] This is principally driven by the fact that sound is produced by the change in the eddy structure as it convects through the flow. Limitations in the experimental community have only recently been alleviated with the advent of spatially and temporally resolved flow measurement systems such as tomographic PIV. Numerically, the accuracy of the simulation is limited by the meshing requirements needed for accurate solution to the governing flow equations.

Several acoustic analogies have been proposed since Lighthill's (1952)[8] seminal paper and include the work of Goldstein (2003),[5] Lilley (1974),[10] and more recently George *et al.*(2007).[4] The strength of these analogies is that they are derived from the complete equations of motion with divergences of the products of density and velocity fluctuations. This however makes it difficult to implement even with the most state-of-the-art experimental diagnostics tools. Alternative approaches, based on vortex sound theory, have also been proposed whereby the role of vorticity is more explicit in the formulation. This began with the pioneering work of Powell (1964)[13] and Möhring (1978)[11] which has since transcended to the recent articles by Schram & Hirschberg (2003).[14] A drawback of these methods is that they impose several restrictions on the nature of the turbulence (inviscid and incompressible), the implications of which are unclear, especially for high Mach number (perfectly expanded supersonic) and heated jets. Nonetheless, they are the only realizable methods that can be applied to experimentally acquired data and so they are quite resourceful in this regard. An approach similar to the aforementioned vortex methods was invoked by Seiner (1998).[15] The idea is that the Lighthill stress tensor can be expressed as a sum of both strain and rotational energies in the jet flow. While, on average, these terms should cancel, they should however be non zero at any instant in time. And so the phase difference between the two terms is then considered to be an indicator of sound production.

In this study, we seek to explore Seiner's (1998)[15] rational approach by first applying the method to a Large Eddy Simulation (LES) of a high Reynolds number, heated, supersonic jet flow. A comparison

---

[*]PhD Student, AIAA Student Member.

[†]Assistant Professor, AIAA Senior Member. http://www.ae.utexas.edu/facultysites/tinney/

[‡]Research Scientist & Research Assistant Prof. of Mech. Engineering, AIAA Member.

[§]PhD Student, AIAA Student Member.

[¶]Research Scientist, AIAA Member.

is made between the full Lighthill stress tensor and the rationalized vortex analogy to see what effect the aforementioned restrictive assumptions (inviscid and incompressible flow) have on the topography of the source field. The findings from this study are being used to provide valuable guidance for an experimental campaign currently underway to study the noise produced by a heated, supersonic jet flow by way of high-speed, volumetric PIV. In what follows, a review of Seiner's (1998) approach is provided in § II followed by a description of the Large Eddy Simulation in § III. The LES is validated against laboratory measurements of the near-field velocity (centerline decay and shear layer spreading rate) and far-field acoustics (OASPL). Preliminary results of Seiner's approach, applied to the LES, is then displayed followed by the prospective work to be included in the full conference paper.

II.   The acoustic source field

A.   Lighthill's Source Term

It is well known that the Lighthill analogy allows one to solve for the far-field pressure using sources which comprise all of the properties of an unsteady fluid in free space. This accounts for all of the effects of the fluid flow, including interactions between the sound field and the turbulence. This inhomogeneous wave equation is obtained by subtracting the divergence of the momentum equation from the time derivative of the continuity equation,

$$\frac{\partial^2 \rho}{\partial t^2} - c_o^2 \frac{\partial^2 \rho}{\partial x_i \partial x_i} = \frac{\partial^2 T_{ij}}{\partial x_i \partial x_j}, \tag{1}$$

where sound generated by accelerations and decelerations of the free space fluid is governed explicitly by Lighthill's stress tensor,

$$T_{ij} = \rho \tilde{u}_i \tilde{u}_j + (p - c_o^2 \rho)\delta_{ij} - \tau_{ij}, \tag{2}$$

with the viscous stress tensor for a Stokesian gas being defined as,

$$\tau_{ij} = \mu \left(-\frac{\partial \tilde{u}_i}{\partial x_j} - \frac{\partial \tilde{u}_j}{\partial x_i} + \frac{2}{3} \left(\frac{\partial \tilde{u}_k}{\partial x_k} \right) \delta_{ij} \right). \tag{3}$$

This encompasses all of the nonlinearities embedded within the Navier-Stokes equation, and so, it was recognized early on[9] that such a formulation was perfectly suited for studying the sound produced by jet flows. A number of items are worth mentioning here, where the utility of modern diagnostic techniques are concerned. The full Lighthill Stress tensor defined in (2), comprises three terms: $(\rho \tilde{u}_i \tilde{u}_j)$, $((p - c_o^2 \rho)\delta_{ij})$ and (τ_{ij}), each of which involve thermo-physical properties of the fluid (density and viscosity) which are not readily available in a laboratory setting. Therefore, if the Lighthill stress tensor is to be simplified in a way that it comprise only those properties that can be measured directly in a laboratory, then it is of interest to determine the inaccuracies that may arise due to the neglect of these other terms.

Beginning with the viscous stress tensor, Freund (2003)[3] showed that, even at low Reynold's numbers, jet noise could be considered an inviscid process and that τ_{ij} was indeed negligible. Likewise, for mildly heated jets, it has been argued that $(p - c_o^2 \rho)$ could be neglected. Furthermore, if the source region can be considered incompressible, then, in combination with the aforementioned assumptions, the Lighthill stress tensor reduces to $T_{ij} \approx \tilde{u}_i \tilde{u}_j$. The last of these tends to be a limiting condition as most jet noise studies are targeted for transonic and even supersonic regimes.[15] In what follows, a direct assessment of these assumptions will be studied by comparing the topography of the original Lighthill source term from (2) alongside this simplified model.

B.   Seiner's "Rational" Approach

Beginning with the divergence of the two-point velocity correlation, it follows from Tennekes & Lumley (1972)[17] that,

$$\begin{aligned}
\frac{\partial}{\partial x_j}(\tilde{u}_i \tilde{u}_j) = \tilde{u}_j \frac{\partial \tilde{u}_i}{\partial x_j} &= \tilde{u}_j \left(\frac{\partial \tilde{u}_i}{\partial x_j} - \frac{\partial \tilde{u}_j}{\partial x_i} \right) + \tilde{u}_j \frac{\partial \tilde{u}_j}{\partial x_i} \\
&= 2\tilde{u}_j r_{ij} + \frac{\partial}{\partial x_i}(\frac{1}{2}\tilde{u}_j \tilde{u}_j) \\
&= -\epsilon_{ijk} \tilde{u}_j \omega_k + \frac{\partial}{\partial x_i}(\frac{1}{2}\tilde{u}_j \tilde{u}_j)
\end{aligned} \tag{4}$$

2 of 9

American Institute of Aeronautics and Astronautics

where the first and second terms on the right hand side are the Lamb's vector and the dynamic pressure, respectively. One should immediately recognized that (4) is the convective stress term from the vorticity equation which is obtained by taking the curl of Navier Stokes. The significance of (4) is that it serves as In important reminder of the contribution to the convective terms in the equations of motion by the Reynolds stresses in the velocity fluctuations.[17] These inertia terms are gradients of stress which lends physical explanation to how sound is produced by changes in the eddy structure as it convects through the flow. By taking the divergence of (4), we see that,

$$\frac{\partial^2(\tilde{u}_i\tilde{u}_j)}{\partial x_i\partial x_j} = -\epsilon_{ijk}\frac{\partial\tilde{u}_j}{\partial x_i}\omega_k - \epsilon_{ijk}\tilde{u}_j\frac{\partial\omega_k}{\partial x_i} + \frac{1}{2}\frac{\partial^2\tilde{u}_j^2}{\partial x_i^2}, \tag{5}$$

which, upon further simplification, results in the following expression,

$$\begin{aligned}
\frac{\partial^2(\tilde{u}_i\tilde{u}_j)}{\partial x_i\partial x_j} &= \epsilon_{ijk}\frac{\partial\tilde{u}_i}{\partial x_j}\omega_k + \left(\frac{\partial\tilde{u}_i}{\partial x_j}\right)^2 \\
&= \epsilon_{ijk}(s_{ij}\omega_k + r_{ij}\omega_k) + \left(\frac{\partial\tilde{u}_i}{\partial x_j}\right)^2.
\end{aligned} \tag{6}$$

If, for the time being, we neglect the second term on the right-hand-side of (6) and turn our attention to the first term, we see that it comprises a sum of the strain rate (s_{ij}) and rotation rate (r_{ij}) tensors, which are typically the predominant terms in turbulent flows. According to the turbulent energy budget,[17] an average of these two terms should cancel because they are equal in magnitude but opposite in sign. However, instantaneously, they may not cancel, and their phase difference may yield an indicator for sound production following the postulations of Seiner (1998).[15] Upon further simplification, it can be shown that (6) transforms into the following expression,

$$\frac{\partial^2(\tilde{u}_i\tilde{u}_j)}{\partial x_i\partial x_j} = 2\left(\frac{\partial\tilde{u}_i}{\partial x_j}\frac{\partial\tilde{u}_j}{\partial x_i} - \frac{\partial\tilde{u}_i}{\partial x_i}\frac{\partial\tilde{u}_j}{\partial x_j}\right). \tag{7}$$

Our intention is to use (7) as an indicator of sound production in high speed volumetric PIV data. This approach bypasses the restrictive assumption that jet flows are isotropic, by applying the double divergence directly to Lighthill's stress tensor, rather than the Green's function; see Goldstein (1976) and Tam (1998).[16] The latter is typically solved using Batchelor's (1960) expression for isotropic turbulence that uses fourth order turbulent stresses expressed as products of second order stresses. Jordan et al.(2004)[6] and Ukeiley et al.(2007)[18] have shown the two-point correlations in jet flows to be highly anisotropic. To test the viability of this approach, the topography of the right hand side of (1) using the full expression for T_{ij} will be analyzed alongside that of (7).

III.   Overview of LES

The primary restriction to creating Large Eddy Simulations of jet flows at Reynolds numbers that are of practical interest continues to be the availability and efficiency of modern day computational resources. It is well known that the near field evolution, downstream development, and noise characteristics of a jet are all strongly affected by the characteristics of the turbulence at the nozzle exit. This can only be realized by developing methods capable of providing realistic boundary conditions to the LES.

Accurate boundary conditions for LES are provided in one of two ways: (a) the nozzle geometry must be included in the simulations or, (b) accurate time dependent boundary conditions must be utilized. By utilizing the former of the two results in a dramatic increase in mesh size. For this reason, alternate methods that use either synthesized turbulence or an excitation of the first few jet modes have been developed. The latter of these relies on the sensitivity of the predicted turbulence field to perturbations in the jet inflow conditions. Unfortunately there is no consensus as to the most appropriate approach to perturbing these jet inflow conditions. Furthermore, these methods are not applicable when noise-suppression devices are being studied since the natural modes are different and unknown. As a promising alternative, CRAFT Tech has developed a novel hybrid RANS/LES method that makes use of the upstream RANS nozzle exit profiles and turbulence description as boundary conditions for a LES of the downstream jet. This allows for a smooth transition of the subgrid eddy viscosity from within the nozzle boundary layer to the LES. A crucial feature

of the implementation process is the exploitation of time-scales already modeled by the $k - \epsilon$ model in the inertial regime of the turbulence wave number spectrum. Thus, only the predicted largest scales within the jet require resolution using fine grids.

As for predictions of the far-field noise produced by the simulated jet, CRAFT Tech implements integral acoustic solvers. The most promising of these is Kirchhoff's method combined with the porous Ffowcs-Williams and Hawkings (FW-H) equations. The FW-H formulation allows surface integrals to be calculated on a permeable integration surface that is not necessarily coincident with a solid body surface. Both methods consist of a direct numerical calculation of the non-linear near- and mid-field, with the far-field solutions obtained from an integral formulation using all quantities evaluated on a control surface. This control surface is designated as the Acoustic Data Surface (ADS), and is chosen such that it surrounds the entire source field of the jet and where wave propagation is linear. These methods have a definite advantage over the traditional acoustic analogy approach that requires complex volume integrals. Both methods (Kirchhoff and FW-H) can also be extended in order to include refraction effects outside the control surface. The placement of the ADS is an important consideration when coupling the LES with the FW-H equation. Outside of the nonlinear turbulent mixing region of the jet, the velocity divergence is related to the time derivative of pressure as is visualized in figure 1a. The placement of the Kirchhoff surface is based on a user defined threshold of the

(a)   (b)
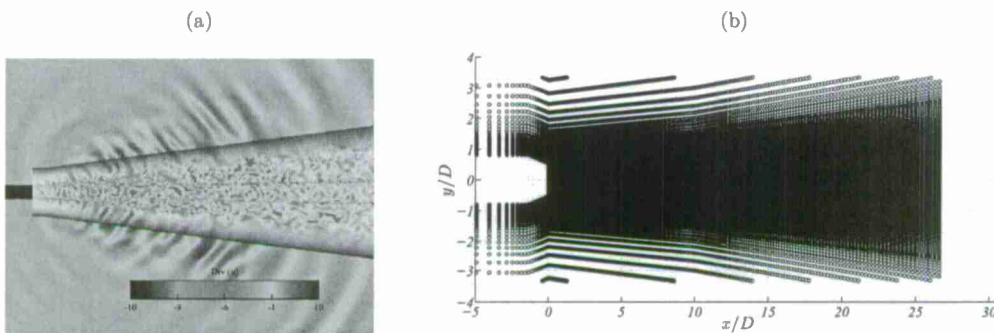
Figure 1. Divergence of the velocity field used to define the boundaries of the Kirchhoff surface for the LES model.

vorticity magnitude that was found to provide reasonable results of the far-field pressure. One can clearly see that the region where the ADS resides (shaded gray) is appropriate. A known complication with employing data surfaces such as the one shown here in figure 1a is in how one goes about treating the end surfaces where the jet exits the computational domain. By placing a surface along the end of the computational domain and across regions in the flow where the pressure perturbations are nonlinear, the FW-H assumptions would be violated. Therefore, the end surface is left open which also means that the contribution from noise at low angles is not captured. As most observer angles of interest are not directly downstream of the jet, but rather at an elevated angle, the inability of this model to capture sound waves propagating downstream is not necessarily problematic. The last concern regarding the ADS is its spatial resolution. It is necessary that the LES grid along the ADS be fine enough to capture the maximum frequency of interest. For problems in jet noise, the number of grid points would be significantly increased. The acoustic calculations are limited to the maximum frequency that the LES grid resolves. It is self-evident then that a fair amount of subjectivity and experience drives one's decision regarding the spatial resolution and location of the ADS for the jet flowfield under study.

The CRAFT CFD code is a structured Navier-Stokes solver that uses an upwind differencing scheme that is fifth order accurate in space and a four stage Runge-Kutta algorithm for time marching. The code is highly parallelized using domain decomposition, with close to linear speed-up parallel performance on several large supercomputers for very large grids. A traditional O-H type grid is used in the current effort and is illustrated in figure 1b. This prevents the ambiguity of centerline pole treatment, and also allows for a higher degree of resolution to be clustered along the nozzle lip of axisymmetric nozzles. In the current effort, the time step for the CFD simulations are selected to be 5.0e-8 seconds. For farfield noise and beamforming

calculations, a sample rate of 200 kHz was determined to be satisfactory, and hence time resolved data on the ADS was saved every 100 CFD timesteps. Several different nozzle configurations and jet exit conditions were modeled and tested. This comprised nozzles with and without a center-body upstream of the throat, as well as over-expanded and fully-expanded flows. For the time being. our analysis focuses on a fully-expanded jet with center-body. A tabulation of the operating conditions based on quasi 1-d isentropic compressible flow equations is provided in table 1 using subscripts j, ∞, 0 to denote jet–exit (static), ambient and stagnation conditions, respectively. The working gas is air (R = 287.05 [J/kg/K]) and the Mach wave radiation angle is based on an average convective speed of $U_c = 0.80 U_j$. Estimates of the supersonic core ($L_s = x_s/D_j$) and potential core ($L_c = x_c/D_j$) lengths of the jet are based on ($L_s = 5.0 M_j^{1.8} + 0.8$) and ($L_c = L_s/(M_j^{0.90})$), following the work of Varnier (2001).[19]

NPR	5.21	$\dot{m}$[kg/s]	0.9578	ρ_j/ρ_∞	0.46
D_j [m]	0.0508	U_j [m/s]	876.6	a_j/a_∞	1.46
T_0 [K]	1005	M_j	1.74	ϕ[deg]	60.55
T_j [K]	643	M_a	2.54	L_c	8.7
T_∞ [K]	293			L_s	14.4

Table 1. Performance properties of the nozzle based on quasi 1-d isentropic compressible flow equations.

A sample snapshot of the instantaneous streamwise velocity (U_1/U_∞) is shown in figure 2a alongside the instantaneous density field ($\rho[kg/m^3]$) in figure 2b. A first observation of the density field is the striking

(a)

(b)
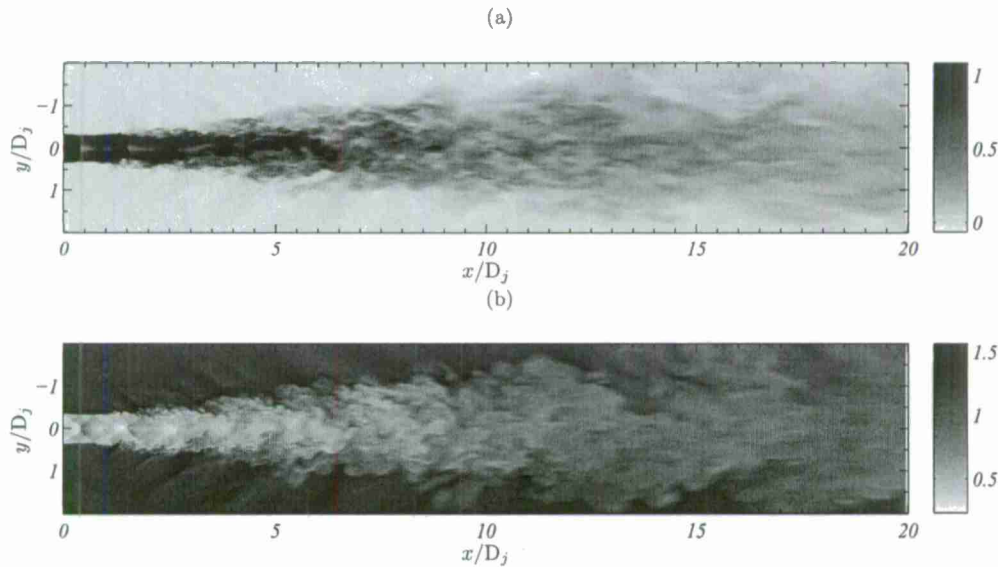
Figure 2. Snapshot of the instantaneous (a) streamwise velocity (U/U_∞) and (b) density field along the centerplane of the LES with centerbody and operating under fully-expanded exit conditions.

appearance of Mach waves. These waves proceed from an area located near the low speed entrainment regions of the flow at three nozzle diameters from the jet exit. and propagate at steep angles away from the jet axis; their intensity rapidly decays beyond this angle. Furthermore, both figures depict free shear layers that remain steady up to about three nozzle diameters from the jet exit plane, after which turbulent vortical structures begin to form. Mixing initially occurs in the annular shear layer and eventually extends until it fills the entire jet at a distance of about $7D_j$, at which point, the potential core collapses. These Mach waves are classified as a component of the turbulent mixing noise produced by supersonic jets and act to produce

5 of 9

American Institute of Aeronautics and Astronautics

highly directive sound waves along the Mach wave radiation angle.[2] The steady behavior of the free shear layer is expected within the first few diameters due to the very nature of the simulation: the mixing is in fact triggered through a perturbation of the exiting flow. Shock cells are observed and comprise both oblique and expansion waves that form diamond shaped patterns that remain visible until the end of the potential core region around $8D_j$. Expansion and contraction of theses cells due to interactions with the turbulence in the shear layer and hydrodynamic core results in broadband shock noise.

A. Model validation

An effort is made to compare the statistical properties of the near and far-field predictions to concurrent measurements of the same flow acquired at the NCPA of the University of Mississippi. A more thorough review of these measurements can be found in Murray *et al.* (2012)[12] who showed the effect of a centerbody and faceted internal geometry on the near and far-field pressure. In particular, the center-body was found to increase the broadband shock noise signature registered by both near and far-field microphone arrays located at steep and sideline angles to the jet axis. A comparison of the total pressure along the centerline of the jet between model and experiment is shown in figure 3a using measurements from a pitot probe comprising a 3.175 mm hole. Both data sets have been adjusted as needed using normal shock corrections. The LES appears to properly capture the shock cell spacing within the first six diameters, albeit the model depicts a shorter potential core downstream. This is attributed to the courser grid used to model the downstream regions of the flow as seen in figure 1b and was done in an effort to reduce computational cost. The effect of the center-body on the shear layer growth and potential core length is shown in figure 3b to have only a minor effect.
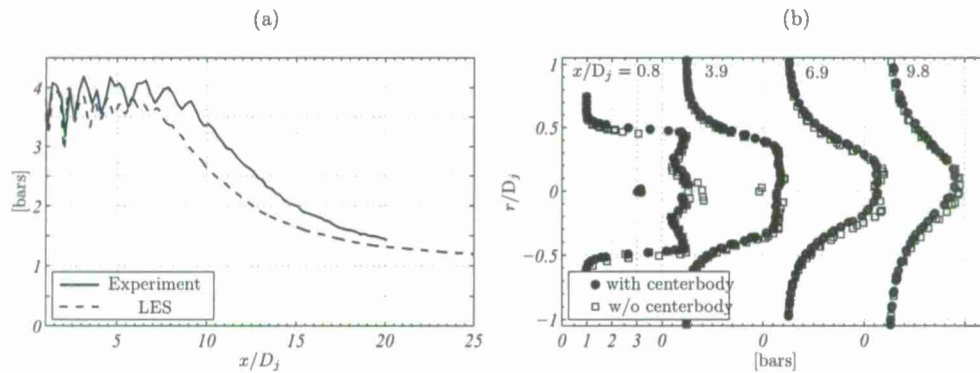
Figure 3. Comparison of (a) total pressure along the centerline of the jet and (b) radial profiles of the total pressure at various positions downstream of the nozzle.

As for the far-field pressure, a comparison of the OASPL and SPL are shown in figures 4a and 4b, respectively. The predicted OASPL appears to agree with laboratory measurements to within 2-3dB or so and over a broad range of angles. The more rapid drop off at shallow angles is attributed to the shape and placement of the Kirchhoff surface. A closer inspection reveals how the prominent directivity resides around 45° to the jet axis. An estimate of the Mach wave radiation angle in table 1 was found to reside at 60° to the jet axis. This suggest that the source region is located downstream of the jet exit in the post-potential core regions of the flow. Likewise, a prediction of the peak frequency in the SPL at the peak directivity observer location is shown to resemble the measured spectra. Elevated noise levels found in the higher frequencies are attributed to artificial noise.

IV. Preliminary results

For the time being, only a slice of the sound production indicator obtained from direct application of (7) to the LES is presented. This is shown in figure 5 along the center plane of the jet axis. The supposed sound
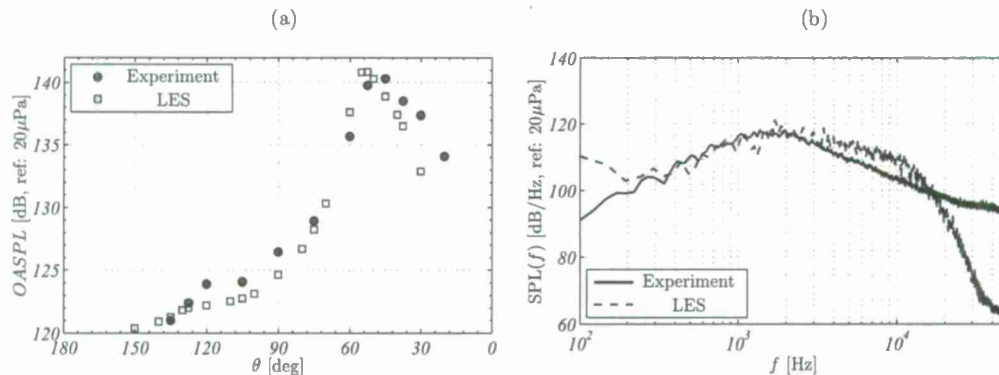
Figure 4. Comparison of (a) OASPL and (b) SPL at $\theta = 45°$ and $r/D_j = 55$ between experiment and LES model prediction.

indicators are shown to reside along the lip line of the nozzle where turbulence kinetic energy is expected to be greatest. This demonstrates the physical significance of this metric, albeit, a scrutiny of these results is currently underway, the findings of which will be the focus of the final paper. Likewise, application of this metric to a fully three-dimensional LES is currently underway, as well as methods for reducing artificially generated noise produced by the double divergence of the model parameters. The elevated noise produced by the double divergence of the velocity field is greatest near the nozzle exit where the ratio of the turbulence length scale to grid scale is small. The full paper will encompass an effort to better understand this new sound production indicator in order to determine its usefulness in upcoming PIV studies to be performed at NCPA of the same high speed jet flow.
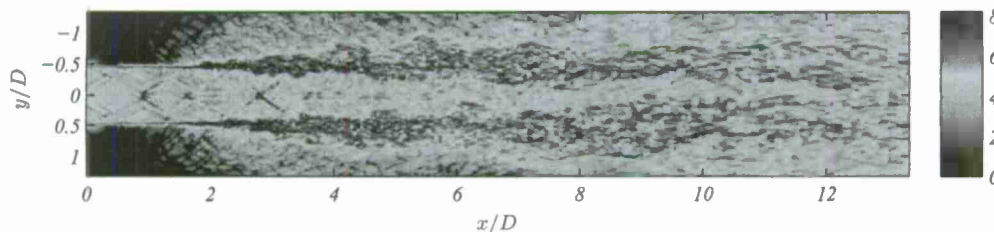
Figure 5. Instantaneous snapshot of the sound production indicator along a slice of the jet.

V. Acknowledgments

VI. Appendix

Below are presented the calculations and simplifications of the double divergence formula (5) that leads to (6) and the new formula (7).

First we develop every right-side term of (5) for the three spatial velocities :

$$-\epsilon_{ijk}\frac{\partial \tilde{u}_j}{\partial x_i}\omega_k = \epsilon_{jik}\frac{\partial \tilde{u}_j}{\partial x_i}\omega_k = \epsilon_{ijk}\frac{\partial \tilde{u}_i}{\partial x_j}\omega_k, \tag{8}$$

and so pursuing by developing the terms for the three spatial velocities :

$$\epsilon_{ijk}\frac{\partial \tilde{u}_i}{\partial x_j}\omega_k = \left(\frac{\partial \tilde{u}}{\partial y} - \frac{\partial \tilde{v}}{\partial x}\right)\omega_z + \left(\frac{\partial \tilde{w}}{\partial x} - \frac{\partial \tilde{u}}{\partial z}\right)\omega_y + \left(\frac{\partial \tilde{v}}{\partial z} - \frac{\partial \tilde{w}}{\partial y}\right)\omega_x = -(\omega_x^2 + \omega_y^2 + \omega_z^2), \tag{9}$$

as the vorticity is defined as such :

$$\omega_k = \frac{\partial \tilde{u}_j}{\partial x_i} - \frac{\partial \tilde{u}_i}{\partial x_j}. \tag{10}$$

Now we develop the second term of (5) :

$$\begin{aligned}
-\epsilon_{ijk}\tilde{u}_j\frac{\partial \omega_k}{\partial x_i} &= \tilde{u}\left(\frac{\partial \omega_z}{\partial y} - \frac{\partial \omega_y}{\partial z}\right) + \tilde{v}\left(\frac{\partial \omega_x}{\partial z} - \frac{\partial \omega_z}{\partial x}\right) + \tilde{w}\left(\frac{\partial \omega_y}{\partial x} - \frac{\partial \omega_x}{\partial y}\right) \\
&= \tilde{u}\left(\frac{\partial^2 \tilde{v}}{\partial x \partial y} + \frac{\partial^2 \tilde{w}}{\partial x \partial z} - \frac{\partial^2 \tilde{u}}{\partial y^2} - \frac{\partial^2 \tilde{u}}{\partial z^2}\right) + \tilde{v}\left(\frac{\partial^2 \tilde{u}}{\partial x \partial y} + \frac{\partial^2 \tilde{w}}{\partial y \partial z} - \frac{\partial^2 \tilde{v}}{\partial x^2} - \frac{\partial^2 \tilde{v}}{\partial z^2}\right) \\
&\quad + \tilde{w}\left(\frac{\partial^2 \tilde{u}}{\partial x \partial z} + \frac{\partial^2 \tilde{v}}{\partial z \partial z} - \frac{\partial^2 \tilde{w}}{\partial x^2} - \frac{\partial^2 \tilde{w}}{\partial y^2}\right),
\end{aligned} \tag{11}$$

now we can use the assumption of incompressibility to use the fact that every derivative of the divergence of the velocity is equal to zero. Therefore we have :

$$\begin{aligned}
\frac{\partial^2 \tilde{u}}{\partial x^2} &= -\frac{\partial^2 \tilde{v}}{\partial x \partial y} - \frac{\partial^2 \tilde{w}}{\partial x \partial z} \\
\frac{\partial^2 \tilde{v}}{\partial y^2} &= -\frac{\partial^2 \tilde{u}}{\partial x \partial y} - \frac{\partial^2 \tilde{w}}{\partial y \partial z} \\
\frac{\partial^2 \tilde{w}}{\partial z^2} &= -\frac{\partial^2 \tilde{u}}{\partial z \partial x} - \frac{\partial^2 \tilde{v}}{\partial z \partial y},
\end{aligned} \tag{12}$$

and we can replace second derivatives in (11) in order to obtain :

$$-\epsilon_{ijk}\tilde{u}_j\frac{\partial \omega_k}{\partial x_i} = -\tilde{u}\left(\frac{\partial^2 \tilde{u}}{\partial x^2} + \frac{\partial^2 \tilde{u}}{\partial y^2} + \frac{\partial^2 \tilde{u}}{\partial z^2}\right) - \tilde{v}\left(\frac{\partial^2 \tilde{v}}{\partial x^2} + \frac{\partial^2 \tilde{v}}{\partial y^2} + \frac{\partial^2 \tilde{v}}{\partial z^2}\right) - \tilde{w}\left(\frac{\partial^2 \tilde{w}}{\partial x^2} + \frac{\partial^2 \tilde{w}}{\partial y^2} + \frac{\partial^2 \tilde{w}}{\partial z^2}\right). \tag{13}$$

Then we develop the dynamic pressure term (neglected in Seiner's approach):

$$\begin{aligned}
\frac{1}{2}\frac{\partial^2 \tilde{u}_j^2}{\partial x_i^2} &= \frac{1}{2}\left(\frac{\partial^2 \tilde{u}^2}{\partial x^2} + \frac{\partial^2 \tilde{u}^2}{\partial y^2} + \frac{\partial^2 \tilde{u}^2}{\partial z^2} + \frac{\partial^2 \tilde{v}^2}{\partial x^2} + \frac{\partial^2 \tilde{v}^2}{\partial y^2} + \frac{\partial^2 \tilde{v}^2}{\partial z^2} + \frac{\partial^2 \tilde{w}^2}{\partial x^2} + \frac{\partial^2 \tilde{w}^2}{\partial y^2} + \frac{\partial^2 \tilde{w}^2}{\partial z^2}\right) \\
&= \left(\frac{\partial \tilde{u}}{\partial x}\right)^2 + \left(\frac{\partial \tilde{v}}{\partial x}\right)^2 + \left(\frac{\partial \tilde{w}}{\partial x}\right)^2 + \left(\frac{\partial \tilde{u}}{\partial y}\right)^2 + \left(\frac{\partial \tilde{v}}{\partial y}\right)^2 + \left(\frac{\partial \tilde{w}}{\partial y}\right)^2 + \left(\frac{\partial \tilde{u}}{\partial z}\right)^2 + \left(\frac{\partial \tilde{v}}{\partial z}\right)^2 + \left(\frac{\partial \tilde{w}}{\partial z}\right)^2 \\
&\quad + \tilde{u}\left(\frac{\partial^2 \tilde{u}}{\partial x^2} + \frac{\partial^2 \tilde{u}}{\partial y^2} + \frac{\partial^2 \tilde{u}}{\partial z^2}\right) + \tilde{v}\left(\frac{\partial^2 \tilde{v}}{\partial x^2} + \frac{\partial^2 \tilde{v}}{\partial y^2} + \frac{\partial^2 \tilde{v}}{\partial z^2}\right) + \tilde{w}\left(\frac{\partial^2 \tilde{w}}{\partial x^2} + \frac{\partial^2 \tilde{w}}{\partial y^2} + \frac{\partial^2 \tilde{w}}{\partial z^2}\right).
\end{aligned} \tag{14}$$

Finally we can notice that by doing the summation of the different terms in (5) and by developing the square of the different vorticities we get the following expression which correspond to (6) in Einstein notations:

$$\begin{aligned}
\frac{\partial^2 (\tilde{u}_i \tilde{u}_j)}{\partial x_i \partial x_j} &= \left(\frac{\partial \tilde{u}}{\partial x}\right)^2 + \left(\frac{\partial \tilde{v}}{\partial y}\right)^2 + \left(\frac{\partial \tilde{w}}{\partial z}\right)^2 + 2\frac{\partial \tilde{u}}{\partial y}\frac{\partial \tilde{v}}{\partial x} + 2\frac{\partial \tilde{v}}{\partial z}\frac{\partial \tilde{w}}{\partial y} + 2\frac{\partial \tilde{w}}{\partial x}\frac{\partial \tilde{u}}{\partial z} \\
&= \epsilon_{ijk}\frac{\partial \tilde{u}_i}{\partial x_j}\omega_k + \left(\frac{\partial \tilde{u}_i}{\partial x_j}\right)^2.
\end{aligned} \tag{15}$$

8 of 9

This formulation reveals the presence of the strain and rotational tensors and allows to make an analogy with Seiner's theory in (??). Nevertheless there is a way to obtain a more convenient formula for post-processing the data of the LES by using again the incompressibility assumption. In fact we can consider that the square of the velocity divergence is equal to zero :

$$(\frac{\partial \tilde{u}}{\partial x} + \frac{\partial \tilde{v}}{\partial y} + \frac{\partial \tilde{w}}{\partial z})^2 = 0$$

i.e.

$$(\frac{\partial \tilde{u}}{\partial x})^2 + (\frac{\partial \tilde{v}}{\partial y})^2 + (\frac{\partial \tilde{w}}{\partial z})^2 = -2\frac{\partial \tilde{u}}{\partial x}\frac{\partial \tilde{v}}{\partial y} - 2\frac{\partial \tilde{v}}{\partial y}\frac{\partial \tilde{w}}{\partial z} - 2\frac{\partial \tilde{w}}{\partial z}\frac{\partial \tilde{u}}{\partial x}.$$

(16)

The next step is to insert (16) into (15) to get :

$$\frac{\partial^2(\tilde{u}_i\tilde{u}_j)}{\partial x_i \partial x_j} = 2(\frac{\partial \tilde{u}}{\partial y}\frac{\partial \tilde{v}}{\partial x} - \frac{\partial \tilde{u}}{\partial x}\frac{\partial \tilde{v}}{\partial y}) + 2(\frac{\partial \tilde{v}}{\partial z}\frac{\partial \tilde{w}}{\partial y} - \frac{\partial \tilde{v}}{\partial y}\frac{\partial \tilde{w}}{\partial z}) + 2(\frac{\partial \tilde{w}}{\partial x}\frac{\partial \tilde{u}}{\partial z} - \frac{\partial \tilde{w}}{\partial z}\frac{\partial \tilde{u}}{\partial x}),$$

(17)

which corresponds in Einstein notation to the final convenient formula (7) :

$$\frac{\partial^2(\tilde{u}_i\tilde{u}_j)}{\partial x_i \partial x_j} = 2(\frac{\partial \tilde{u}_i}{\partial x_j}\frac{\partial \tilde{u}_j}{\partial x_i} - \frac{\partial \tilde{u}_i}{\partial x_i}\frac{\partial \tilde{u}_j}{\partial x_j})$$

(18)

References

[1] BAARS, W. J., TINNEY, C. E., MURRAY, N. E., JANSEN, B. J. & PANICKAR, P., 2011 The Effect of Heat on Turbulent Mixing Noise In Supersonic Jets. *AIAA Paper 2011-1029*.

[2] BAARS, W. J., TINNEY, C. E. & WOCHNER, M.S., 2012 Nonlinear propagation of sound from a Fully Expanded Mach 3 Jet. *AIAA Paper 2012-1177*.

[3] FREUND, J.B. 2003 Noise-Source Turbulent Statistics and the Noise from a Mach 0.9 Jet. *Phys. Fluids* 15:6, 1788–1799.

[4] GEORGE, W.K., WÄNSTRÖM, M. & JORDAN, P. 2007 Identifying aeroacoustic sources. 13th *AIAA/CEAS Aeroacoustics Conference*. Paper AIAA-2007-3603, Rome.

[5] GOLDSTEIN, M. 2003 A generalized acoustic analogy. *J. Fluid Mech.* 488, 315–333.

[6] JORDAN, P. & GERVAIS, Y. 2004 Modelling self- and shear-noise mechanisms in inhomogeneous, anisotropic turbulence. *J. Sound & Vib.* 279, pp. 529–555.

[7] JORDAN, P. & GERVAIS, Y. 2008 Subsonic jet aeroacoustics: associating experiment, modelling and simulation. *Exp. Fluids.* 44:1, 1–21.

[8] LIGHTHILL, M.J. (1952) On sound generated aerodynamically. Part I. General Theory. *Proc. Royal Society, London A* 211, 564–587.

[9] LIGHTHILL, M.J. (1954) On sound generated aerodynamically. Part II. Turbulence as a source of sound. *Proc. Royal Society, London A* 222, 1–32.

[10] LILLEY, G.M. (1974) On the noise from jets. *Tech. Rep. CP-131, AGARD*

[11] MÖHRING, W. 1978 On vortex sound at low Mach numbers. *J. Fluid Mech.* 85, 685–691.

[12] MURRAY, N., LYONS, G., TINNEY, C.E., DONALD, B., BAARS, W., THUROW, B., HAYNES H. & PANICKAR, P., 2012 A laboratory framework for synchronous near/far-field acoustics and MHz PIV in high-temperature. shock-containing jets. *Proc. Internoise 2012 ASME NCAD meeting*. New York City, U.S.A., August 19-22

[13] POWELL, A. 1964 Theory of vortex sound. *J. Acoustical Society of America.* 36:1, 177–195.

[14] SCHRAM, C. & HIRSCHBERG, A. (2003) Application of vortex sound theory to vortex-pairing noise: sensitivity to errors in flow data. *J. Sound & Vib.* 266, 1079–1098.

[15] SEINER (1998) A rational approach to jet noise reduction. *Theor. Comp. Fluid Dyn.* 10, 373–383.

[16] TAM, C. K. W. 1998 Jet Noise: Since 1952. *Theor. Comp. Fluid Dyn.* 10, 393–405.

[17] TENNEKES, H. & LUMLEY, J. L. 1972 A first course in turbulence. *MIT Press*.

[18] UKEILEY, L.S., TINNEY, C.E., MANN, R. & GLAUSER, M.N. 2007 Spatial correlations in a transonic jet. *AIAA J.* 45:6, 1357–1369.

[19] VARNIER, J., 2001 Experimental study and simulation of rocket engine freejet noise. *AIAA J.* 39:10, 1851–1859.

Appendix G: Manuscript Submitted to *J. Fluid Mech.*

1

Nonlinear distortion of acoustic waveforms from high-speed jets

W. J. BAARS[1]†, C. E. TINNEY[1] AND M. S. WOCHNER[2]

[1]Department of Aerospace Engineering & Engineering Mechanics, University of Texas at Austin, Austin, TX 78712, USA

[2]Applied Research Laboratories, University of Texas at Austin, Austin, TX 78713, USA

An empirical model for predicting the presence of cumulative nonlinear distortions in the acoustic waveforms produced by high speed jet flows is proposed. The model accounts for the effects imposed by jet exit conditions of practical interest and is based upon historical relationships to determine the ratio between shock formation distance and viscous absorption length. The model is shown to scale with Mach number, temperature ratio, Strouhal number and an absolute observer distance relative to a broadband Gaussian source. Surveys of the far-field pressure produced by a laboratory-scale, shock free and unheated Mach 3 jet flow are used to support the findings of the model. These acoustic waveforms are acquired on a 2D grid in an acoustically treated and range–restricted environment. Various statistical metrics are employed to examine the degree of local and cumulative nonlinearity in the measured waveforms and their temporal derivative. This includes the number of zero crossings, a wave steepening factor, Skewness, Kurtosis, the Morfey-Howell nonlinearity indicator and an application of the generalized Burgers equation. It is advocated that in order for the Morfey-Howell indicator to be used as an investigative tool for the presence of cumulative nonlinear waveform distortion, that it be applied as a multi-point indicator along a propagation path that abides by spherical spreading laws.

Key words:

1. Preface

In supersonic jets, an extended line of distributed sources act in compliance to generate and propagate noise in a complex manner to an observer far away from the jet. Nonlinear distortion of the acoustic waveform is often considered a prerequisite to understanding this propagation process. This is driven by one's capture of 'shock-type' structures or so called 'N-wave' like signatures in the pressure waveform, which are generally attributed to nonlinear wave steepening. Likewise, imperfect collapse of the spectra between an observer signal and a prediction, formed from a linear rescaling of the closer signal (using $1/r^2$ dependence), is also often believed to be caused by nonlinear distortion. Unfortunately, these observations are most often made using measurements acquired in a range-restricted environment where changes to the waveform, due to cumulative nonlinear distortion, are too small to be accurately quantified, and/or without prior knowledge of the sound propagation path. The current work aims to fill this gap

† Email address for correspondence: baars@utexas.edu

2   *W. J. Baars, C. E. Tinney and M. S. Wochner*

by exploring the acoustic field produced by an unheated, perfectly expanded, Mach 3 jet in a laboratory–scale environment, of which there are several scientific advantages. Foremost, the nozzle produces a shock-free flow when operated at its design point which eliminates the other sources of supersonic jet noise associated with screech and broad-band shock noise. Furthermore, the convective and acoustic Mach numbers for this flow are 1.4 and 1.8, respectively, which ensures the formation of strong Mach waves; this ultimately increases the level of waveform distortion.

The study is broken into two parts. Part 1 focuses on a time-averaged approach to understanding the degree of non-linearity in the acoustic waveform at several far-field observer positions. Various "off-the-shelf" indicators are explored including a new model for predicting the presence (or lack there of) of cumulative non-linear waveform distortion in the signal. In part 2, temporal changes to the waveform are preserved in order to explore the signal in terms of its time-frequency distribution. This is done in an effort to filter out the distorted acoustic waveform from the background signatures in order to better understand the statistical properties of these shock-type structures.

2. Introduction

2.1. *A review of research on supersonic jet noise*

Several experimental and numerical studies have been conducted over the past four decades to understand the noise produced by supersonic jet flows. These have com-prised a plethora of conditions including temperature effects, perfectly and imperfectly expanded flows, circular, elliptical and faceted geometries, as well as multi-stream nozzle assemblies. Restricting one's attention to shock-free, unheated supersonic jet flows, the more relevant stacks of literature reduce to the laboratory-scale jet studies of McLaughlin *et al.* (1975), Tanna & Dean (1975), the full-scale flight tests of Morfey & Howell (1981) or the numerical studies of Howell & Morfey (1987), Morris (1977) and Seiner *et al.* (1994). The aforementioned work comprised spectral analysis of the far-field acoustic waveform produced by jets with supersonic exit speeds based on the gas dynamic Mach number ($M_j = U_j/a_j > 1$). The work of Papamoschou *et al.* (2010), McLaughlin *et al.* (2010) and Baars *et al.* (2011) comprised supersonic jets in terms of the acoustic Mach number ($M_a = U_j/a_\infty > 1$); this definition of the jet Mach number is most rele-vant to the formation of Mach waves. Aside from conventional spectral analysis, Laufer *et al.* (1976), Gallagher (1982), Petitjean *et al.* (2006) and Veltin *et al.* (2011) studied the temporal characteristics of the acoustic pressure waveform in a laboratory (range-restricted) environment while Gee *et al.* (2008) focused on the nonlinear propagation effects of a full-scale static jet engine and compared the experimental data successfully to a numerical model based on the generalized Burgers equation. Some of the more rele-vant numerical studies include the large-eddy simulation of an overexpanded Mach 3.3 jet by de Cacqueray *et al.* (2011*b*) as well as the frequency-domain algorithm for simulating nonlinear noise propagation by Saxena *et al.* (2009). Where the development of robust acoustic analogies are concerned, one may wish to review the work of Morris & Farassat (2002), Tam *et al.* (2008), Tam (2009) and Morris (2009). As for rocket launch vehicle noise, McInerny (1996) and McInerny & Ölçmen (2005) studied the formation of shocks found in the acoustic far-field regions of an engine during start-up; rocket acoustics has received considerably less attention due to the large back pressures required to produce these conditions.

Unlike subsonic jets, the noise produced by a supersonic jet flow can be categorized into three distinct mechanisms (Tam 1995): turbulent mixing noise, broadband shock-

Nonlinear distortion of acoustic waveforms from high-speed jets   3
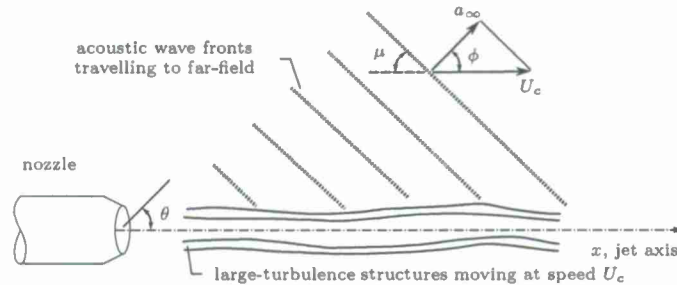
FIGURE 1. Simplified schematic of the Mach wave radiation mechanism in the near-field of the supersonic jet (ambient sound speed a_∞ and convective speed U_c of the instability waves).

associated noise and screech tones. The latter two occur when shock structures are present in the plume. It has been postulated for quite some time that turbulent mixing noise consists of two components. The first and most distinguishable component is generated by the (often supersonic) convective motion of large turbulent structures or instability waves that pass along the potential core region of the flow, whereas the second component is believed to be associated with the fine-scale turbulence within the shear layer.

Where the large-scales are concerned, various families of instability waves have been observed; this was originally addressed in the work of Oertel and then later by Tam & Hu (1989). One particular family of instability waves act as surface panels convecting at supersonic speeds that radiate waves at the Mach cone half angle: $\phi = \pi/2 - \mu = \pi/2 - sin^{-1}(a_\infty/U_c)$ as is shown in figure 1. Highly directive and intense noise patterns appear due to a radiation process known as a *super directive pattern*. This pattern forms within the zone of action where acoustic radiation becomes increasingly intense as the convective Mach number of the turbulent large-scale structures move at supersonic speeds relative to the ambient. Between the zones of action and silence, the intensity of these radiating waves rapidly decays. Phillips (1960) first described these radiating waves as 'Mach waves' and addressed the significance of Mach wave radiation produced by (cylindrical) supersonic shear layers. Ffowcs Williams & Maidanik (1965) focussed on similar annular shear flows from the exhaust of rockets. Analytical models for the radiation process were developed early on by these authors, but few reliable experiments were available at that time to verify their accuracy. A decade later the noise produced by Mach waves became the subject of numerous investigations (McLaughlin *et al.* 1975; Laufer *et al.* 1976; Seiner *et al.* 1994; Tam & Chen 1994; Tam *et al.* 2008; Tam 2009). This is attributed to the fact that the noise produced by Mach waves is the dominant component of turbulent mixing noise and therefore researchers have attempted to tackle this component in order to achieve significant jet noise reduction (Papamoschou & Debiasi 1999, 2001). Several factors believed responsible for influencing the radiation mechanisms associated with Mach waves are (1) growth, saturation and decay of the instability waves along the jet axis, (2) the non-uniform and frequency dependent convective speeds of the large scale structures, and (3) additional factors such as acoustic refraction in the case of non-isothermal jets. While a simplified illustration of the formation of Mach waves from a high speed jet flow is shown in figure 1, the complexity is well visualized in, for example, the experiments of Clemens & Paul (1993) on a perfectly expanded Mach 2 helium jet or the direct numerical simulation of a perfectly expanded Mach 1.92 jet flow by Freund *et al.* (2000). Insightful snapshots of the far-field pressure produced by Mach waves can be seen in the recent simulations by de Cacqueray *et al.* (2011a).

The other component of turbulent mixing noise, associated with the fine-scale tur-

4   *W. J. Baars, C. E. Tinney and M. S. Wochner*

bulence (Tam *et al.* 2005), causes an omni–directional propagation of sound and is the dominant source of noise at angles exceeding the Mach wave radiation angle. With these two components of noise revealed, the spectral features of the jet's far-field regions can be fitted to two universal, empirically derived, spectra associated with the two mixing noise components (Tam *et al.* 1996, 2008). At shallow angles, the spectra form a low-frequency hump due to the presence of Mach waves in the shear layer and is referred to as the Large Scale Similarity (LSS) spectrum. At angles beyond the Mach angle (sideline and upstream angles) the shape of the spectra resorts to a more broadband shape; this is reflective of the broadband nature of the fine-scale mixing noise and is characterized by the Fine Scale Similarity (FSS) spectrum. At intermediate angles a superposition of the LSS and FSS spectra can be matched to the observed spectrum.

2.2. *Nonlinear acoustics*

Nonlinear distortion of the acoustic waveform emanating from the source region is often considered a prerequisite to understanding the noise signature produced by a supersonic jet. However, there continues to be a lack of consensus on how these nonlinearities are manifest. A common method for determining if nonlinearities are present in the waveform is to project the spectra acquired from a *near* far-field observer to a *far* far-field observer using linear metrics and to compare the projected spectra to the actual measurement at that location (Viswanathan 2008). If spherical spreading laws and atmospheric absorption effects are properly accounted for then one is led to believe that the residual between the projected and measured waveforms are attributed to nonlinear distortion. This however, requires that the propagation path be known, which is rarely the case in most laboratory and full-scale jet studies due to the expense of acquiring multiple observer locations.

As a review, two types of nonlinear effects can affect the shape of an acoustic waveform, that is *local* and *cumulative*. Distortions that become more pronounced with propagation distance are considered *cumulative* and are the consequence of deviations in the particle velocity (U) over the waveform. These distortions include wave steepening, shock formation, viscous/atmospheric absorption, shock coalescence and relaxation. Wave steepening and shock formation result in a transfer of energy from mid frequencies to high frequencies. Likewise, stronger shocks that travel faster than weaker ones cause shocks to coalesce, thereby reducing the number of zero crossings; this is reflected by a shift of energy from mid frequencies to low frequencies. If viscous absorption permits, an overall broadening of the spectrum occurs. A classic illustration of the evolution of a sinusoidal waveform undergoing nonlinear distortion is shown in figure 2*(a)*. A more realistic illustration of a distorted acoustic waveform corresponding to a supersonic jet is shown in figure 2*(b)*. On average, waveform compressions are much stronger and occur over a shorter duration of time than waveform expansions. The large positive spikes in the pressure derivative are an indication of this. In general, cumulative effects dominate local effects. The latter being instantaneous effects such as a finite displacement of the source and, in the theoretical case, an actual nonlinearity of the pressure-particle velocity (impedance) relation. In the case of progressive waves, this component can often be neglected since the local distortion is only dominant in close proximity to the source.

Nonlinear acoustics is necessary once the small-signal assumption used for linear acoustics breaks down. That is, nonlinear terms need to be retained in the conservation equations thereby allowing the acoustic waveform to distort (Hamilton & Blackstock 2008). This can be seen in the seminal work of Pestorius & Blackstock (1974) which resulted in the development of methods capable of applying nonlinear acoustic theory to broadband signals. In particular, they applied a hybrid time-frequency algorithm that numerically solves the generalized Burgers equation. The method takes an input waveform from a

Nonlinear distortion of acoustic waveforms from high-speed jets   5

(a)   (b)
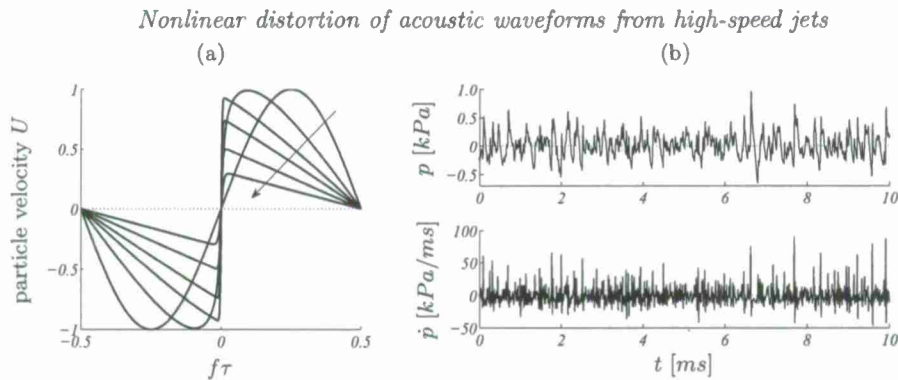
FIGURE 2. (a) Schematic of the distortion of an initial sinusoidal waveform with frequency f during nonlinear propagation including viscous absorption. A non-dimensional retarded time ($\tau = t - x/a_\infty$) is used on the x-axis. (b) Typical acoustic waveform of broadband jet noise *(top)* having instances of sharp compressions followed by gradual expansions. The time derivative of the waveform, $\dot{p}$, shows spikes where sharp compressions in the waveform occur *(bottom)*.

near far-field microphone and predicts the waveform at a position further out. The hybrid Burgers equation takes into account atmospheric absorption, molecular relaxation losses, nonlinearities, dispersion, and geometrical spreading and is written as follows:

$$\frac{\partial p}{\partial \tau} = \frac{\beta}{2\rho_0 a_\infty^3}\frac{\partial p^2}{\partial \tau} + \psi_\tau\{p\} - \frac{1}{r}p, \tag{2.1}$$

where p is acoustic pressure, r is the coordinate along the propagation path, $\beta = (\gamma+1)/2$ is the coefficient of nonlinearity, ρ_0 is ambient density, a_∞ is ambient sound speed, $\tau = t - x/a_\infty$ is retarded time, and ψ_τ is the atmospheric absorption and dispersion operator. The algorithms propagate input time waveforms in a stepwise manner by first applying a nonlinear distortion step using the Earnshaw solution (Hamilton & Blackstock 2008). Absorption, dispersion, and geometrical spreading losses are then accounted for in the frequency domain. Given sufficiently small spatial steps the time and frequency domain steps can be treated independently. In addition, the algorithm can be formulated to perform both linear and nonlinear predictions of the input waveform. For linear predictions, the first term on the right hand side of (2.1) is removed, thus allowing the propagation of the waveform between the first and second observer points to be fully calculated in the frequency domain and in one simple step. Pestorius & Blackstock (1974) focused their study on the propagation of a broadband noise pulse emitted by a high-intensity source in an air-filled progressive plane wave tube. Excellent agreement was achieved between the measured and computed waveforms at various locations downstream of the source. It was the first introduction of an algorithm capable of propagating arbitrarily shaped waveforms in one dimension while incorporating shock formation and relaxation effects.

Application of the generalized Burgers equation to problems in jet noise, however, has had limited success. Beginning with the pioneering work of Ffowcs Williams *et al.* (1975), the lack of cumulative waveform steepening in the pressure waveform was attributed to low amplitude levels at the source (based on private communication between Blackstock and Ffowcs Williams). Only in recent years, has a successful execution of this algorithm been performed on high speed jet flows and can be found in the work of Gee *et al.* (2008). In response to earlier failed attempts at using the generalized Burgers equation to study nonlinear distortions in the acoustic waveform from high speed jet flows, alternative methods where developed. One such approach can be found in the

6   *W. J. Baars, C. E. Tinney and M. S. Wochner*

work of Howell & Morfey (1987) who derived a nonlinear indicator based on (2.1); this is commonly referred throughout the literature as the *Morfey-Howell indicator*. In essence, this indicator is a measure of how the energy in the power spectrum is redistributed due to nonlinear distortion. A short coming of this indicator is that it requires one to compute the normalized quadrature spectral density whose amplitude is highly sensitive to the shape of the signal's Probability Density Function (PDF). We will show later on how successful execution of this technique to problems in jet noise demands a measure of the Morfey-Howell indicator at multiple points along the propagation path, which is rarely found in the literature. An extensive discussion and application of this indicator is presented in § 6.2.1.

Another widely used approach to study the nonlinear propagation of sound from high-speed jet flows involves computing near-field/far-field correlations using higher-order spectral analysis methods. Originally developed by the systems identification community, these techniques are designed to quantify nonlinear coupling in a single-input/output system. These bispectral methods identify nonlinearities by computing the quadratic bicoherence, which is essentially the second-order variant of the well-known linear coherence. By applying these techniques one can essentially identify the frequencies at which two signals are linearly and nonlinearly related (Gee *et al.* 2005, 2007*a*). Since the bispectral technique is an identification technique and does not provide the direct capability of estimation and prediction, another technique, developed in the field of system identification, was introduced which started with the work of Tick (1961). This higher-order estimation technique was presented recently in a paper by Baars *et al.* (2010) where it is combined with proper orthogonal decomposition to allow the application of this technique to sets of sensors in the near-field and far-field, thereby eliminating the limitation of single-sensor analysis. It is a promising technique but due to current limitations in processor power, the technique is confined to second order (quadratic) systems and low frequency resolution. A second difficulty arises due to convergence issues of higher-order spectral moments which casts doubts on one's ability to reveal the true nature by which the nonlinear distortion is manifest.

2.3. *Overview of current study*

While a great number of surveys have focused on noise from supersonic jets in general, very few have attempted to investigate nonlinear acoustic phenomena in a spatial domain covering the near- and far-field acoustic regions. Moreover, no studies have explicitly addressed the relationship between local and cumulative nonlinear acoustic distortion. In an effort to address these questions, the current study focuses on detailed measurements of the acoustic far-field regions of a perfectly expanded (shock-free plume) Mach 3 jet flow. This eliminates screech and the noise produced by turbulence interactions with shock cells. Aside from the rocket engine noise studies of McInerny (1996), Varnier (2001) and de Cacqueray *et al.* (2011*a*), the Mach number chosen for this study is not typical of commercial or military aircraft engines, and bears little relevance to most practical systems of engineering interest. However, the high Mach number results in a convective and acoustic Mach number around 1.4 and 1.8, respectively, which ensures the strong formation of Mach waves. We believe this can provide insightful information about how the sound propagates from lower supersonic Mach number jets, and even subsonic jet flows.

The measurements comprise temporal acoustic pressure waveforms acquired on a grid in the (x, r)-plane in order to quantify the topography of time-averaged signatures in the far-field of the jet. The study is unique in the sense that sufficient spatial information is available in order to make valid conclusions regarding propagation trends. This opposes

Nonlinear distortion of acoustic waveforms from high-speed jets   7

the majority of the studies where spatially isolated measurements along a single array or single point are considered. In the first part of the manuscript, § 4, the spectral features of the sound field from this Mach 3 jet are described and are shown to comprise expected trends when compared to published literature. This is followed by a discussion in § 5 which focuses on the difficulties associated with studying cumulative nonlinear propagation in a laboratory–scale (range–restricted) environment. A unique scaling model is proposed that allows one to predict useful indicators of cumulative nonlinearities and the relationship between laboratory– and full–scale experiments. It is inferred from this model that significant cumulative nonlinear distortion is most likely absent in our far–field data set. Proof of this is shown in § 6 using two correlation studies, waveform analysis (by means of a numerical hybrid-time frequency prediction code, see § 2.2) and application of the Morfey-Howell indicator at several points along the propagation path. Finally, in § 6.2.2, the locally distorted waveform is analyzed by means of *time-averaged* (statistical) metrics and it is concluded that shock-type waveform structures are solely present in the Mach cone and that the signatures are most intense at the Mach angle, where Mach wave radiation dominates.

3. Experimental arrangement

3.1. *Facility*

Experiments were performed in a fully anechoic chamber and open jet wind tunnel located at the J.J. Pickle Research Campus of The University of Texas at Austin. A plan view of this facility is shown in figure 3. Interior dimensions of the anechoic chamber (wedge tip to wedge tip) are 19 ft(L) × 15 ft(W) × 12 ft(H). The acoustic wedge design comprises 18 in of fire retardant melamine foam backed by a 4 in air cavity followed by 5.5 in of recycled cotton fibre. This level of treatment provides 99% normal incidence sound absorption for frequencies above 100 Hz, based on impedance tube tests performed at ETS Lindgren (Cedar Park, Texas). As for the wind tunnel, entrained air is allowed to enter the chamber through a 4 ft × 4 ft opening behind the nozzle jet rig which then exhausts through a 6 ft × 6 ft acoustically treated eductor on the opposing wall. A set of turning vanes redirect the exhausted flow through an acoustically treated square duct before being drawn out by a 500 HP vane axial fan. The vane axial fan prevents flow recirculations from forming inside the chamber while the turning vanes prevent fan and other outside contaminating sources of noise from entering the chamber.

A custom fabricated jet rig allows different nozzle configurations to be tested and is installed along the centreline of the wind tunnel and chamber, as is shown in figures 3 and 4(a,b). Pressurized air is supplied to this jet rig by a 2,700 p.s.i.g. compressor attached to 140 ft^3 (4.25 m^3) of water volume storage that discharges through 4 in carbon steel piping capable of transporting dry air at 2,100 p.s.i.g. On top of the jet rig, the 4 in pipe line diverges into a 6 in inner diameter settling chamber. This settling chamber is located immediately upstream of the nozzle mounting flange and houses a Corning Celcor®, ceramic flow straightener (400 square cells per in^2 substrate) that conditions the flow before entering the nozzle contraction.

Nozzle pressure ratios (NPR) are regulated using a 3 in pneumatically actuated control valve governed by a control algorithm; this uses a National Instruments (NI) CompactRIO system. Test conditions are monitored and recorded using this Compact RIO system during each run. These include barometric chamber pressure (p_∞), temperature (T_∞) and humidity, total pressure (p_0) and temperature (T_0) in the plenum, as well as storage tank pressure.

8   W. J. Baars, C. E. Tinney and M. S. Wochner
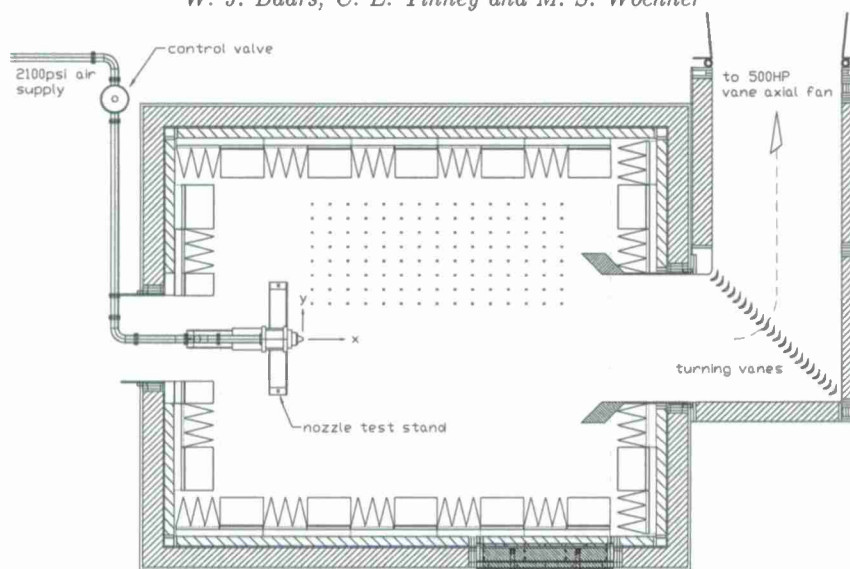
FIGURE 3. Plan view of the multidisciplinary fluid dynamics facility at UT Austin with the nozzle test rig installed. The microphone locations (projected on the (x, y)-plane) during the grid measurements are indicated by the dark circles.

(a)   (b)
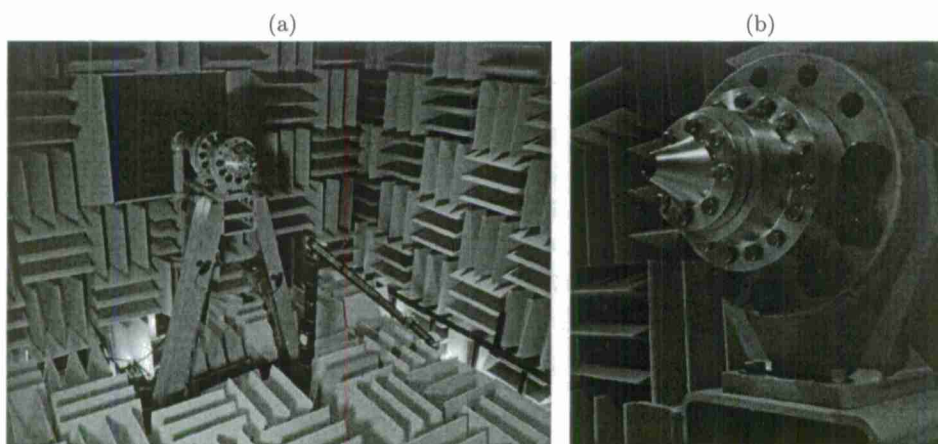
FIGURE 4. (a) Arrangement of the chamber during grid measurements of the far-field acoustics. (b) The Mach 3 MOC nozzle, with contraction, mounted to the ø6 in settling chamber.

The test article used for this study was designed using the Method of Characteristics to have an exit gas dynamic Mach number of $M_e = 3.00$ (total temperature, $T_0 = 273.15$ K, ratio of specific heats, $\gamma = 1.4$, specific gas constant of air, $R = 287.05$ J/kg/K). The exit diameter was constrained to 1 in (25.4 mm) resulting in a throat to exit length of 2.30 in. All measurements were performed with the nozzle operating under perfectly expanded conditions; a nozzle pressure ratio of $NPR = p_0/p_\infty = 36.73$ was required to achieve this shock-free flow. The associated mass flow was computed to be 1.04 kg/s.

Nonlinear distortion of acoustic waveforms from high-speed jets 9

(a)

Grid measurements: (in $\varphi = -38.5°$ plane)
$x/Dj = [5, 145], \Delta x/Dj = 10$
$r/Dj = [25, 95], \Delta r/Dj = 10$

(b)

Line-array measurements:

(plane: $\varphi = -38.5°$)
$4, \rho = 140D_j$
$3, \rho = 120D_j$
$2, \rho = 90D_j$
$1, \rho = 60D_j$
$\phi = 45°$
$20D_j$
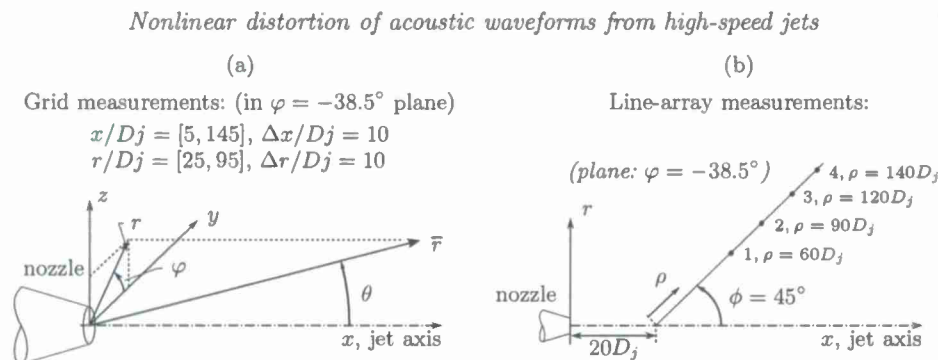
FIGURE 5. (a) Jet coordinate system and positioning of the 2D microphone grid relative to the nozzle exit plane. (b) Coordinate system and positioning of the four-microphone line-array radiating from $x = 20D_j$.

The convergent-divergent nozzle piece was attached to an additional contraction (6 in to 2 in diameter) which was mounted to the settling chamber as is shown in figure 4*(b)*.

3.2. *Instrumentation*

Acoustic data was acquired using four 1/4 in prepolarized, pressure-field, condenser microphones (PCB, model 377B10 and matching preamplifiers model 426B03). The microphones have a frequency response range of 4 Hz to 70 kHz with $\pm$ 1 dB error up to 20 kHz and a dynamic range of up to 170 dB (re 20 μPa). A NI-PXI-1042Q system (low 43 dBA acoustic emission) embedded with an eight channel NI PXI-4472 module provided the necessary IEPE conditioned power (27 VDC and 4 mA) to operate the microphones all the while conditioning the input signal to eliminate aliasing prior to digitization (filter roll-off occurs at 0.84 of the Nyquist frequency). All four channels were acquired synchronously at a rate of 102.4 kS/s with 24 bit resolution for a minimum of 2^{20} samples. Microphone diaphragms were oriented at grazing incidence to the acoustic wave fronts at all times (plane of the diaphragm intersecting the complete jet axis; see Viswanathan 2006) and with grid caps removed. Two different microphone configurations were used: a 2D grid in the jet center plane (identified by dark circles in figure 3) and, a line–array positioned strategically along the Mach cone half angle radiating from the post potential core region at $x = 20D_j$. Coordinates for the 2D grid and line–array are provided in figures 5*(a)* and 5*(b)*, respectively.

3.2.1. *Planar grid measurements.*

The planar 2D grid measurements were acquired on a (x,r)-plane oriented at an angle of $\varphi = -38.5°$. This uniform grid spanned from 5 D_j to 145 D_j in the axial direction and from 25 D_j to 95 D_j in the radial direction with a spacing of $\Delta x = \Delta r = 10$ D_j. The furthest microphone position was located at $|\bar{r}| = 173.3$ D_j and $\theta = 33.2°$. A translatable array was constructed that supported the four microphones and was re-positioned in between runs to capture the acoustic data at all grid positions (figure 4*a*).

In order to facilitate subsequent discussion, several grid points were selected in order to form both line and arc arrays of acoustic observers. Figure 6 provides a visual mapping of these observer points. The first of these comprised eight microphones forming an 'artificial' arc-array at $\rho = 100$ $D_j \pm 1.5\%$ and centered at $x = 20D_j$. The precise location of these eight acoustic observers are listed in table 1 and are further denoted by microphones 1 to 8. Several lines radiating from $x = 20D_j$ were then formed, labeled A–G in figure 6. Subsequent discussions employ subscripts (increasing with out-

10   *W. J. Baars, C. E. Tinney and M. S. Wochner*

mic #	1	2	3	4	5	6	7	8
$(x,r)/D_j$	(115,25)	(115,35)	(105,55)	(95,65)	(85,75)	(75,85)	(55,95)	(45,95)
$\phi\ [degr]$	14.7	20.2	32.9	40.9	49.1	57.1	69.8	75.3
ρ/D_j	98.2	101.2	101.2	99.3	99.3	101.2	101.2	98.3

TABLE 1. Locations of microphones (8) used to form an artificial arc-array centered at $x = 20D_j$.
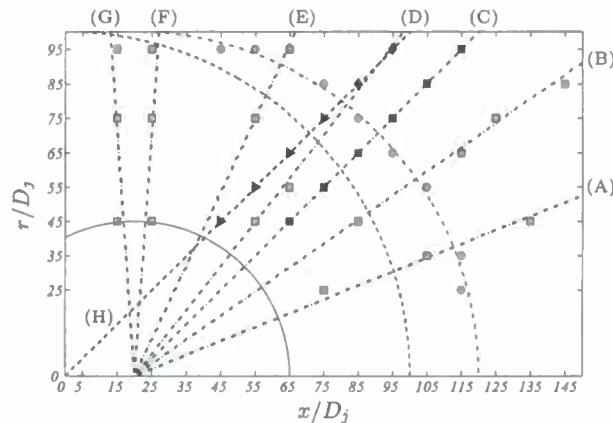
FIGURE 6. Microphone observer positions used to construct various line arrays labeled A-H. Lines A-G ($\square$) radiate from a point at $x/D_j=20$; line H ($\triangle$) radiates from the nozzle exit plane. An 'artificial' arc-array ($\circ$) at $\rho = 100$ $D_j \pm 1.5\%$ is centered on $x = 20D_j$.

ward radial distance) to indicate which microphone is being used. For example, microphone C_4 is located at $(x, r) = (95, 75)$ D_j. Furthermore, lines A–G are angled at $\phi = [22, 35, 45, 52, 65, 86, 94]°$, respectively. A final line, H, highlighted in figure 6, originates from the nozzle exit plane.

3.2.2. *Line-array measurements.*

After processing the 2D planar grid measurements, the sound propagation path was found to emanate from the post-potential core region near $x = 20$ D_j, and along a path oriented at 45° from the jet axis. A line-array of four microphones was then installed and positioned so as to follow this path. As can be seen from the coordinates that are provided in figure 5(b), all four microphones were positioned at one azimuthal angle φ, as opposed to the work of Petitjean & McLaughlin (2003) for example. This in-line placement is necessary in order to perform coherence studies and waveform analyses (§ 6.1 & § 6.3) along this path. It is believed that the sound propagation is not obstructed by upstream microphones due to the 1/4 in tube supports.

3.3. *Test Conditions*

Experiments were conducted over a duration of three days during late Autumn time conditions in Austin, Texas. Weather patterns produced high levels of relative humidity (RH) for the first (75%, see figure 7) and second (63%) days of testing which eventually dropped to 48% by the third day. These conditions were monitored periodically throughout the duration of the experiments and are summarized in table 2 using subscripts $j, \infty, 0$ to denote jet–exit, ambient and stagnation conditions, respectively. Column 'grid–

Nonlinear distortion of acoustic waveforms from high-speed jets 11

FIGURE 7. The Mach 3 jet plume being visualized by water vapor during a run with 75% relative humidity.

array *(day 1)'* corresponds to the measurements performed in the range $x = [5, 95]$ D$_j$, $r = [25, 95]$ D$_j$, whereas column 'grid–array *(day 2)'* pertains to the remaining section of the grid: $x = [105, 145]$ D$_j$, $r = [25, 95]$ D$_j$. Jet exit conditions were calculated from standard isentropic relations using an estimate for the dynamic viscosity based on Sutherland's law,

$$\frac{\mu_j}{\mu_{ref}} = \left(\frac{T_j}{T_{ref}}\right)^{3/2} \frac{T_{ref} + s}{T_j + s}, \tag{3.1}$$

where $\mu_{ref} = 1.716 \cdot 10^{-5}$ Ns/m^2, $T_{ref} = 273$ K and $s = 111$ K for air. Other relevant non-dimensional parameters are provided in table 2.

A useful metric for predicting the formation of Mach waves in a jet is known as the Oertel convective Mach number, denoted M_{co}. This non-dimensional parameter is determined from $M_{co} = (U_j + 0.5a_j)/(a_j + a_\infty)$. If $M_{co} < 0.75$ then Mach waves are non-existent, for $0.75 < M_{co} < 1$ the Mach waves are in their developing stages, and for $M_{co} > 1$, Mach waves are expected to be fully developed. Upon inserting the conditions from table 2 into this expression we obtain a value of $M_{co} = 1.31$, which suggests that these conditions are more than adequate for generating strong Mach waves.

3.3.1. *Convective velocity.*

The convective speed of the prominent hydrodynamic instability waves are a prerequisite for calculating the Mach wave radiation angle. Here we have chosen to assume $U_c = 0.80 \, U_j$ and was motivated by the findings of McLaughlin *et al.* (1975) and Troutt & McLaughlin (1982) who showed phase velocities of the axial instability waves to be of this magnitude over a broad range of wave numbers; similar findings were reported by Kerhervé *et al.* (2006). Norum & Seiner (1982) on the other hand, achieved reasonable results using $0.7 \, U_j$. A recent study by Tinney *et al.* (2008), based on near-field pressure and velocity correlations, has also shown how low-mode number disturbances, residing on the high speed sides of the annular shear layer, convect at speeds near $0.8 \, U_j$. These low mode-number events correlate well with the far-field pressure (Hall *et al.* 2009).

4. Basic acoustic–field observations

4.1. *Statistics*

The spatial topography of the overall sound pressure level (OASPL) obtained from the planar grid measurements is presented in figure 8. Experimentally acquired contours can also be found in the literature (Potter & Crocker 1966; McLaughlin *et al.* 1975; Gallagher 1982; Varnier 2001; Greska *et al.* 2008), but none with the range provided here (up to $x = 145$ D$_j$ and $r = 95$ D$_j$). The classical heart shape pattern and cone of silence are observed. A strong intensity gradient centred along $\theta = 45°$ (initiating from the jet exit) is also observed and supports the notion that Mach wave radiation intensity decays rapidly beyond the Mach wave radiation angle. Furthermore, the 'edge' remains distinct with outward distance, up to, and likely beyond the range of consideration.

12   W. J. Baars, C. E. Tinney and M. S. Wochner

		grid-array *(day 1)*	grid-array *(day 2)*	line-array *(day 3)*
	M_j		$3.00 \pm 1\%$	
	$NPR = p_0/p_\infty$		$36.73 \pm 4.5\%$	
measured	p_∞ $[kPa]$	100.7	100.8	101.2
	T_0 $[K]$	291.2	286.2	285.1
	T_∞ $[K]$	293.3	287.2	287.5
	RH $[\%]$	75.4	63.2	48.2
calculated	T_j $[K]$	104.0	102.2	101.8
	a_j $[m/s]$	204.4	202.7	202.3
	a_∞ $[m/s]$	343.3	339.7	339.9
	U_j $[m/s]$	613.3	608.0	606.9
	$f_c = U_j/D_j$ $[kHz]$	24.1	23.9	23.9
	T_j/T_∞	0.35	0.36	0.35
	ρ_∞/ρ_j	0.35	0.36	0.35
	Re_j	$7.4 \cdot 10^6$	$7.6 \cdot 10^6$	$7.6 \cdot 10^6$
	$U_c = 0.80 U_j$ $[m/s]$	490.6	486.4	485.5
	$M_a = U_j/a_\infty$	1.79	1.79	1.79
	$M_c = U_c/a_\infty$	1.43	1.43	1.43
	ϕ $[degr]$	45.6	45.7	45.6

TABLE 2. Summary of the experimental conditions (measured) for the microphone grid-array and line-array measurements (M_j was controlled to be the fully expanded Mach number $M_e = 3.00$). Computed jet parameters are indicated in the 'calculated' section.
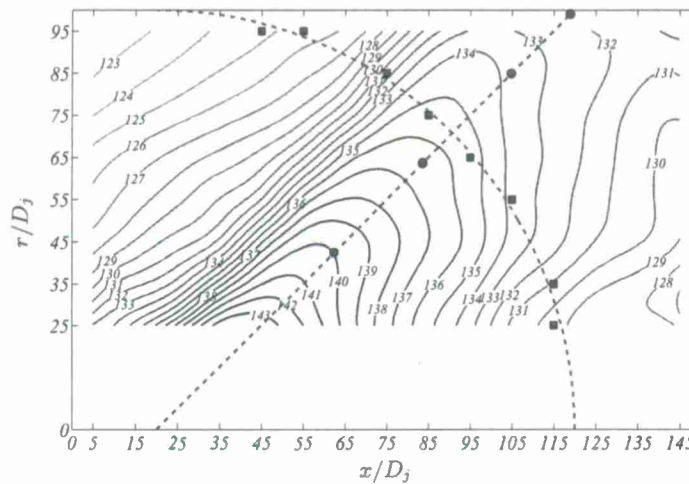
FIGURE 8. Contours of constant Overall Sound Pressure Level (OASPL) in dB, $p_{ref} = 20$ μPa. Contour lines of the original grid are interpolated (spline) by a factor of 10; original grid has uniform spacing of 10 D_j. Superposed are the grid points used to construct the artificial arc-array, and the line-array measurement locations are indicated.

These observations, in combination with the suggestion that the direction of peak sound intensity coincides with the radiation angle (Tam *et al.* 1992), justifies the assumption for the convective speed of the instability waves responsible for generating Mach waves: $U_c = 0.80 U_j$ (see § 3.3).

Nonlinear distortion of acoustic waveforms from high-speed jets   13

FIGURE 9. The OASPL as function of the jet axial coordinate for all radial positions. The solid gray circles indicate a simple linear spreading model that initiates at the position of maximum OASPL. Each circle is located at the subsequent r/D_j position and the orientation of this model is $\phi = 45°$.

OASPLs are presented in figure 9 as function of the jet axial coordinate for all radial positions. A simple linear spreading of the OASPL, superposed all other trends, is shown as a dashed line with solid markers. The spreading originates from the estimated point of maximum OASPL ($x/D_j = 40$, $r/D_j = 25$, $OASPL = 144$ dB) and has an orientation of $\phi = 45°$. By comparing the solid markers (r/D_j grid locations) to their corresponding experimental OASPL curves at that r/D_j location it can be concluded that the actual spreading rate along the peak OASPL path is nearly linear. A subtle deviation is expected due to contributions from axially distributed noise sources residing in the pre– and post–sound intensity regions of the flow that contribute acoustic energy to the peak propagation path regions of the far field. Nonetheless, the close resemblance of a $1/r^2$ decay law along the peak OASPL path justifies two important assumptions that are required of subsequent analysis. The first is that measurements along the peak OASPL path can be considered to have been taken in the acoustic 'far–field' regions of the jet flow while the second is the peak OASPL path is the propagation path for the dominant sources in the flow.

4.1.1. *Core lengths of the jet*

It is known that the most intense sound producing region of a jet flow occurs in the post-potential core. No centreline data is available for the current study, and so, empirical formulations are used to determine the potential core length ($L_c = x_c/D_j$) and the length of the supersonic region ($L_s = x_s/D_j$). Nagamatsu & Horvay (1970) showed that $L_c = 5.22M_j^{0.90} + 0.22$ and $L_s = 5M_j^{1.8} + 0.8$ worked well for a broad set of conditions; the jets were mostly operated in near-perfectly expanded conditions and encompassed unheated and high temperature jets with exit diameters ranging between 1 in and over 40 in. Upon applying these empirical relations to the current set of data, we obtain $L_c = 14.3$ and $L_s = 36.9$. It was further shown (Nagamatsu & Horvay 1970) that the location of most intense sound generation ($L_p = x_p/D_j$) resided just upstream of the sonic point in the so-called transition region, but always downstream of the potential core; $L_c < L_p < L_s$. These observations were based on measurements of the pressure fluctuations and acoustic power output along the axis of the jet. Varnier (2001) later extended the empirical model of Nagamatsu & Horvay (1970) and concluded that the estimate of Nagamatsu & Horvay (1970) for L_s was adequate in describing the most pronounced sound source location. However, Varnier (2001) found that for a slightly

W. J. Baars, C. E. Tinney and M. S. Wochner

model	L_c	L_p	L_s
Nagamatsu & Horvay (1970)	14.3	–	36.9
Varnier (2001)	13.7	14.5	36.9
Greska *et al.* (2008)	17.1	–	–
Witze (1974)	18.3	–	–
current experimental data	–	17.5	–

TABLE 3. Potential core length, location of most intense noise production, and length of the supersonic region for the Mach 3.0 jet according to various models.

overexpanded jet, $M_j = 2.8$ ($M_e = 3.3$; M_e being the design Mach number), L_p resided further upstream at $L_s/L_p \approx M_j^\alpha$ with $\alpha = 0.85$, and that the potential core length was estimated by $L_s/L_c \approx M_e^{0.9}$. For the current study, this results in estimates of $L_p = 14.5$ and $L_c = 13.7$.

Surprisingly, the jet temperature does not appear explicitly in the previous formulations. Thus, discrepancies are expected when large variations in jet exit conditions are analysed. In an effort to overcome this deficiency, Greska *et al.* (2008) suggested that $L_c = 3.134\exp(1.043M_j - M_c)$; variations in jet temperature were now accounted for by way of a convective Mach number. Once again, for the current study of an unheated jet, this results in $L_c = 17.1$. Lastly, we consider the model proposed by Witze (1974), which governs only supersonic unheated jets, and from which we estimate the potential core length in the current study to be $L_c = 18.3$. This last model was described in more detail by Baars *et al.* (2011), including a discussion of the adaptations of the Witze (1974) model by other authors attempting to account for supersonic heated jets. A recent large-eddy simulation of a slightly overexpanded and slightly heated ($T_j = 360$ K) Mach 3.30 jet by de Cacqueray *et al.* (2011a) found $L_c = 10$ (based on locating the point where U = 0.90 U$_j$), $L_p = 12.5$ and $L_s = 18$. These numbers fall short of the empirical models previously mentioned and may be attributed to both the elevated temperature used in the simulation (this is known to reduce L_c; see Baars *et al.* 2011) and, the first set of overexpansion shocks (causing the flow to deflect towards the jet axis and further shortening the core length).

A summery of the results obtained from these aforementioned models is provided in table 3. An estimate for the location of maximum peak pressure fluctuations, obtained by way of linear extrapolation of the peak OASPL, has also been included for comparison. Visual inspection of figure 8 suggests that $L_p = 17.5D_j$ is reasonable and will be used throughout the remainder of the analysis.

4.2. *Spectral Distribution of Sound*

Estimates of the one-sided Power Spectral Densities (PSD's) from points located on the artificial arc-array (table 1) are presented in figure 10 using a frequency resolution of $\delta f = 12.2$ Hz ($\Delta St_{D_j} = 5.1 \cdot 10^{-4}$) and $N = 8,192$ samples per bin. Low frequency wiggles ($St_{D_j} < 0.03$) are attributed to reflections from the chamber walls based on the first fundamental frequencies identified in the spectra and the distance from each observer position to the chamber wall.

Additional spectra are presented in figure 11 and are computed by first scaling each point to $\rho = 100$ D$_j$ and then averaging points that share the same azimuthal position for a given spreading line (A to G). The scaling involves a simple linear spreading concept and does not include corrections for humidity. An illustration of this process is shown in figure 12*(a)* for microphone observers located along line C and are shown to overlay

Nonlinear distortion of acoustic waveforms from high-speed jets   15
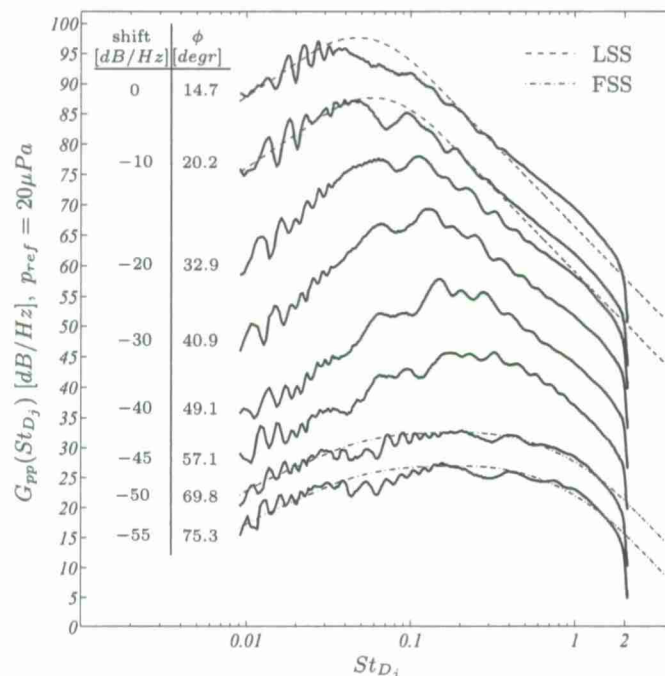
FIGURE 10. Pressure spectra along the artificial arc-array (5% bandwidth moving filter applied). Spectra at shallow and side-line angles are compared to LSS and FSS trends, respectively (Tam *et al.* 1996).

one another quite well. Wiggles found in the spectra at $\rho = 140D_j$ are observed and are believed to be caused by changes in the flow resistive properties of the melamine foam (that the acoustic wedges are constructed from) due to rather high relative humidity levels in the chamber $(63\% - 75\%)$ during the first two days of testing. Proof of this is shown in figure 12*(b)* by comparing the pressure spectra at two microphone locations and under different relative humidities; the general features are unaffected.

Nevertheless, the spectra in figures 10, 11 and 12*(a,b)* display two well-accepted trends that are typical of supersonic jet noise. That is, a pronounced hydrodynamic–like ridge at shallow angles $(\phi \leqslant 49.1°)$, –indicative of the noise produced by Mach wave radiation– and broadband, lower amplitude, spectra at sideline angles $(\phi \geqslant 57.1°)$ –typical of the fine–scale turbulence mixing noise. Large Scale Similarity (LSS) and Fine Scale Similarity (FSS) spectra (Tam *et al.* 1996, 2008) have been included and demonstrate good agreement for the shallow and sideline angle observers, respectively.

Contours of sound pressure intensity at various Strouhal numbers are illustrated in figure 13*(a-f)* to show the spatial topography of the pressure spectra. This is obtained by applying a band-pass filter that averages over 20% of the chosen center frequency in order to remove the wiggles caused by humidity effects discussed earlier. For reference, the PSD's are presented in contour format in figure 14 as function of axial distance for three different radial positions. Figures 13*(a)* and 13*(b)* reveal peak intensities of the low frequencies radiating at angles shallower than the Mach wave radiation angle with lines

16   W. J. Baars, C. E. Tinney and M. S. Wochner
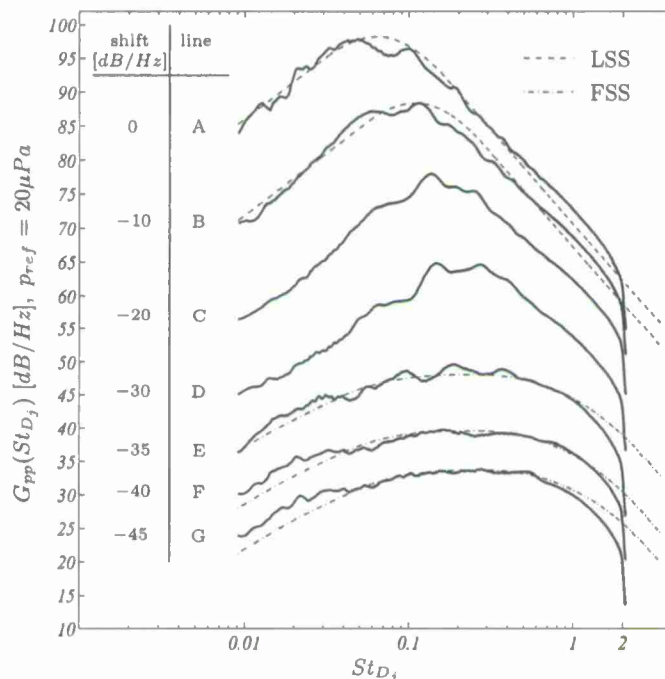
FIGURE 11. Pressure spectra along spreading lines A to G (5% bandwidth moving filter applied). The spectra are averaged from the individual microphones along the radial lines after they were linearly scaled to $\rho = 100\,D_j$. Spectra at shallow and side-line angles are compared to respectively the LSS and FSS spectra presented by Tam *et al.* (1996).
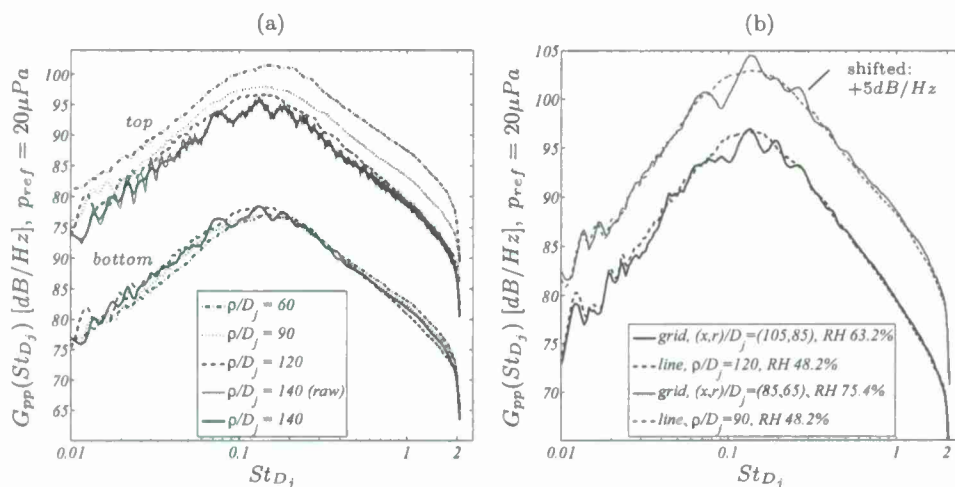
FIGURE 12. (a) PSD's along the line-array (5% bandwidth moving filter applied), *(top)* raw spectra, *(bottom)* spectra linearly scaled to $\rho = 100\,D_j$. (b) Effect of relative humidity on the pressure spectra at two microphone locations along the line array.

Nonlinear distortion of acoustic waveforms from high-speed jets   17

emanating from an origin located downstream of the post potential core ($x \gtrsim 17.5 D_j$). This is caused by a considerable drop in axial phase velocity of the instability waves for low frequencies ($St < 0.2$) (Troutt & McLaughlin 1982); shallow propagation of low frequency noise was observed in a similar fashion by Kuo *et al.* (2010). For frequencies centered around $St_{D_j} = 0.2$ in figure 13*(c)*, the peak radiation angle follows along the Mach wave radiation angle. Spectra that are filtered around higher center frequencies (figure 13*d-f*) appear to shift their origins upstream, but never originate from the nozzle exit plane. These findings are in agreement with Kuo *et al.* (2010) who observed that the angular orientation of the lobe of peak intensity remained mostly unchanged with frequency for an unheated Mach 1.5 jet. Contrary to the current result, Kuo *et al.* (2010) observed a broadening of the lobe at higher frequencies and concluded that this was more consistent with the notion that the noise pattern produced by the fine–scale turbulence was omni-directional. Here, a broadening is not explicitly observed. A plausible explanation for this discrepancy is the high convective Mach number in this study which causes the highly directional Mach wave radiation process to saturate more of the higher frequency omni-directional noise content. Henceforth, differences between acoustic source mechanisms and associated sound fields might express themselves better due to the high convective (1.43) and acoustic (1.79) Mach numbers being explored in this study when compared to other supersonic jet studies (where any typical trends might be embedded in the more conventional sound producing mechanisms). For example, most supersonic jet noise studies found in the open literature comprise acoustic Mach numbers around unity; this produces a subsonic convective Mach number. In general, these findings support the notion that high frequency noise radiates from regions close to the nozzle exit, while low frequency noise dominates locations further downstream. However, all radiating angles appear to originate from a region surrounding the post potential core of the jet.

Contours of the spectral peak amplitude and peak frequency are presented in figures 15*(a)* and 15*(a)*, respectively. The peak Strouhal number is constant along outward spherical sound propagation paths for angles equal or less than the Mach angle. The shallower the angle, the lower the peak frequency, which is expected from earlier discussions. Peak frequencies at side-line angles possessed a large plateau range thus making it difficult to precisely identify the most energetic frequency.

5. Acoustic nonlinearities from a laboratory–scale jet

5.1. *Addressing the difficulties*

Numerous endeavors have been undertaken to investigate the nonlinear propagation of sound from jet flows and in range-restricted environments. Some examples include the work of Gallagher (1982) and Petitjean *et al.* (2006). However, only weak observations of cumulative nonlinear effects have been made using a laboratory–scale setup, all the while being observed under full–scale conditions. Examples of full–scale jet and rocket tests can be found in the literature (Morfey & Howell 1981; McInerny 1996; McInerny & Ölçmen 2005; Gee *et al.* 2008; Saxena *et al.* 2009). In particular, significant nonlinear effects from full-scale engine tests were found in the spectra presented by Morfey & Howell (1981) and Gee *et al.* (2008). The inconsistency is caused by the lack of rigor in understanding what the appropriate scaling parameters should be for producing measurable cumulative nonlinearities in a laboratory–scale environment. In this chapter, an effort is made to introduce a scaling model that could be used to guide future studies aimed at predicting whether the acoustic waveform produced by a jet flow will undergo cumulative nonlinear waveform distortion.

18   W. J. Baars, C. E. Tinney and M. S. Wochner
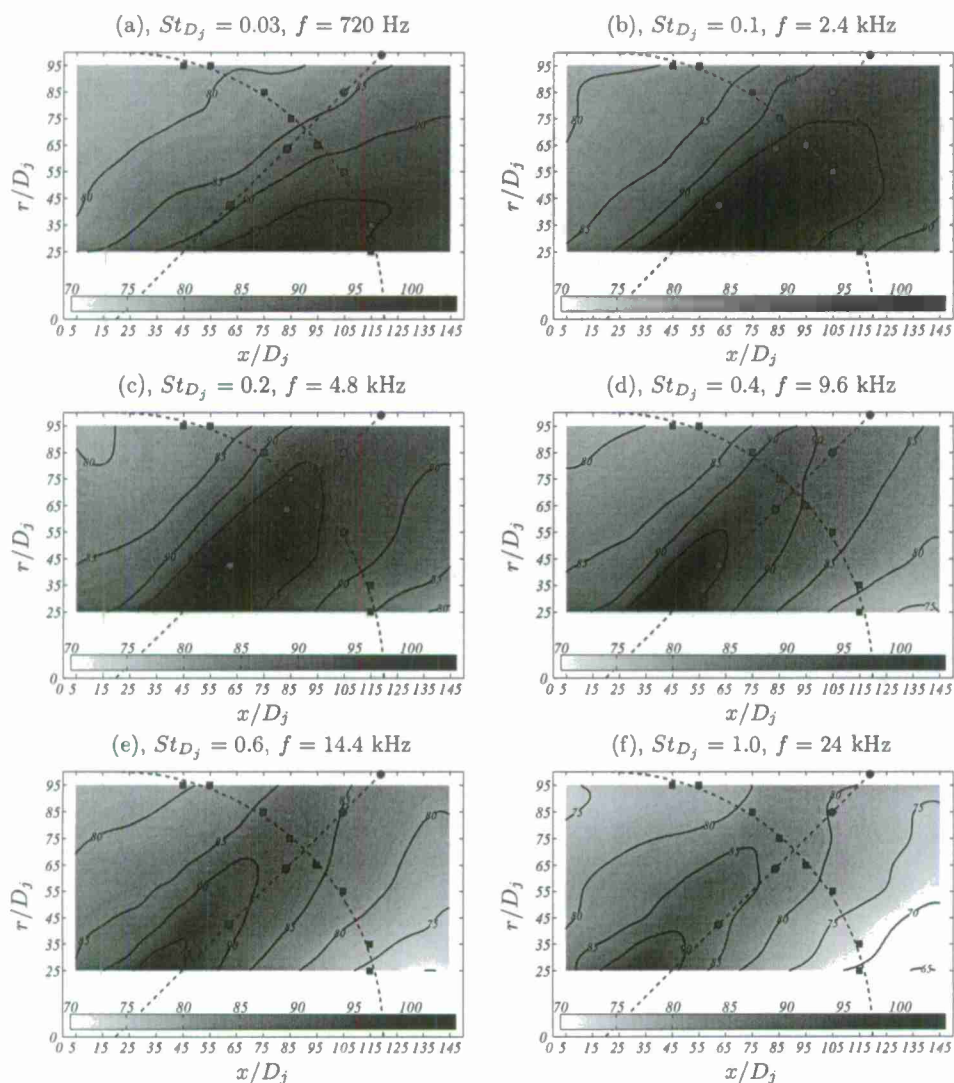
FIGURE 13. Contours of the Sound Pressure Level (SPL) in dB/Hz, $p_{ref} = 20$ μPa. The SPL value is averaged over a domain spanning $\pm 20\%$ around the center Strouhal number.

Complete dynamic similarity is required of every laboratory–scale study and is achieved by matching both sub–scale and full–scale similarity parameters. For high-speed jet flows, this comprises the Reynolds number, Mach number and jet temperature ratio. Geometric scaling is another prerequisite which is typically represented by the observer distance *relative* to the jet exit (or source region) using a normalization based on D_j. The latter, however, turns out to be a flawed scaling approach for producing measurable cumulative nonlinear effects in a range-restricted environment if the sound field medium is the same for both the laboratory– and full–scale experiment; shock formation distances and absorption losses do not scale with nozzle geometry, but rather with properties of the source. In fact, an *absolute* observer distance might be more appropriate since nonlinear

Nonlinear distortion of acoustic waveforms from high-speed jets   19

FIGURE 14. Equal spectral density contours of the one-sided PSD for (a) $r/D_j = 25$, (b) $r/D_j = 55$ and (c) $r/D_j = 95$ (5% bandwidth moving filter applied).

FIGURE 15. (a) Contour of the peak SPL in dB/Hz, $p_{ref} = 20\ \mu$Pa. (b) Contour of the peak Strouhal number in kHz.

propagation effects through the standard atmosphere are not scalable (these discrepancies have also been observed by Gallagher (1982), Petitjean *et al.* (2006), McLaughlin *et al.* (2010) and Saxena *et al.* (2009)). As an example, a successful capture of cumulative non-linear waveforms produced by a full-scale engine by Gee *et al.* (2008) comprised observer distances of 300 m (410 D$_j$); most laboratory–scale studies are restricted by chamber walls that extend only a few meters from the source region. While the use of geometrical scaling is the culprit of these failed laboratory-scaled studies, we will show in § 5.2 that measurable cumulative non-linear effects can be furnished using geometrically scaled nozzles and in a range-restricted environment, so long as all relevant jet parameters are taken into consideration.

5.2. *Scaling model for nonlinear supersonic jet noise*

An *ad hoc* approach to confront the issues surrounding nonlinear scaling is outlined here by presenting scaling laws based on reasonable assumptions. An earlier attempt to develop a scaling model was performed by Gee (2005) who addressed the effect of varying ambient conditions. In the current model we assume that the ambient medium

20   *W. J. Baars, C. E. Tinney and M. S. Wochner*

is identical, and thus, the models are complementary to one another in that sense. To the authors' knowledge, this is the first known development of such a complete model.

5.2.1. *Length-scales and the check for nonlinear dominance*

The most fundamental ingredients for ensuring waveform distortion by cumulative nonlinear effects are a high enough amplitude of the initial waveform (i.e. in terms of particle velocity or pressure) and favourable atmospheric absorption losses. On a theoretical basis, a first step in determining if nonlinear distortion will occur is to consider two important length-scales corresponding to viscous absorption and cumulative distortion effects. The first of these length scales is generally taken as the acoustic absorption length (l_a), which is the inverse of the classical absorption coefficient

$$l_a = \frac{1}{\alpha}. \tag{5.1}$$

Classical absorption coefficients for air are functions of frequency and depend on ambient conditions, i.e. temperature, pressure and relative humidity (RH). For our laboratory conditions, the curves for the absorption coefficient for different relative humidities are shown in figure 16*(a)* and are taken from Appendix B of Blackstock (2000). The coefficient has units of nepers per unit distance (Np/m, 'neper' is a unit without units) and can be converted to the decibel absorption rate $\overline{\alpha}$ in units of decibels per unit distance according to $\overline{\alpha}(f) = 8.686\alpha(f)$. Figure 16*(b)* presents the amplitude coefficient for a relative humidity of 70% (average humidity for our grid-array measurements) and indicates the various contributions from relaxation and thermoviscous absorption. Relaxation dominates at low frequencies and for atmospheric air, two relaxation processes are relevant: absorption associated with the vibration of nitrogen molecules (α_{N_2}) and absorption associated with the vibration of oxygen molecules (α_{O_2}). Thermoviscous effects (α_{tv}) become dominant at higher frequencies and is expressed by the asymptotic formula

$$\alpha_{tv} = \frac{\delta (2\pi f)^2}{2a_\infty^3}, \tag{5.2}$$

thus being a 'frequency-squared' effect acting on the entire frequency range. For completeness, δ is the diffusivity of sound and is equal to $3.66 \cdot 10^{-5}$ m^2/s. It is well known that relaxation frequencies of N_2 and O_2 are dependent on relative humidity (as shown in figure 16*a,b*) but do converge at high frequencies where thermoviscous effects are dominant.

The second length scale is concerned with cumulative nonlinear effects and is taken as the shock formation distance. For progressive (non-steepened) plane waves that are emitted by a broadband Gaussian source, the shock formation distance, as introduced by Gurbatov & Rudenko (p. 383, Hamilton & Blackstock 2008), is determined as,

$$\overline{x} = \frac{\rho_\infty a_\infty^3}{\beta(2\pi f_0)p_{rms}}. \tag{5.3}$$

In (5.3), the ambient density is taken as $\rho_\infty = 1.223$ kg/m^3, the coefficient of nonlinearity is given by $\beta = (\gamma+1)/2 = 1.2$, and p_{rms} is the pressure standard deviation of the source, and f_0 is the centre frequency of the broadband source. The shock formation distance can be interpreted as the distance along the propagation path that is required for the first shock (infinite derivative in the waveform) to occur and is based on lossless fluid theory, e.g. the distance at which cumulative waveform distortions are allowed to develop without losses imposed through viscous absorption. Because the sound field of a jet is

FIGURE 16. (a) Absorption curves for different relative humidities taken from Appendix B of Blackstock (2000). (b) The absorption curve for the laboratory conditions during the acquisition of the grid-array pressures.

three-dimensional in nature, it is replaced here by a simple spherical source emitting outgoing spherical waves. The shape of the source is irrelevant for the purposes of this analysis since only a single sound ray is being considered. As a consequence, the shock formation distance is denoted by $\bar{r}$ and is determined by (Hamilton & Blackstock 2008)

$$\bar{r} = r_0 \ exp\left(\pm\bar{x}/r_0\right), \tag{5.4}$$

where only the diverging waves (+ sign) are of importance in the current case. Shock formation distances are larger for spherically spreading sound waves than for plane waves due to the spreading losses in the former that cause a more rapid decay in the waveform amplitude with distance and hence, a delay in the steepening process. The parameter r_0 is the radius of the spherically radiating source and will be expressed in terms of the geometric nozzle size according to $r_0 = sD_j$.

This simple source is centred at the location of maximum peak pressure fluctuations on the jet axis ($x = 17.5D_j$, see § 4.1.1), and is reasonable. For the moment, the radius (r_0) is chosen to remain variable as this has considerable influence on the shock formation distance. The most interesting region concerning nonlinear noise propagation resides along the peak noise direction. Therefore, in the remainder of this analysis, only one spherically spreading ray will be considered which is oriented to follow a path along the direction of maximum OASPL (45° for the current laboratory case) and is assumed to be emitted by the simple spherical source. As a next step, the pressure standard deviation (p_{rms}) and centre frequency (f_0) at the source's surface are obtained by examining our

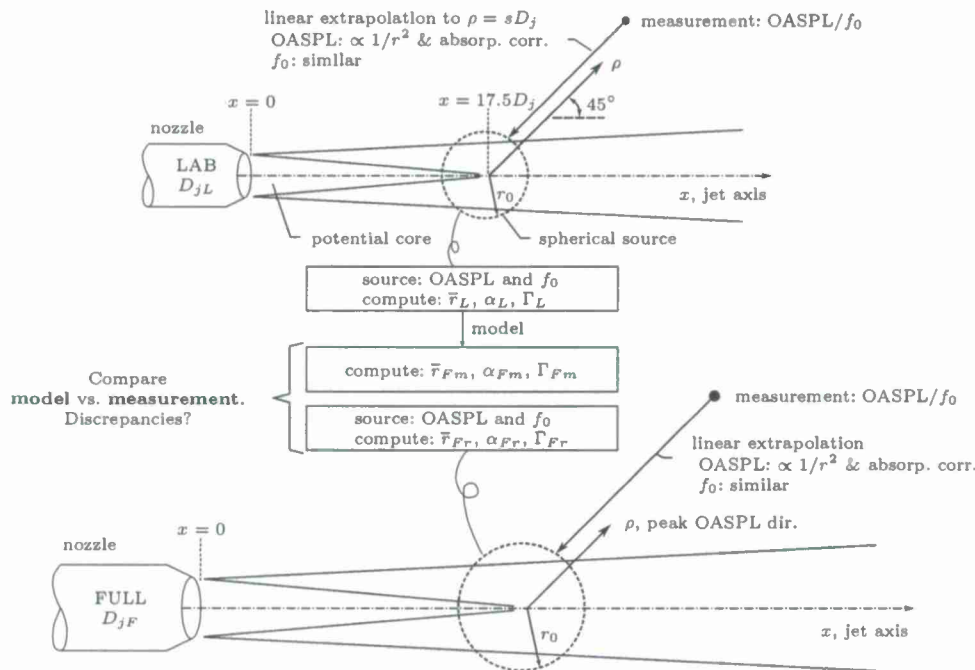22 *W. J. Baars, C. E. Tinney and M. S. Wochner*

FIGURE 17. Concept of scaling approach indicating the comparison of characteristic nonlinear parameters between the model prediction (subscript Fm, 'm' from model) and a full-scale measurement (subscript Fr, 'r' from reference).

measurements of the SPL presented in figure 12(a,b). The closest measurement along the peak noise direction ($\rho = 60$ D_j: OASPL $= 140.1$ dB and $f_0 = 3.6$ kHz) is extrapolated towards the source surface with corrections for atmospheric absorption being applied in the frequency domain; this assumes simple spherical spreading ($p \propto 1/r^2$). The source amplitude (p_{rms}) will thus be significantly higher than the measurement, and the centre frequency is assumed to be equal. An illustration of this process is shown in figure 17. Using the aforementioned approach and parameters, the shock formation distance ($\bar{r}_L$), as function of source size s, is presented in figure 18(a) where the subscript L refers to laboratory–scale conditions. The increasing trend is expected, since a larger source is affiliated with a lower source amplitude, which causes the waveform to steepen less fast and thus extends the shock formation distance. Lastly, for the given centre frequency, the amplitude coefficient is found to be $\alpha_L = 2.60 \cdot 10^{-3}$ Np/m (indicated in figure 16b) which corresponds to an absorption length of $l_{aL} \approx 385$ m.

Since expressions for both length-scales are established, a check for the presence of cumulative nonlinearities in our laboratory–scale experiment can be determined by calculating the Gol'dberg number. This dimensionless number is defined as the ratio of the acoustic absorption length (l_a) to the characteristic nonlinear length ($\bar{r}$); this is a measure of the strength of nonlinear distortion relative to that of dissipation (Hamilton & Blackstock 2008). If $\Gamma \leqslant 1$, attenuation dominates and the formation of shocks is suppressed. If $\Gamma \gg 1$, nonlinear effects will be distinctly present. Since a broadband source signal is considered in the current work, the absorption coefficient, shock formation distance, and thus Gol'dberg number are all functions of frequency. For simplification the centre frequency is selected for the analysis as was done in computing the shock formation distance

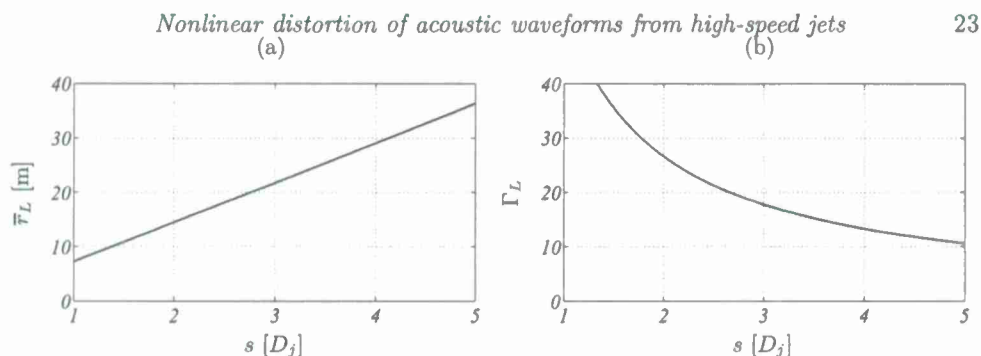*Nonlinear distortion of acoustic waveforms from high-speed jets* 23

FIGURE 18. (a) The spherical shock formation distance for the current laboratory scenario as function of source size ($r_0 = sD_j$). (b) The effective Gol'dberg number in the laboratory case as function of source size.

earlier, and is now denoted as the *effective* Gol'dberg number,

$$\Gamma = \frac{l_a}{\bar{r}} = \frac{1}{\alpha\bar{r}}. \tag{5.5}$$

It is reasonable for one to select the centre frequency of the measured SPL along the propagation path as the actual Gol'dberg number varies by less than one order of magnitude for a single frequency range around the centre frequency. The frequency dependence of the Gol'dberg number was recently addressed by Gee *et al.* (2012). The resultant effective Gol'dberg number for the current laboratory scale study of a Mach 3 jet flow (Γ_L) is shown in figure 18*(b)*. For the entire range of source sizes, $\Gamma_L \gg 1$, which implies that cumulative nonlinear effects are present. A typical source size is estimated to span the width of the shear layer in the post potential core regions of the flow. Given the relatively linear growth of the jet shear layer (Tinney *et al.* 2008), this results in a source size of $s = r_0/D_j = 2.5$, which we assume to hold over a range of jet conditions. The resultant shock formation distance and effective Gol'dberg number for this laboratory scale study are determined to be $\bar{r}_L(s = 2.5) = 18.1$ m and $\Gamma_L(s = 2.5) = 21.3$.

As for typical full–scale conditions, where higher temperature ratios and larger nozzle diameters are anticipated, the centre frequency, and thus α, decreases. It will soon be shown that under these conditions, $\bar{x}/r_0$ will decrease by a factor of about 5.5. Thus, the effective Gol'dberg number Γ will become even larger in the full–scale study thereby making cumulative nonlinear effects even more present in the matching full–scale case. It is important to point out that (5.4) assumes the source signal at $\rho = r_0$ to be Gaussian and without any features of a steepened waveform. We will show later that the waveform distribution from our nearest far–field observer point is well approximated by a Gaussian, but has 'N-wave' type structures even though it has not yet undergone any cumulative nonlinear distortion. Therefore, the shock formation distance and Gol'dberg number are expected to decrease and increase, respectively, which will differ slightly from what is predicted by this model. This warrants additional analysis to determine what effect a pre–steepened wave has on the shock formation distance.

5.2.2. *Scaling shock formation distance*

Having now shown that our unheated Mach 3.0 jet flow provides the necessary conditions for ensuring the formation of cumulative nonlinear acoustics ($\Gamma_L \gg 1$), scaling laws are derived for the occurrence of these effects between the laboratory– and full–scale environments in terms of jet exit parameters (i.e. D_j, M_j, T_j). We begin by scaling the shock formation distance, (5.3) and (5.4), based on lossless fluid theory. Lossless fluid

24   *W. J. Baars, C. E. Tinney and M. S. Wochner*

theory is the most favourable scenario for studying nonlinear effects, since the distance to shock formation is now the shortest possible ($\Gamma \to \infty$). In reality, absorption will delay, and partly suppress, this process. The physical meaning of this scaling will therefore be commented on later when the Gol'dberg number is scaled. Foremost, it is assumed that the propagation medium between the laboratory– and full–scale environments is the same (i.e. ambient air). On the other hand, it is not assumed in our formulations that the Strouhal number (St_{D_j}) corresponding to the peak SPL in the two environments is the same (variations in non-dimensional frequencies appear from changes in jet exit conditions, M_j and T_j). And so, peak frequencies are related by $f \propto St_{D_j} U_j / D_j$. Lastly, the sound intensity I for supersonic jets (satisfying the threshold $U_j > 1\,500$ ft/s) has been shown to vary with the cube of the jet exit velocity, thus $I \propto U_j^3$ (Ffowcs Williams 1963; Varnier 2001). Since the intensity is given by $I \equiv p_{rms}^2 / (\rho_\infty a_\infty)$, it can be shown that the source amplitude is $p_{rms} \propto U_j^{1.5}$. Note that the temperature ratio does not appear in this expression. In the case of subsonic and transonic jets, Viswanathan (2004) has provided subtle improvements to the relationship between sound intensity and jet exit velocity on account of variations in the temperature ratio (T_0 / T_∞). While we believe that temperature ratio does play a secondary role, its influence on the original findings from Ffowcs Williams (1963) is currently unavailable for supersonic jets. Upon inserting the aforementioned assumptions into (5.3), the following relationship unfolds,

$$\bar{x} \propto \frac{D_j}{U_j^{2.5} St_{D_j}}. \tag{5.6}$$

In the most general case for a supersonic jet, and by repeatedly taking into account the equal-medium assumption, (5.6) can be written as

$$\bar{x} \propto \frac{D_j}{M_j^{2.5} T_j^{1.25} St_{D_j}}. \tag{5.7}$$

Knowing that $r_0 = s D_j$, the exponent in (5.4) can be expressed as follows,

$$\frac{\bar{x}}{r_0} \propto \frac{1}{M_j^{2.5} T_j^{1.25} St_{D_j}}, \tag{5.8}$$

which employs all of the jet parameters of interest. The shock formation distance between the laboratory–scale (denoted by L) and full–scale (denoted by F) environments can be related as follows

$$\frac{\bar{r}_L}{r_{0L}} = \left(\frac{\bar{r}_F}{r_{0F}} \right)^\eta, \tag{5.9}$$

where the parameter η is obtained by substituting (5.8) into (5.4) and is defined as

$$\eta = \eta \left(M_j, T_j, St_{D_j} \right) = \frac{\bar{x}_L / r_{0L}}{\bar{x}_F / r_{0F}} = \left(\frac{M_{jF}}{M_{jL}} \right)^{2.5} \left(\frac{T_{jF}}{T_{jL}} \right)^{1.25} \left(\frac{St_{D_{jF}}}{St_{D_{jL}}} \right). \tag{5.10}$$

Because geometric scaling is observed throughout the open literature, one may to prefer to normalize the shock formation distance (5.9) by the nozzle exit diameter, which results in the following expression,

$$\frac{\bar{r}_L}{D_{jL}} = \left(\frac{\bar{r}_F}{D_{jF}} \right)^\eta s^{(1-\eta)}. \tag{5.11}$$

Here we show how (5.11), in combination with (5.10), constitutes a reasonable scaling relationship for the shock formation distance in terms of jet exit parameters.

Nonlinear distortion of acoustic waveforms from high-speed jets   25

In an effort to illustrate the scaling laws proposed here for regenerating cumulative nonlinear effects in a laboratory environment, we will first consider variations to η under different laboratory–scale conditions. This requires a full–scale reference case to be selected from the open literature; we will resort to a recent study by Gee *et al.* (2012). Their study comprised surveys of the far-field acoustics from a Pratt & Whitney F-135 engine installed in an F-35A military aircraft. The exit conditions of this study were approximated to be $M_{jF} = 1.4$ and $T_{jF} = 1000$ K (the engine was operated at military – 100% ETR – power) with a nozzle exit diameter of $D_{jF} = 0.95$ m (37.4 in). It was found that the foregoing assumptions of the jet operating conditions had little influence on the results. Gee *et al.* (2012) observed peak OASPLs of 138.8 dB at a radial location of $\rho = 80D_{jF}$ (centred 6.7 m aft of the aircraft) and at an angle of 50° from the jet axis. The centre frequency along the peak direction was found to be 300 Hz and tests were conducted with relative humidity levels of 24% ($\alpha_F = 1.48 \cdot 10^{-4}$ Np/m). This full-scale reference case is used throughout the remainder of this section. Given the full-scale conditions of Gee *et al.* (2012), the parameter η is determined from (5.10) and found to be 5.5 (see point 1 in figure 19). We will show later on how a reasonable prediction of the Gol'dberg number pertaining to the full-scale conditions can be determined from any laboratory–scale tests.

Variations in η are illustrated in figure 19 for a wide range of operating conditions ($1.0 < M_{jL} < 3.5$ and 50 K $< T_{jL} < 1200$ K). It is important to note that in this visual representation, Strouhal number remains constant at $St_{D_{jL}} = 0.15$ for the laboratory–scale case (based on our operating conditions) and at $St_{D_{jF}} = 0.32$ for the full–scale case. The correct mapping of $St_{D_{jL}} = St_{D_{jL}}(M_{jL}, T_{jL})$ is currently unknown. However, $St_{D_{jF}}/St_{D_{jL}} = 1$ if temperature and Mach numbers are matched (Greska *et al.* 2005), and so η should equal one under such conditions. And so, since the effect of Strouhal ratio on η is not accurately accounted for under varying jet conditions (differences in Mach number and temperature ratios between laboratory– and full–scale), figure 19 is, strictly speaking, only valid for point 1 from our current study. However, the order of magnitude is not expected to change significantly since Strouhal numbers for the laboratory– and full–scale cases are expected to be of the same order. As for the hatched area in figure 19, this corresponds to regions of the model that are invalid on account of $U_j < 460$ m/s (1500 ft/s); where the exit velocity threshold corresponds to a change in relationship between sound intensity and jet exit velocity (*i.e.* $I \propto U_j^3$ becomes invalid, see Ffowcs Williams (1963)).

In figure 19, the parameter η resides within roughly one order of magnitude (around unity) for a wide range of laboratory operating conditions. Furthermore, when the laboratory experiment encompasses an unheated and low Mach number jet, η becomes significantly large. This is the first indicator that studying cumulative nonlinearities in range–restricted environments is not necessarily feasible when the jet is operated under these conditions. Namely, if η becomes large, $\bar{r}_L/D_{jL}$ becomes extensively large (albeit the source size factor becomes much smaller than one). Shock formation (in an ideal lossless world) is thus expected to occur far outside any practical laboratory–scale anechoic environment. As a final testament to the usefulness of these scaling laws, it can be shown that when $\eta = 1$, it follows from (5.11) that the shock formation distance scales geometrically:

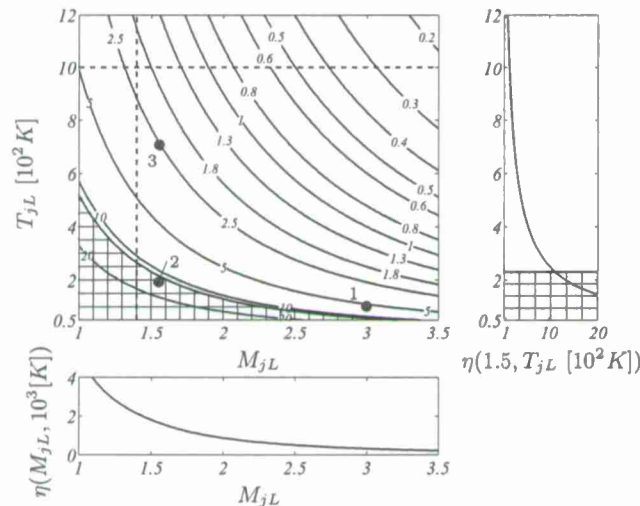$$\frac{\bar{r}_L}{D_{jL}} = \left(\frac{\bar{r}_F}{D_{jF}}\right). \tag{5.12}$$

26   W. J. Baars, C. E. Tinney and M. S. Wochner

FIGURE 19. *(main plot)* Parameter η for the scaling of the spherical shock formation distance for supersonic jets relative to a full-scale reference case ($M_{jF} = 1.4$, $T_{jF} = 10$ K). Conditions of the current study (point 1) along with the unheated (point 2) and heated (point 3) jet conditions from Baars *et al.* (2011) are indicated by the solid circles. *(right subset)* v for fixed $M_{jL} = 1.5$ –identified by vertical dashed line in main plot. *(bottom subset)* v for fixed $T_{jL} = 10^3$ K –identified by horizontal dashed line in main plot.

5.2.3. *Scaling effective Gol'dberg number*

Upon learning the effect of jet exit conditions on shock formation distance, it is natural for one to inquire about how these conditions can impact the effective Gol'dberg number. This ultimately determines to what capacity, and in what range, cumulative nonlinear waveform distortions become pronounced. A simplified illustration of the effect of Gol'dberg number on the degree of cumulative nonlinear distortion to the waveform emanating from the point of maximum OASPL is illustrated in figure 20. One may choose to consider these two trends representative of the amplitude of the second (or higher-order) harmonics in the case of a mono-frequency source. Or, with the current study in mind, figure 20 would illustrate increases in energy in the high-frequency bands of the SPL (relative to a base case) since steepened signals encompass more high-frequency energy. Nevertheless, an initial rise in the waveform's distortion due to cumulative nonlinear effects (waveform becomes more 'nonlinear') eventually plateaus and reaches its maximum value when viscous absorption becomes the dominant distortion mechanism. Viscous absorption continues to relax any further distortions and so the degree of nonlinearity eventually recedes asymptotically with propagation distance. When the effective Gol'dberg number is smaller (dashed curve relative to solid curve), wave steepening develops less rapidly.

Ideally, one would prefer to match this degree of cumulative nonlinearity versus ρ/D_j between the laboratory– and full–scale scenarios. This would ensure that the wave steepening process (and possible shock formation and coalescence) occurs at similar positions along the propagation path. Only then will an interpretation of sub-scale results be valid for the corresponding full–scale conditions. And so, it is in one's interest to hold (ΓD_j) constant, or at least, within the same order of magnitude (provided the assumptions in this model discussed earlier). Here we will explore whether cumulative nonlinear dis-
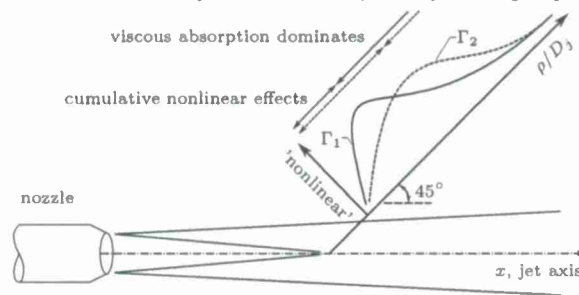
FIGURE 20. Illustration of the qualitative picture of nonlinearities along a spherical ray for two different effective Gol'dberg numbers: $\Gamma_1 > \Gamma_2$ (curves are not to scale).

tortions to the acoustic waveform produced in our laboratory–scale environment can be used to predict the same type of distorted waveform observed in full-scale tests, or under what conditions might one be able to replicate the full-scale distorted waveform in a range-restricted environment.

The mathematical expressions for this are relatively straightforward. Beginning with (5.5) and (5.11), it can be shown that

$$\frac{1}{\alpha_L D_{jL} \Gamma_L} = \left(\frac{1}{\alpha_F D_{jF} \Gamma_F} \right)^{\eta} s^{(1-\eta)}, \tag{5.13}$$

which can be rewritten as

$$\Gamma_L D_{jL} = \frac{\alpha_F^{\eta}}{\alpha_L} \left(\Gamma_F D_{jF} \right)^{\eta} s^{(\eta-1)}. \tag{5.14}$$

It is preferred to express the ratio α_F^{η}/α_L in terms of jet parameters, which could be achieved by using an absorption coefficient comprising only thermoviscous effects; see (5.2). However, since vibrational states of the molecules form unique asymptotes that differ between laboratory– and full–scale scenarios (differences in peak Strouhal numbers may be large; see figure 16b), classical absorption alone is incapable of furnishing an accurate comparison between the two scenarios. Thus, in order to compute the parameter group (ΓD_j) for the full–scale case based on known laboratory–scale values (or vice versa), (5.14) is used directly. Note that when values are substituted into (5.14), exit diameters are required to be in meters, if absorption coefficients are determined in Np/m.

With this approach in mind, an attempt is made to predict the effective Gol'dberg number of the full–scale conditions, based on the model and our laboratory–scale conditions (denoted by the subscript 'Fm', see the schematic in figure 17), and is shown in figure 21. The model prediction (Γ_{Fm}) is dependent on the source size and full-scale Strouhal number corresponding to the peak frequency in the direction of maximum OASPL. Once again, since the effect of Mach number and Temperature ratio on the peak Strouhal number is unknown at this time, a range of possible solutions based on $St_{D_{jF}}/St_{D_{jL}}$ should be considered. However, choosing now to isolate a peak Strouhal number for the full–scale condition (based on the measurements of Gee *et al.* (2012)), the effect of source size on Γ_{Fr} can be determined, as is shown in figure 22(a) for the appropriate choice of $St_{D_{jF}}/St_{D_{jL}}$. Here, the Gol'dberg number for the full-scale condition, predicted from this model and based on laboratory–scale conditions, is approximately 46 times higher than the laboratory–scale value. On the contrary, if we choose to fix the source size ($s = 2.5$), the effect of Strouhal number on the Gol'dberg ratio can be determined, as is shown in
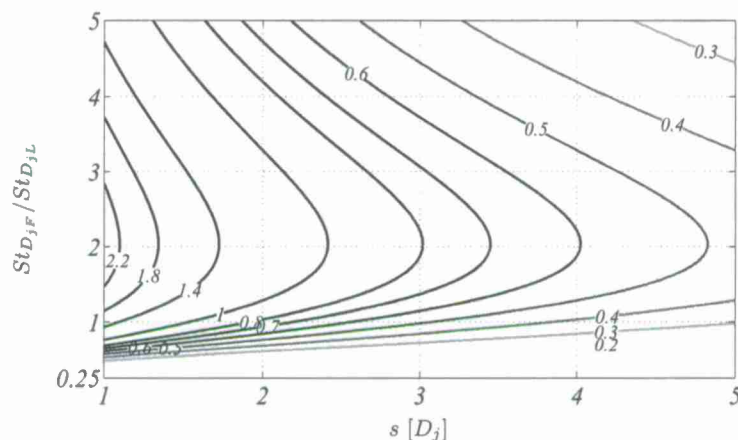
28   *W. J. Baars, C. E. Tinney and M. S. Wochner*

FIGURE 21. The effective Gol'dberg number for the full-scale case as predicted by the model, $\Gamma_{Fm}\left(s, St_{D_{jF}}\right)$, (multiply by 1 000).

figure 22*(b)*. The decay in Gold'berg number above $St_{D_{jF}}/St_{D_{jL}} = 2$ is a consequence of increased absorption at higher frequencies.

In an effort to determine the validity of this model approach, the effective Gol'dberg number is computed for the full–scale study of Gee *et al.* (2012), and compared to the prediction based on laboratory–scale conditions. The same approach for estimating nonlinear characteristic parameters is applied to the full-scale conditions whereby the OASPL at the source is obtained by extrapolating near-field observer levels to an imaginary source surface with corrections for atmospheric absorption. The resultant full-scale effective Gol'dberg number is shown in figure 22*(a)* and is only a factor of 2.1 times greater than the prediction tendered by the model. A summary of these numbers are shown in table 4 based on a typical source size of $s = 2.5$. We believe this to be a good result, but prefer to offer a number of plausible reasons for this discrepancy in the off-chance that one might choose to improve on this first principles approach.

Foremost, the dependence of source size s on exit Mach number and exit temperature ratio is unknown and may result in large differences between laboratory–scale and full–scale conditions. Furthermore, the high exit Mach number and low exit temperature ratio of our laboratory–scale condition places the exit velocity - sound intensity relationship in close proximity to the hatched regions of figure 19; the errors associated with this are not well understood with trends being derived from a limited number of experimental programs (Ffowcs Williams 1963). Nevertheless, insightful conclusions can be drawn here. Foremost, the parameter group (ΓD_j), being more than three orders of magnitude lower in the laboratory–scale case suggests that cumulative nonlinear distortions in the acoustic waveform will be more distinct under full-scale conditions, as opposed to measurements performed in a range-restricted environment. For instance, the increased peak frequency has a profound influence on the Gol'dberg number due to increased absorption. This further delays the shock formation distance which makes it more difficult for one to capture and study cumulative nonlinear distortions in a range restricted environment and so, any claims of such observations are clearly questionable. In closing, the cumulative nonlinear effects are expected to form in the waveforms emitted by this unheated, Mach 3 jet flow, but will not appear significant within the spatial confines of our anechoic chamber walls. Thus, no major wave steepening and coalescence are expected to be observed.
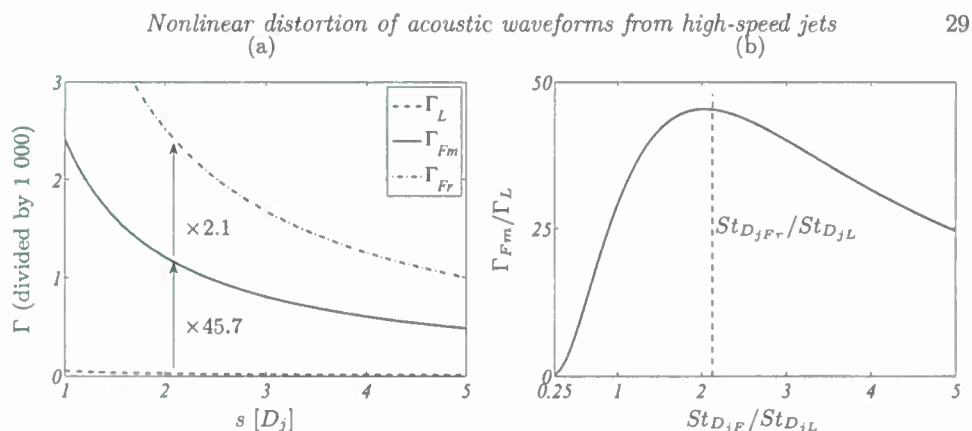
FIGURE 22. (a) The effective Gol'dberg number for the laboratory environment (Γ_L), the model prediction for the full-scale scenario (Γ_{Fm}) and the actual full-scale measurement (Γ_{Fr}). (b) The ratio of the predicted full-scale Gol'dberg number and the laboratory Gol'dberg number as function of Strouhal number ratio.

	l_a [m]	$\bar{x}$ [m]	$\bar{r}$ [m]	$\bar{r}/D_j$	Γ	ΓD_j [m]
Laboratory (measured)	385	0.36	18.1	713	21.3	0.541
Full–scale (model)	6,733	2.56	6.98	7.35	965	916
Full–scale (Gee *et al.* 2008)	6,733	0.82	3.35	3.53	2,010	1,910

TABLE 4. Summary of the nonlinear characteristic parameters in the laboratory case and full-scale cases (model and measurement) when the source size is fixed at $s = 2.5$.

Proof of this will be demonstrated in the next section by following the reasoning of Ffowcs Williams *et al.* (1975) and by application of the Morfey-Howell indicator (Morfey & Howell 1981).

6. On the absence of cumulative nonlinear acoustic distortion

It is known from our discussion in § 2 that nonlinear acoustical phenomena can be grouped into *cumulative* and *local* effects. Long-distance waveform distortions, encumbered by subsequent wave steepening, shock formation and shock coalescence, occur cumulatively along the noise propagation path. It is well known that these effects are ultimately dominated by viscous absorption and relaxation phenomena (Hamilton & Blackstock 2008), and so, the waveform relaxes to a shock-free state without showing direct evidence of past nonlinear effects†. Various statistical metrics are exercised in this section to quantify the degree of both *local* and *cumulative* nonlinear acoustic distortion of our measured waveforms. We begin with a simple correlation study in § 6.1 to complement the findings in figure 9, which establishes the sound propagation path for this jet flow. A description of the more mundane analysis tools is presented in § 6.2 and includes an analyses using the Morfey-Howell indicator. We then close with a waveform propagation study in § 6.3. Where geometric scaling is concerned, the current measurements are acquired at observer distances that exceed most laboratory–scale studies found in the open literature.

† Nonlinear effects are still present since the increased energy at high-frequencies undergo asymptotic decay with distance back to their expected linear value.

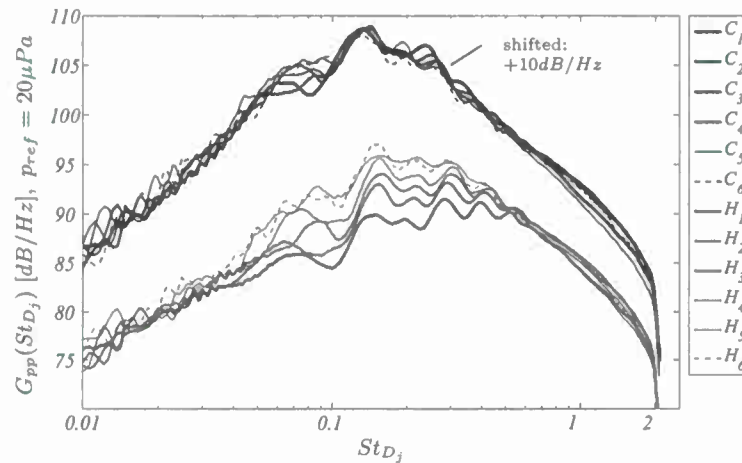30   *W. J. Baars, C. E. Tinney and M. S. Wochner*

FIGURE 23. PSD's of the microphones along line C and H after being linearly scaled to a distance of $100D_j$ (centered around $x = 0D_j$ for line H and $x = 20D_j$ for line C) (5% bandwidth moving filter applied).

6.1. *Spectral statistics along the propagation path*

The abundance of noise produced by this Mach 3 jet flow has been shown to propagate along spherically spreading lines that originate at $x = 17.5\ D_j$. Therefore, synchronized measurements along the line-array are considered since these measurements are acquired *along a propagation path* coinciding with the Mach wave radiation angle (oriented at $\phi = 45°$). Most studies found in the literature assume the jet noise to propagate along spherically spreading paths originating from the jet exit plane (Viswanathan 2008). This has lead many to inadvertently link changes in the far-field spectra (when corrected linearly to different far-field observer distance) to nonlinear effects. As an illustration, the spectra along lines C and D (see figure 6) are presented in figure 23 (all scaled using a simple linear spreading concept to $100\ D_j$ from the jet axis). While the spectra along line C collapse, it is clear that they do not along line H. This is simply because the noise does not propagate along line H, and so, different features of the far-field pressure waveform from various angles are observed instead of just one propagation angle. In fact, had line H been assumed to be the propagation path, incorrect conclusions regarding the shift in spectral energy as function of outward distance would have been made. This example shows the importance of having sufficient knowledge about the *spatial* dependence of the sound field, as opposed to single point measurements far from the jet, as is done in most anechoic chambers. Measurements that map the acoustic field are a prerequisite to developing well-supported conclusions on the sound propagation characteristics. From the spectra along the line-array (figure 12a) it becomes clear that no significant increase at the high frequency part of the spectrum occurs, so nonlinear attenuation of the high frequency side is mostly absent. Moreover, correlation and waveform analyses can be performed since the four microphones were acquired synchronously. At first, the temporal cross correlations were computed between the first ($60\ D_j$) and three subsequent microphones. The arrival times of the acoustic disturbances, in terms of distances, are presented in figure 24. High correlation coefficients are found, respectively, 0.77, 0.69 & 0.64, which demonstrates that no major distortion of the waveform occurs in this range, since that would have caused a more significant loss of linear coherence by expectancy (Ffowcs

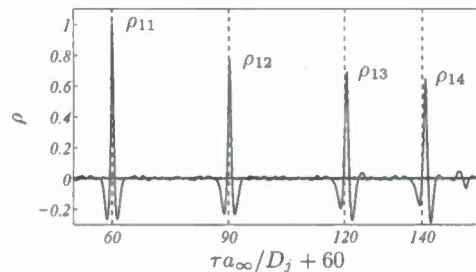Nonlinear distortion of acoustic waveforms from high-speed jets 31

FIGURE 24. The temporal cross correlation coefficient between the first and subsequent microphones on the line-array.
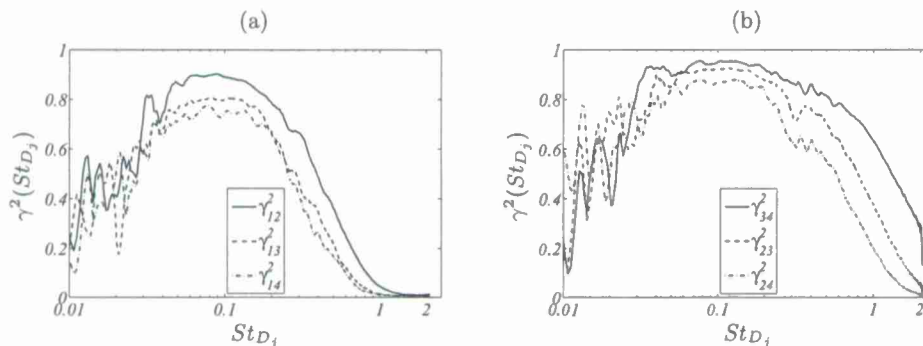
FIGURE 25. Linear coherence spectra between the microphones on the line-array (5% bandwidth moving filter applied).

Williams *et al.* 1975). Likewise, linear coherence between the transducers are presented in figure 25(*a,b*) to illustrate the band of frequencies over which acoustic waveforms remain strongly correlated.

6.2. *Metrics for quantifying nonlinearities*

6.2.1. *Definitions with examples*

Various off–the–shelf metrics have been used in the past to locally characterize the degree of nonlinearity in a waveform (Gallagher 1982). This, again, is not to be confused with cumulative nonlinear waveform distortions as are discussed in § 5. Albeit, the spatial topography of these localized nonlinear indicators can be used to infer information about cumulative distortions in that region, as will be done here.

Both near– and far–field pressure waveforms that form from Mach waves are known to comprise sharp compressions, followed by more gradual expansions. The expansive part is less intense than the compressive counterpart which suggests that the PDF of the temporal pressure $B(p(t))$ and its temporal derivative $B(\dot{p}(t))$, are non-Gaussian. The third and fourth central moments are commonly used to characterize deviations in the waveform from a Gaussian and are most often presented in non-dimensional form as Skewness (S) and Kurtosis (K) factors, respectively. These metrics are defined as,

$$S(p) \equiv \frac{\overline{p^3}}{\sigma^3}, \tag{6.1}$$

$$K(p) \equiv \frac{\overline{p^4}}{\sigma^4}, \tag{6.2}$$

32   *W. J. Baars, C. E. Tinney and M. S. Wochner*

where σ is the variance of $p(t)$, and the third central moment is given by (Tennekes & Lumley 1972)

$$\overline{p^3} \equiv \int_{-\infty}^{\infty} p^3 B(p)\,dp. \tag{6.3}$$

For a Gaussian signal, $S = 0$ and $K = 3$. In a high intensity rocket noise study by McInerny (1996), it was shown how the statistics of the pressure gradient are more sensitive indicators of the presence of shock like structures in the acoustic waveform. Henceforth, the Skewness and Kurtosis of the waveform derivative, denoted as $S(\dot{p})$ and $K(\dot{p})$, are considered important to this discussion.

Aside from employing classical statistical metrics, additional indicators are considered and include the wave steepening factor (WSF), the number of zero crossings (Z_c) and the Morfey-Howell indicator. The first of these is defined as the modulus of the average negative slope divided by the average positive slope in the waveform (Gallagher 1982). The range of WSF is thus $[0,1]$, where 1 corresponds to a pure harmonic wave and 0 to a perfect N wave. Where Z_c is concerned, it is known that in the absence of viscous absorption, stronger shock waves move faster in the waveform and merge or coalesce with weaker shocks and so the number of zero crossings per unit time of the temporal waveform will change. When shocks coalesce, a decrease of Z_c appears with propagation distance and is therefore a measure of a cumulative nonlinear propagation effect.

As for the Morfey-Howell indicator, this has become an increasingly popular approach in the jet noise community to those interested in studying cumulative nonlinear acoustic waveform distortions. Applications can be found in the literature and include the work of McInerny & Ölçmen (2005), Petitjean *et al.* (2006), Gee *et al.* (2007a) and Kuo *et al.* (2010). Originally derived by Morfey & Howell (1981), this indicator starts with the general from of the Burgers equation for spherically outgoing waves. This imposes a major limitation in that the results are only valid for *"propagation along a ray tube with arbitrary area variation"*, (Morfey & Howell 1981). Their first step was to obtain a statistical form of the Burgers equation:

$$\frac{\partial}{\partial r}\left[r^2 e^{2\alpha r} S_{pp}(r,f)\right] = -2\pi f \frac{\beta}{\rho_\infty c_\infty^3} e^{2\alpha r} Q_{p^2 p}(r,f), \tag{6.4}$$

where r is the coordinate along the propagation path, S_{pp} is the double-sided PSD of the pressure, and $Q_{p^2 p}$ is the quadrature spectral density; which is the imaginary part of the conjugated single-sided cross-spectral density between the pressure squared and the pressure (Bendat & Piersol 1980):

$$Q_{p^2 p}(f) = -\Im\left[2P_2(f)P^*(f)\right]. \tag{6.5}$$

Here, $P(f)$ and $P_2(f)$ are the Fourier transforms of the signals $p(t)$ and $p^2(t)$ respectively. The factor 2 accounts for the single-sided version of the PSD. The spatial rate of change of the PSD, involving a simple linear spreading concept and atmospheric absorption, appears on the left hand side of (6.4). This term would be zero in the case of linear spreading. A logical step forward is to argue that the right-hand side accounts for non-linear distortion of the spectrum (Morfey & Howell 1981). Thus, any nonlinear distortion must be the consequence of a non-zero value of the quadrature spectral density. In the case of a positive right-hand side (for certain frequencies), the PSD on the left-hand side gains energy in that frequency band due to nonlinear distortion, and vice versa for a negative right-hand side. (6.4) can be thought of as being analysed between two points (Δr apart from each other) on a propagation path. In practice, the right-hand side is computed at a single point and so the left-hand side is the actual derivative at that point

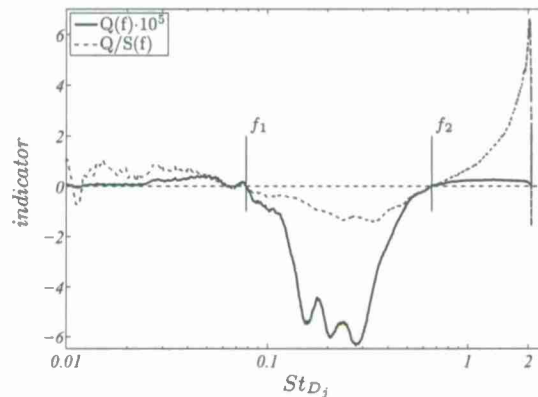*Nonlinear distortion of acoustic waveforms from high-speed jets*   33

FIGURE 26. The normalized quadrature spectral density Q and the Q/S Morfey-Howell indicator for arc-array microphone 5.

in the limit of small Δr. The actual forms of the single-point Morfey-Howell indicator are well outlined by Gee *et al.* (2007*a*). Here we choose to consider the normalized form of the quadrature spectral density,

$$Q(f) = \frac{Q_{p^2p}(f)}{p_{rms}^3}, \tag{6.6}$$

which has dimensions of 1/Hz. One of the most used forms of the indicator was introduced as 'Q/S' and uses the PSD to obtain a dimensionless quantity:

$$\frac{Q}{S}(f) = \frac{Q_{p^2p}(f)/p_{rms}^3}{S_{pp}(f)/p_{rms}^2}. \tag{6.7}$$

Once again, the indicator can only measure how the energy in the PSD is redistributed due to *cumulative* nonlinear distortion effects when multiple points on a spreading ray are analysed. As an example, Q and Q/S are demonstrated in figure 26 for arc-array microphone 5. The trends are relatively similar, as is expected given that S is positive-definite. However, Q/S increases quite significantly at higher frequencies due to roll-off of the PSD. Overall, both Q and Q/S exhibit the same features that are required of this study. Albeit, an exact interpretation of the amplitude of the indicator, as well as its physical meaning, has become problematic for those working with this technique (McInerny & Ölçmen 2005; Falco *et al.* 2006).

Before proceeding further, it is important to emphasize the nonlinear detection characteristics of this single-point indicator. Foremost, the quadrature spectral density Q_{p^2p} is zero for a truly Gaussian signal. This is assumed to be the case for the noise source in the above discussion. Therefore, when a Gaussian acoustic waveform propagates away from its source, it may distort and become non-Gaussian due to nonlinearities. The single-point Morfey-Howell indicator detects this as being non-zero and so one concludes that the waveform has undergone cumulative nonlinear distortion between the source region and observer location. However, no distinction can be made between *local* effects, *cumulative* effects, or a combination of the two based on a single-point measurement alone. If, for example, the noise source emits acoustic waves that are immediately non-Gaussian (local) but have not traveled far enough for them to have undergone any recognizable cumulative nonlinear distortion (they have essentially propagated linearly), the single-point Morfey-Howell indicator would, once again, be non-zero. And so, without any knowledge

34   *W. J. Baars, C. E. Tinney and M. S. Wochner*

of the nature of the starting waveform, it is inconclusive for one to make any distinction between *local* or *cumulative* nonlinear distortions based on a single-point estimate of the Morfey-Howell indicator. It is further pointed out that the quadrature spectral density is highly sensitive to deviations from a Gaussian, which may be an unavoidable consequence of instrument errors or the averaging process.

To demonstrate this, an arbitrarily chosen, and experimentally acquired, waveform is selected from our jet noise database and is then projected to several observer positions using the generalized Burgers equation. The process for doing this is described in § 2.2 following the work of Pestorius & Blackstock (1974). Four of the projected waveforms $p(t)$ at $r = [4, 6, 8, 10]$m are shown in figure 27(a,b) along with the original input waveform $(r = 3$m$)$ and corresponding time derivatives $\dot{p}(t)$; derivatives are computed using a first–order forward difference routine. PSDs, quadrature spectral densities and the Morfey-Howell indicator of these projected waveforms are then computed and are shown in figure 28(a,b,c) with comparisons to the input waveform at $r = 3$m (identified by a dashed line in each figure). Statistical attributes of the evolving waveform and its temporal derivative, are scrutinized by way of its PDF, Skewness and Kurtosis, and are listed in table 6. Other metrics such as the WSF and the number of zero crossings, are provided for inspection. The generalized Burgers equation is applied under typical atmospheric conditions ($T_\infty = 288$ K, $p_\infty = 1$ atm, RH $= 40\%$ $\rho_\infty = 1.226$ kg/m^3, $a_\infty = 340.2$ m/s, $f_0 = 1,200$ Hz, $\beta = 1.201$) and with a large source amplitude at r $= 3$ m ($p_{rms} = 582.4$ Pa, or 149.3 dB, $p_{ref} = 20\cdot10^{-6}$ Pa) to ensure sufficient waveform steepening. The algorithm assumes that the fluid is lossless (no viscous absorption) and plane wave propagation is used for practical purposes so that the resultant shock formation distance is estimated from (5.3) to be $\overline{x} = 9.2$ m.

In figure 27(a,b) the waveform is shown, as expected, to undergo wave steepening, shock formation and eventual coalescence with increasing distance from the source. The PDF of $p(t)$ shows negligible deviations from a Gaussian where as $\dot{p}(t)$ manifests deviations which increase significantly with increasing distance. As for the spectral behavior of the waveform in figure 28(a,b,c), shifts in energy from mid– to high–frequencies are observed and with crossover frequencies that also increase with increasing distance from the source. This upward shift in energy is a well known consequence of waveform steepening. Likewise, Q and Q/S for the input waveform are non-zero, thus demonstrating the acute sensitivity of these parameters to the PDF of the signal. This non-zero quadrature spectral density and Morfey-Howell indicator at the $d = 3$m observer position is a testament to the necessity of measuring these properties at several positions along the propagation path (as oppose to just one) if one is to accurately characterize the degree of cumulative nonlinear distortion to the far–field acoustics from jet flows, since the statistical nature of the source is most often unknown. Thus, a non-zero quadrature spectral density observed from a single–point measurement alone may inadvertently compel one to believe that a cumulative nonlinear distortion process is underway. A simple example is considered here to demonstrate this concept. Consider taking a sample signal from this jet study (e.g. the signal at position D_2 with non-zero Q and Q/S) to use as the source signal in a progressive plane wave tube experiment, like the ones used by Pestorius & Blackstock (1974) and Falco *et al.* (2006). If that input signal is played at a much lower amplitude, with the propagating waveform being measured at several distances from the source, then one should expect the same Q ands Q/S values to be observed even though the signal fails to possess the required amplitude to cause cumulative waveform steepening to occur. In experiments with known sources (like a progressive wave tube with a driver as was used by Pestorius & Blackstock (1974)), it is safe to use the indicator to detect wave steepening. However, when studying problems in jet noise, where the statistical na-

Nonlinear distortion of acoustic waveforms from high-speed jets   35

r [m]	$OASPL$ [dB]	$S(p)$	$S(\dot{p})$	$K(p)$	$K(\dot{p})$	WSF	$Z_c/10^3$ [s^{-1}]
3	149.3	0.095	2.529	3.062	19.25	0.669	9.913
4	148.7	0.037	7.438	2.930	92.50	0.433	9.113
6	147.5	-0.004	8.648	2.864	96.59	0.252	8.638
8	146.3	-0.010	8.790	2.895	97.03	0.201	8.517
10	145.2	-0.006	9.047	2.948	102.68	0.182	8.246

TABLE 5. Statistical properties of the raw and projected waveforms displayed in figure 27.

r [m]	$-Q_{neg}$ [–]	$-(Q/S)_{neg}/10^3$ [Hz]
3	0.072	1.156
4	0.139	2.196
6	0.196	3.204
8	0.220	3.440
10	0.235	3.426

TABLE 6. Metrics corresponding to the distances.

ture of the source is unknown, the spatial evolution of Q and Q/S should be considered, and so, a single-point indicator is insufficient due to the problematic interpretation of its amplitude.

Morfey & Howell (1981) have suggested that for aircraft noise prediction studies, it is preferred that one integrate Q/S along the propagation path in order to characterize the net flux of energy transfer. Here we have chosen to confine the limits of integration to the negative part of the quadrature spectral density as follows,

$$Q_{neg} = \int_{f_{neg}} Q(f)df, \tag{6.8}$$

$$(Q/S)_{neg} = \int_{f_{neg}} \frac{Q}{S}(f)df, \tag{6.9}$$

which, in practice, involves integrating from f_1 to f_2 in figure 26. Table 6 displays the results of applying (6.8) and (6.9) to the sample waveforms from figure 28. As expected, a clear change in the net flux is manifest which we owe to the cumulative nonlinear distortion of this sample waveform.

6.2.2. *Application to the far-field of the Mach 3 jet.*

Having now developed an understanding of how the quadrature spectral density and other statistical metrics are affected by cumulative nonlinear waveform distortions, the next logical step is to apply the same analysis methods to the current data set of our Mach 3 jet flow. It is important to note that the pressure time series of the current study were high-pass filtered at 400 Hz to assure that slow drifts in the microphone signal and equipment were not saturating any result of the Skewness and any other statistical metric. Figure 29 depict estimates of Q and Q/S from the microphone signals along spreading lines A to G as they emanate from the post potential core regions of the flow. It is clear that each spreading line exhibits a unique trend for both Q and Q/S and that they are most prevalent within the Mach cone. Therefore, large-scale turbulent mixing noise is responsible for producing local distortions to the waveform. Further, for a given

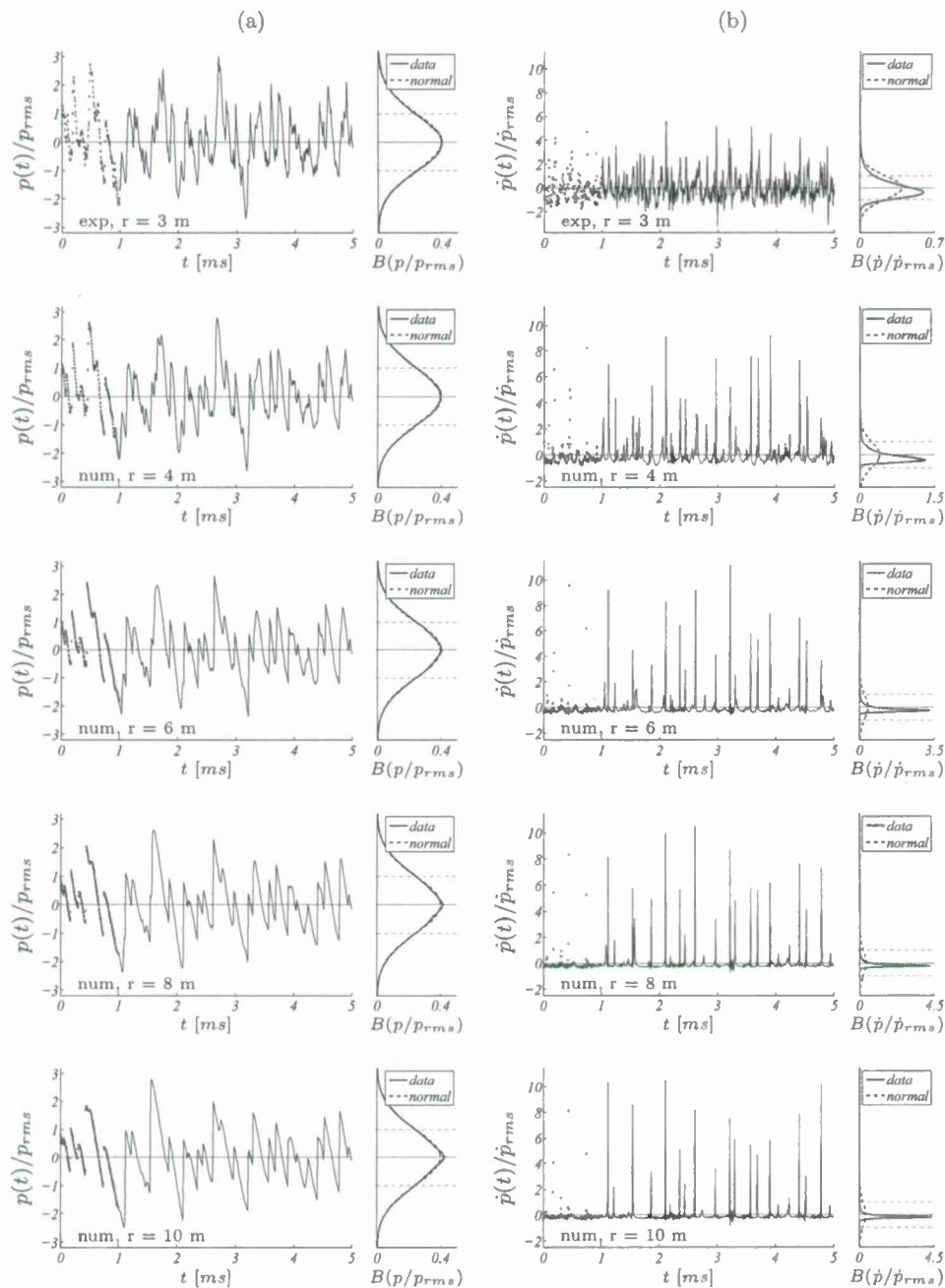36   *W. J. Baars, C. E. Tinney and M. S. Wochner*

FIGURE 27. Waveform projections using the generalized Burgers equation. (a) The raw waveform and (b) its temporal derivative.

Nonlinear distortion of acoustic waveforms from high-speed jets   37
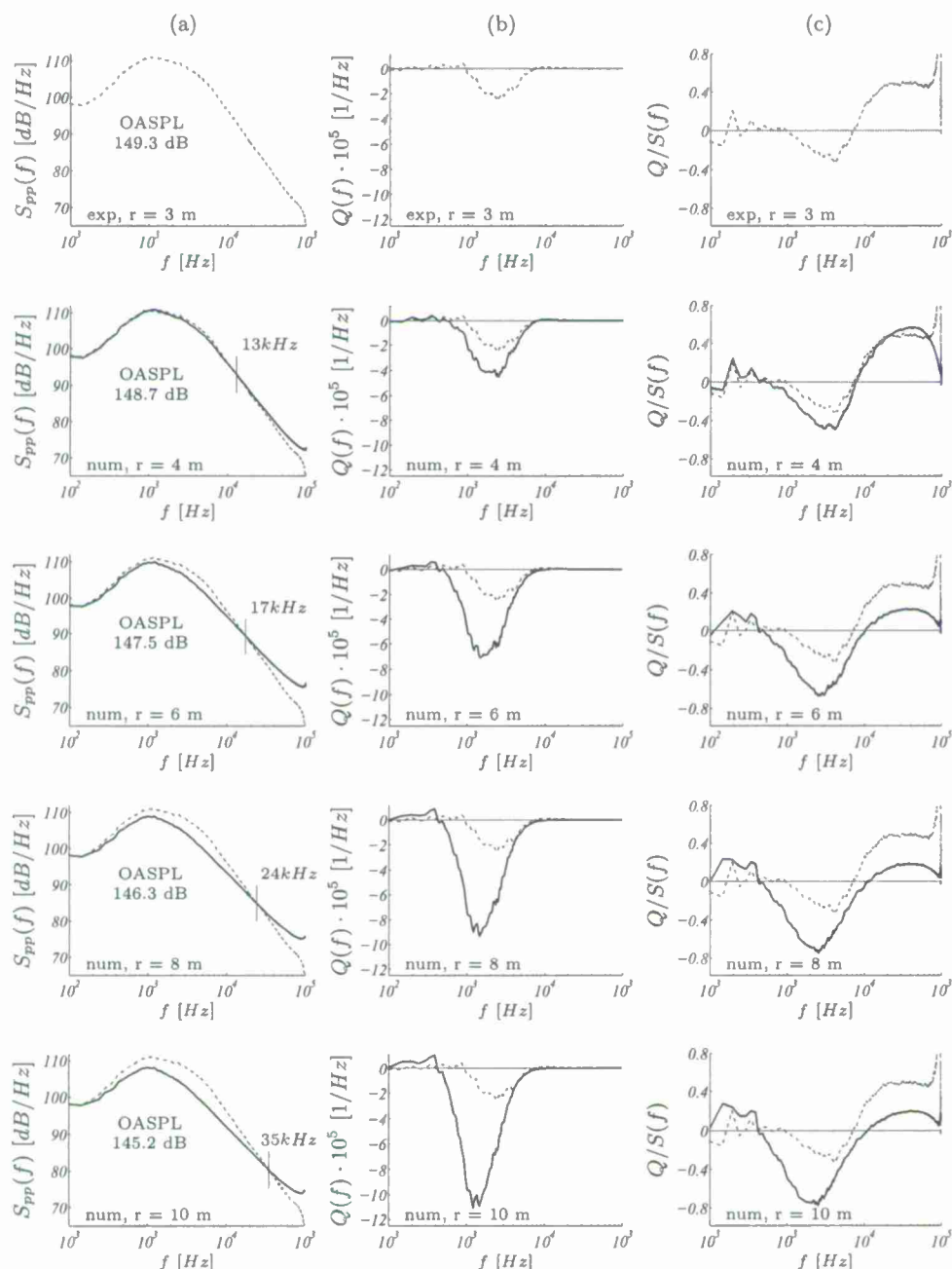

FIGURE 28. (a) PSD's, (b) normalized quadrature spectral density Q and (c) the Q/S Morfey-Howell indicator applied to the waveform data in figure 27.

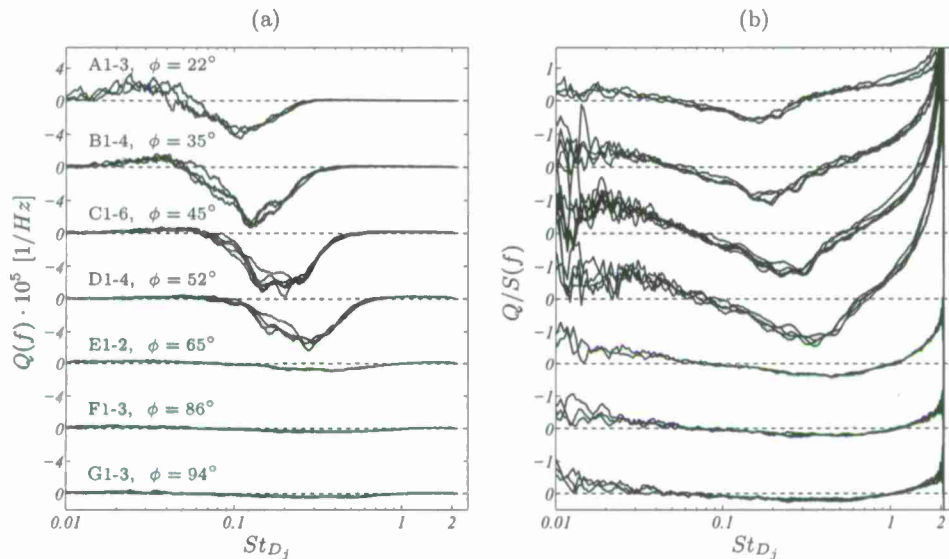38   *W. J. Baars, C. E. Tinney and M. S. Wochner*

FIGURE 29. (a) The quadrature spectral density, and (b) the normalized quadrature spectral density along the spreading lines A-G (5% bandwidth moving filter applied).

spreading line, the trends collapse quite well, which suggests that the propagation path has been correctly identified; had line H been chosen from figure 6, false conclusions would be formed regarding the presence of cumulative nonlinearities. Recall from figure 9 that the OASPL closely resembles a $1/r^2$ decay law along the peak OASPL path, and so, it is reasonable to assume that, on average, this is the correct propagation path. Contours of Q_{neg} from the Mach 3 jet data are also shown in figure 30; note that contours of $(Q/S)_{neg}$ result in a similar topography. The angle where maximum negative values reside is slightly steeper than the estimated Mach wave radiation angle, but continues along a path emanating from the post potential core regions of the flow.

From figures 29(a,b) and 30, a number of important conclusions can be made about the use of the Morfey-Howell indicator for characterizing either *local* or *cumulative* nonlinear distortions in the waveform. Negligible changes are observed in Q and Q/S over the propagation paths emanating from the post potential source region which suggests that if the waveform is undergoing cumulative distortions, the process is very slow in forming and that the shock formation distance is much further out than our farthest measurement. This provides proof that earlier estimates for the shock formation distance are indeed correct; our model estimates $\overline{r}_L = 18.1$ m and $\Gamma_L = 21.3$ for a source size of $s = 2.5$ D$_j$. While our measurements extend to 140 D$_j$ from the source, they are still confined by the restrictions of the chamber walls which only extend to about 3.5 m; this is approximately 20% of the estimated shock formation distance. This is an important finding in that it suggests that no measurable *cumulative* nonlinear distortions are present in our travelling acoustic waveform even though single-point Q and Q/S indicators are non-zero.

Contours of the Skewness of the pressure time series, Skewness of the pressure time derivative, and the WSF are shown in figures 31, 32 and 33, respectively. The contour levels have been normalized according to the equations provided in the captions, so that their range falls between 0 and 10. Likewise, a higher number indicates more nonlinearities in the waveform, or shock-type structures in the waveform. The topography of these

Nonlinear distortion of acoustic waveforms from high-speed jets   39
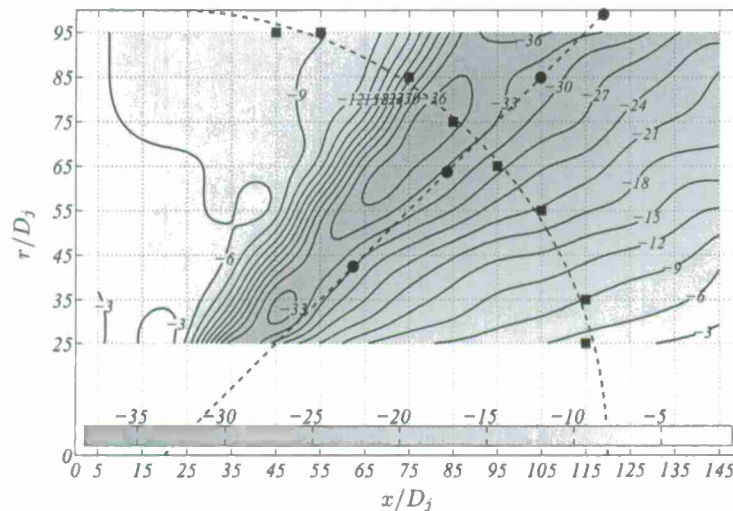
FIGURE 30. Contour of the quantity $Q_{neg} \cdot 10^2$, defined in (6.8).

metrics indicate how waveform steepening is most extreme along the Mach wave radiation angle with lines closely aligned with the direction of highest sound intensity. A steep inclination is observed for all criteria which resembles the trend observed for the OASPL (figure 8). Although the trends are globally similar for all criteria, differences reside in the location of the peak values. Maximum nonlinearity occurs upstream of the line-array according to the WSF and $S(p)$ criteria and downstream for the $S(\dot{p})$ criterion. The physical relevance of the nodes are questionable given the proximity of the chamber wall and wind tunnel collector to these measurement locations. PDF's of the pressure time series for each of the arc-array microphones are presented in figure 34 for the readers perusal. A normal distribution has been included for comparison and indicates that the pressure waveforms are near Gaussian, as is indicated by the relatively low Skewness values. Subsequently, the PDF's of the pressure time derivative along the arc-array are shown in figure 35; the PDF's are highly skewed for non-sideline angles. This clearly indicates that the Skewness of the pressure derivative is more sensitive to these nonlinear, shock-type waveform structures, as was also observed by Gee *et al.* (2007*b*) and McInerny (1996).

The final nonlinearity indicator that we consider in this study, the number of zero crossings per unit time (Z_c), is presented in normalized form in figure 36*(a,b)*. A high-pass frequency filter of 300 Hz was applied to the data to increase the accuracy of these estimates. The end result is very similar to an inverse contour of the low frequency content (e.g. figure 13*a*). Low frequency signals have simply fewer zero crossings than signals dominated by high frequencies, and so this finding is not surprising. Nonetheless, an interesting conclusion can be made. Figure 36*(b)* portrays zero-crossing contours aligned with spherically spreading paths originating from $x = 17.5$ D_j where our post-potential source is assumed to reside. This implies an absence of shock coalescence along the propagation paths for the relatively small range considered (in terms of typical distances over which shock coalescence occurs). And so, aside from the lack of observable waveform steepening, shock coalescence is also absent in our measurement range. Petitjean & McLaughlin (2003) found a decrease in Z_c along a line-array angled at 35° to the jet

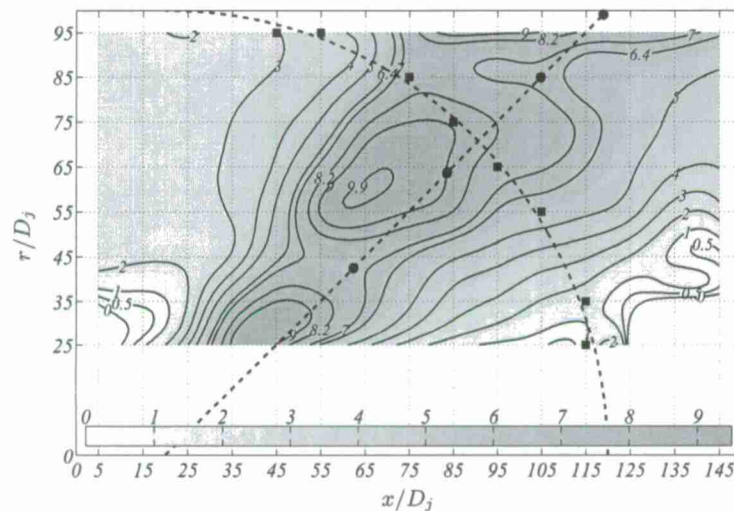40   *W. J. Baars, C. E. Tinney and M. S. Wochner*

FIGURE 31. Contour of the normalized Skewness of the pressure time series, $S(p)/S(p)_{max} \times 10$, where $S(p)_{max} = 0.47$ at position $(x,r)/D_j = (75,65)$. The contours of $S(p) = 0.3$ (contour line 6.4) and $S(p) = 0.4$ (contour line 8.2) are indicated as well.
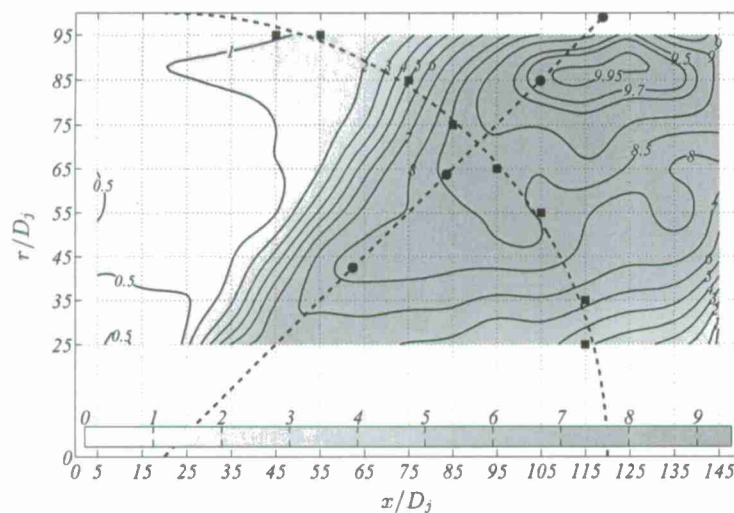
FIGURE 32. Contour of the normalized Skewness of the pressure time derivative, $S(\dot{p})/S(\dot{p})_{max} \times 10$, where $S(\dot{p})_{max} = 1.96$ at position $(x,r)/D_j = (115,85)$.

axis and emanating from the jet exit plane. Both a cold jet ($M_j = 1.5$, $T_j/T_\infty = 0.69$) and heat-simulated jet ($M_j = 1.5$, $T_j/T_\infty = 2.50$) were investigated with the same arrangement of instruments. The Mach wave radiation angle for that study is estimated to be 60° for the cold case and 75° for the heat-simulated case. It is postulated that the line-array positions at which Z_c is determined is crossing over several different contour lines. Henceforth, a decrease in Z_c might not have been observed for a propagation path

Nonlinear distortion of acoustic waveforms from high-speed jets   41

FIGURE 33. Contour of the normalized Wave Steepening Factor (WSF),
$(1 - WSF) / (1 - WSF)_{max} \times 10$, where $(1 - WSF)_{max} = 0.36$ at position
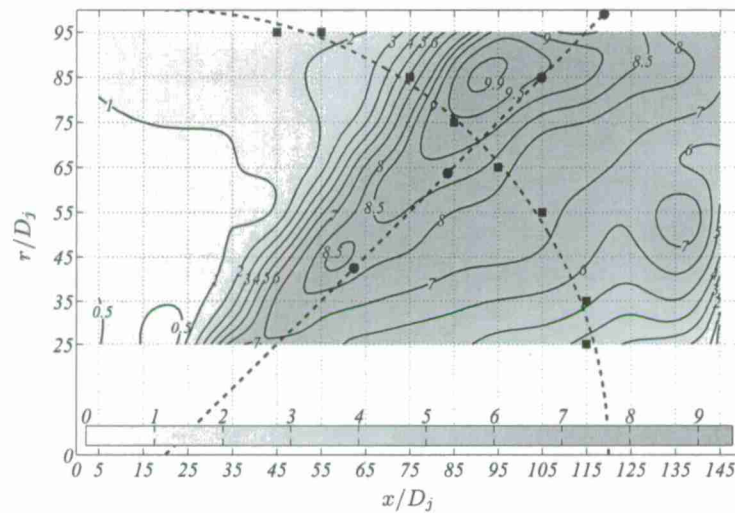$(x, r) / D_j = (95, 85)$.
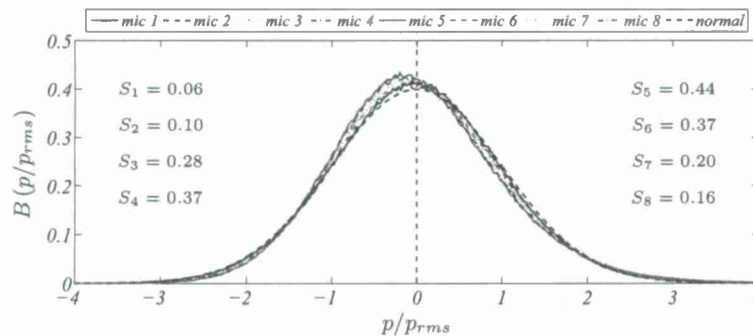
FIGURE 34. Probability Density Function (PDF) of the pressure time series for each of the microphones on the artificial arc-array. The skewness values are indicated in the graph. A normal distribution is shown for reference.

along lines emanating from the post-potential core region of the flow. A summary of these nonlinear indicators along the arc-array is listed in table 7 for reference.

6.3. *Waveform analysis*

Here we apply the generalized Burgers equation described in described in § 2 to acoustic waveforms captured along our line–array. This follows the same approach taken by Ffowcs Williams *et al.* (1975) (see p. 258). In that study, Professor D. T. Blackstock applied the generalized Burgers equation (Pestorius & Blackstock 1974) to near-field acoustic data (provided by Ffowcs Williams from a full-scale jet engine) and propagated it outward to an observer far away from the jet. Blackstock concluded that the amplitude of the waveform was too low to cause any nonlinear distortion, and that the distance needed for nonlinear effects to take place was much larger than the measurement range provided from

42   *W. J. Baars, C. E. Tinney and M. S. Wochner*
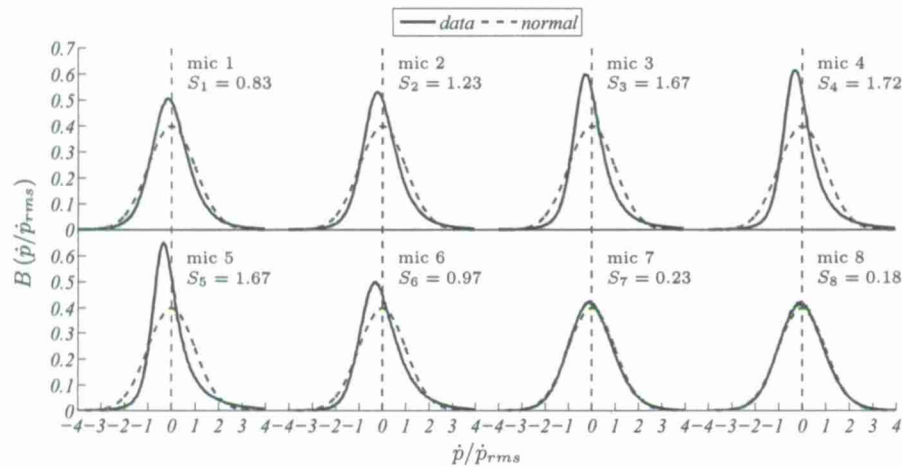
FIGURE 35. Probability Density Function (PDF), the respective skewness value, and the corresponding normal distribution of the pressure time derivative for each of the arc-array microphones.
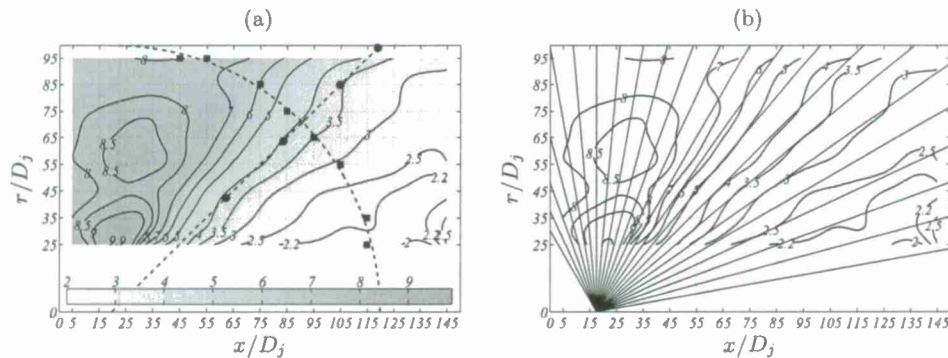
FIGURE 36. (a) Contour of the normalized number of zero crossings, $Z_c/Z_{c_{max}} \times 10$, where $Z_{c_{max}} = 4.25 \cdot 10^4 s^{-1}$ at position $(x, r)/D_j = (25, 25)$. (b) Spherical rays spreading from $(x, r)/D_j = (17.5, 0)$ lining up with lines of constant number of zero crossings.

mic #	$OASPL$ [dB]	$S(p)$	$S(\dot{p})$	WSF	$Z_c \cdot 10^{-3}$ [s^{-1}]
1	129.5	0.047	0.828	0.867	8.930
2	130.9	0.069	1.234	0.812	9.460
3	133.8	0.281	1.657	0.736	12.43
4	135.5	0.371	1.720	0.697	14.93
5	135.4	0.435	1.673	0.657	18.97
6	131.6	0.371	0.973	0.778	25.35
7	125.5	0.177	0.231	0.941	33.07
8	124.7	0.144	0.177	0.956	34.15

TABLE 7. Metrics corresponding to the microphones on the artificial arc-array.

FIGURE 37. (a) PSD's of the linear and nonlinear predicted time series at $\rho/D_j = 140$ and the PSD's of the input waveform at $\rho/D_j = 60$. (b) Comparison of the predicted and measured PSD's at location $\rho/D_j = 140$ (5% bandwidth moving filter applied).

the experiment. We will show similar conclusions to those found in the study described by Ffowcs Williams *et al.* (1975) which will lend additional support to the credibility of the model proposed in § 5.2 for predicting the presence, or lack thereof, of cumulative nonlinear distortions in the acoustic waveform produced by high speed jets.

In order to improve the accuracy of the predicted signal using the generalized Burgers equation, the acoustic waveform should propagate as a 1D beam (a waveguide so to speak). Given the highly directive nature of the sound field produced by this Mach 3 jet flow, it is reasonable to consider the sound propagating along the Mach wave radiation angle as a waveguide. In our application, the time waveform recorded at $\rho = 60~D_j$ is used as the input to the hybrid time-frequency algorithm. As a result, the temporal pressure waveform at an outward distance is sequentially computed by solving both the generalized, nonlinear Burgers equation and then the linearized Burgers equation. The results of this are shown in figure 37(a) by comparing spectra from linear and nonlinear predictions of the waveform at $\rho = 140~D_j$ to the original (experimentally acquired) signal at $60~D_j$. As expected, the linear prediction is qualitatively very similar to the input spectra since the linear propagation model simply applies geometrical spreading, absorption and dispersion losses. In figure 37(b), a direct comparison between the predicted and measured spectra at $140~D_j$ is shown. Differences between the measured spectra and the nonlinear prediction are found to reside in the higher frequencies ($St_{D_j} > 1.25$ or $f > 30$ kHz) and suggest that either wave steepening occurred in the 60–$140~D_j$ range, or that the measurement system is incapable of accurately resolving the higher frequencies being predicted by the algorithm (see § 3.2 for details concerning the experiment). It will become apparent in the following discussion that these differences are attributed to restrictions with the instruments and data acquisition system.

A comparison between the measured and predicted temporal waveforms are presented here for discussion. An experimentally acquired input waveform at $60~D_j$ is compared with its linear prediction at $140~D_j$ in figure 38(a), and then to its nonlinear prediction at $140~D_j$ in figure 38(b). Peaks and valleys appear to coincide with one another between the experimental and predicted waveforms; the nonlinear model expresses wave steepening

44   *W. J. Baars, C. E. Tinney and M. S. Wochner*
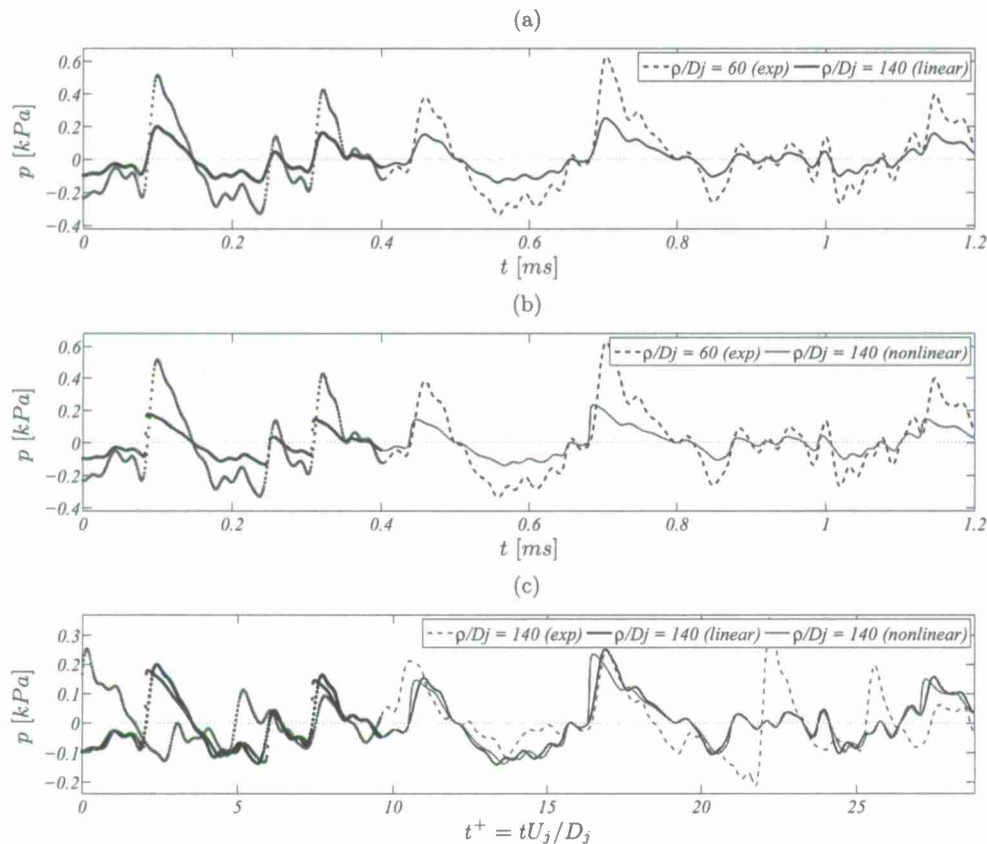
(a)

(b)

(c)

FIGURE 38. (a) & (b) Temporal pressure waveforms of the experimental input signal and the linear and nonlinear predictions at $\rho/D_j = 140$ respectively. (c) Comparison of the temporal pressure waveform (experiment versus predictions) at $\rho/D_j = 140$ (waveforms were lined up using temporal correlation peak). *Note: the time discretization is visualized for $t < 0.4ms$.*

effects not found in the linear prediction due to spreading and absorption. Albeit, over the short propagation distance considered here (2032 mm), geometric spreading and atmospheric absorption losses and dispersion appear less significant, and generally the effect is simply a decrease in pressure amplitude. In figure 38(c), a direct comparison is made between the linear and nonlinear predictions and the experimentally acquired waveform at 140 D_j. The experimental waveforms at 60 D_j and 140 D_j were acquired synchronously with a time shift, based on $80D_j/a_\infty^{-1}$, being used to align the data. At $t^+ \sim$ 17, the linear prediction produces a closer match than the nonlinear prediction. Likewise, distortions in the nonlinear prediction over the linear prediction are more significant for higher amplitude peaks and is expected due to the higher particle velocities. A peak in the experimental waveform is observed around $t^+ \sim 22$, and is likely due to an acoustic waveform propagating from a different source location not captured by the microphone at the 60 D_j position. The algorithm used to implement the generalized Burgers equation assumes that all energy is propagating spherically outward from the input time waveform position. It is evident from the differences in the experimental and predicted waveforms

Nonlinear distortion of acoustic waveforms from high-speed jets   45

in figure 38(c) that not all of the acoustic waves passing over the 140 D_j observer are being generated by the same source.

7. Summary & Conclusions

The acoustic field of an unheated and perfectly expanded Mach 3 jet flow was examined to understand the degree of local and cumulative nonlinear waveform distortion of sound produced by high speed jets. The source mechanisms of interest are those produced by the formation of Mach waves, which become pronounced as the convective speed of the large scale events in the shear layer move at supersonic speeds relative to the ambient surroundings. The resultant sound field forms a highly directive pattern with a ridge that follows along the Mach cone half angle of the jet. The source of this noise is shown to emanate from a region confined to boundaries defined by the potential core and supersonic core lengths.

A model for predicting the formation of cumulative nonlinear distortions to the acoustic waveform produced by jet flows is then proposed based on an assessment of the effective Gol'dberg number: a ratio of shock formation distance to acoustic absorption length. Relevant scaling parameters are shown to comprise Mach number (gas dynamic or acoustic), temperature ratio, and Strouhal number of the peak frequency residing along the propagation path. This model assumes the size of the spherical source to scale with nozzle diameter. Laboratory scale measurements of the Mach 3 jet flow are used in conjunction with full-scale engine tests of Gee *et al.* (2012) to justify the findings produced by this model. Two different scaling scenarios are then presented for the practicing scientist to choose from. The first of these allows shock formation distance to be preserved between laboratory and full-scale conditions based on a geometric scaling of the shock formation distance to nozzle diameter. The second scenario allows one to preserve the wave steepening process between laboratory and full-scale conditions based on a match of the effective Gol'dberg number. Both methods provide promising results upon application of the laboratory and full-scale experimental data sets.

There are, of course, several opportunities in which one may improve upon this model by developing a more thorough assessment of how jet exit conditions affect scaling parameters. Where Strouhal number is concerned, it is still unclear how the peak frequency along the dominant sound propagation path depends on jet exit conditions such as temperature ratio or Mach number. It is also assumed here that the source size scales with nozzle diameter only. This overhasty assumption disregards the dependence of the source size on Mach number, Reynolds number, temperature ratio, or even the operating state of the nozzle (overexpanded or underexpanded). For overexpanded and underexpanded jet flows, broadband shock noise is saturated by turbulent mixing noise along shallow angles to the jet axis (within the Mach cone of the jet) so measurable distortions to the acoustic waveform are still anticipate for supersonic jets operating under off-design conditions so long as the effective Gol'dberg number is shown to be sufficiently large. Deficiencies in our understanding of these dependencies would be alleviated by accurate parametrization of the effects of Strouhal number and source size on Mach number, temperature ratio and Reynolds number. Finally, and most importantly, it is unclear to what effect a pre-steepened acoustic waveform has on shock formation distance. Waveform steepening occurs when the wave amplitude is large enough to overcome viscous absorption. This requires a large source intensity and hence, a large Mach number at the exit. This suggests that cumulative nonlinear acoustic distortions are unlikely to occur under subsonic jet exit conditions. Albeit, viscous absorption is considerably weaker at low frequencies, and so it is still plausible for a geometrically large subsonic flow to produce acoustic waves

46 *W. J. Baars, C. E. Tinney and M. S. Wochner*

capable of undergoing cumulative nonlinear distortions. Nevertheless, Mach waves that develop in supersonic jet flows produce pre-steepened waveforms at the source that take on the shape of N-waves which can accelerate the wave steepening process and shorten the shock formation distance. A carefully documented execution of the generalized Burgers equation using pre-steepened waveforms could provide some useful answers to this last concern.

Temporal waveforms from the Mach 3 jet study are then examined using various statistical metrics including Skewness, Kurtosis, wave steepening factor, the number of zero crossings and the Morfey-Howell nonlinearity indicator. Where the Morfey-Howell indicator is concerned, it is concluded that its spatial evolution, along a path resembling a $1/r^2$ decay law, should only be considered due to the problematic interpretation of its amplitude as well as the highly directive nature of the sound field produced by jets. This is especially important for problems in jet noise where the statistical nature of the source term is unknown.

REFERENCES

BAARS, W. J., TINNEY, C. E., MURRAY, N. E., JANSEN, B. J. & PANICKAR, P. 2011 The effect of heat on turbulent mixing noise in supersonic jets. In *49th Aerospace Sciences Meeting and Exhibit*. Orlando, FL: AIAA.

BAARS, W. J., TINNEY, C. E. & POWERS, E. J. 2010 Pod based spectral higher-order stochastic estimation. In *48th Aerospace Sciences Meeting and Exhibit*. Orlando, FL: AIAA.

BENDAT, J. S. & PIERSOL, A. G. 1980 *Engineering applications of correlation and spectral analysis*. New York: Wiley.

BLACKSTOCK, DAVID T. 2000 *Fundamentals of Physical Acoustics*. New York: John Wiley & Sons, Inc.

CLEMENS, N. T. & PAUL, P. H. 1993 Mach waves radiating from a supersonic jet. *Phys. Fluids A.* **5** (9), S7.

DE CACQUERAY, N., BOGEY, C. & BAILLY, C. 2011*a* Investigation of a high-mach-number overexpanded jet using large-eddy simulation. *AIAA J.* **49** (10), 2171–2182.

DE CACQUERAY, N., BOGEY, C. & BAILLY, C. 2011*b* Investigation of high supersonic jet noise: non-linear propagation effects and flow-acoustics correlations. In *17th AIAA/CEAS Aeroacoustics Conference*. Portland, Oregon: AIAA.

FALCO, LAUREN E., ATCHLEY, ANTHONY A. & GEE, KENT L. 2006 Investigation of a single-point nonlinearity indicator in the propagation of high-amplitude jet noise. In *12th AIAA/CEAS Aeroacoustics Conference*. Cambridge, MA: AIAA.

FFOWCS WILLIAMS, J. E. 1963 The noise from turbulence convected at high speed. *Phil. Trans. R. Soc. Lond. A* **255**, 469–503.

FFOWCS WILLIAMS, J. E. & MAIDANIK, G. 1965 The mach wave field radiated by supersonic turbulent shear flows. *J. Fluid Mech.* **21**, 641–657.

FFOWCS WILLIAMS, J. E., SIMSON, J. & VIRCHIS, V. J. 1975 'Crackle': an annoying component of jet noise. *J. Fluid Mech.* **71**, 251–271.

Nonlinear distortion of acoustic waveforms from high-speed jets　　　47

Freund, J. B., Lele, S. K. & Moin, P. 2000 Numerical simulation of a mach 1.92 turbulent jet and its sound field. *AIAA J.* **38** (11), 2023–2031.

Gallagher, J. 1982 The effect of non-linear propagation in jet noise. In *20th Aerospace Sciences Meeting and Exhibit*. Orlando, FL: AIAA.

Gee, Kent L. 2005 Prediction of nonlinear jet noise propagation. PhD thesis, The Pennsylvania State University, State College, PA.

Gee, Kent L., Atchley, Anthony A., Falco, Lauren E., Gabrielson, Thomas B. & Sparrow, Victor W. 2005 Bispectral analysis of high-amplitude jet noise. In *11th AIAA/CEAS Aeroacoustics Conference*. Monterey, CA: AIAA.

Gee, K. L., Downing, J. M., James, M. M., McKinley, R. C., McKinley, Richard L., Neilsen, T. B. & Wall, A. T. 2012 Nonlinear evolution of noise from a military jet aircraft during ground run-up. In *18th AIAA/CEAS Aeroacoustics Conference*. Colorado Springs, CO: AIAA.

Gee, Kent L., Shepherd, Micah R., Falco, Lauren E., Atchley, Anthony A., Ukeiley, Lawrence S., Jansen, Bernard J. & Seiner, John M. 2007a Identification of nonlinear and near-field effects in jet noise using nonlinearity indicators. In *28th AIAA/CEAS Aeroacoustics Conference*. Rome, Italy: AIAA.

Gee, K. L., Sparrow, V. W., Atchley, A. & Gabrielson, T. B. 2007b On the perception of crackle in high-amplitude jet noise. *AIAA J.* **45** (3), 593–598.

Gee, Kent L., Sparrow, Victor W., James, Michael M., Downing, J. Micah, Hobbs, Christopher M., Gabrielson, Thomas B. & Atchley, Anthony A. 2008 The role of nonlinear effects in the propagation of noise from high-power jet aircraft. *J. of Acoustical Society of America* **123** (6), 4082–4092.

Greska, B., Krothapalli, A., Horne, W. C. & Burnside, N. 2008 A near-field study of high temperature supersonic jets. In *14th AIAA/CEAS Aeroacoustics Conference*. Vancouver, British Columbia, Canada: AIAA.

Greska, Brenton, Krothapalli, Anjaneyulu, Seiner, John M., Jansen, Bernard J. & Ukeiley, Lawrence 2005 The effects of microjet injection on an f404 jet engine. In *11th AIAA/CEAS Aeroacoustics Conference*. Monterey, CA: AIAA.

Hall, J. W., Hall, A. M., Pinier, J. T. & Glauser, M. N. 2009 Cross-spectral analysis of the pressure in a mach 0.85 turbulent jet. *AIAA J.* **47** (1), 54–59.

Hamilton, Mark F. & Blackstock, David T. 2008 *Nonlinear Acoustics*. Melville, NY: Acoustical Society of America.

Howell, G. P. & Morfey, C. L. 1987 Non-linear propagation of broadband noise signals. *J. Sound Vib.* **114** (2), 189–201.

Kerhervé, F., Fitzpatrick, J. & Jordan, P. 2006 The frequency dependence of jet turbulence for noise source modelling. *J. Sound Vib.* **296**, 209–225.

Kuo, Ching-Wen, Veltin, Jérémy & McLaughlin, Dennis K. 2010 Effects of jet noise source distribution on acoustic far-field measurements. In *48th Aerospace Sciences Meeting and Exhibit*. Orlando, FL: AIAA.

Laufer, J., Schlinker, R. & Kaplan, R. E. 1976 Experiments on supersonic jet noise. *AIAA J.* **14** (4).

McInerny, S. A. 1996 Launch vehicle acoustics part 2: Statistics of the time domain data. *J. of Aircraft* **33** (3), 518–523.

McInerny, S. A. & Ölçmen, S. M. 2005 High-intensity rocket noise: Nonlinear propagation, atmospheric absorption, and characterization. *J. of Acoustical Society of America* **117** (2), 578–591.

McLaughlin, Dennis K., Bridges, James E. & Kuo, Ching-Wen 2010 On the scaling of small, heat simulated jet noise measurements to moderate size exhaust jets. In *16th AIAA/CEAS Aeroacoustics Conference*. Stockholm, Sweden: AIAA.

McLaughlin, Dennis K., Morrison, Gerald L. & Troutt, Timothy R. 1975 Experiments on the instability waves in a supersonic jet and their acoustic radiation. *J. Fluid Mech.* **69**, 73–95.

Morfey, C. L. & Howell, G. P. 1981 Nonlinear propagation of aircraft noise in the atmosphere. *AIAA J.* **19** (8), 986–992.

Morris, P. J. 1977 Flow characteristics of the large scale wave-like structure of a supersonic round jet. *J. Sound Vib.* **53** (2), 223–244.

48   *W. J. Baars, C. E. Tinney and M. S. Wochner*

Morris, Philip J. 2009 A note on noise generation by large scale turbulent structures in subsonic and supersonic jets. *Intl J. Aeroacous* **8** (4), 301–316.

Morris, Philip J. & Farassat, F. 2002 Acoustic analogy and alternative theories for jet noise prediction. *AIAA J.* **40** (4), 671–680.

Nacamatsu, H. T. & Horvay, Gabriel 1970 Supersonic jet noise. In *8th Aerospace Sciences Meeting*. New York, NY: AIAA.

Norum, T. D. & Seiner, J. M. 1982 Broadband shock noise from supersonic jets. *AIAA J.* **20** (5), 68–73.

Papamoschou, D. & Debiasi, M. 1999 Noise measurements in supersonic jets treated with the mach wave elimination method. *AIAA J.* **37** (2), 154–160.

Papamoschou, D. & Debiasi, M. 2001 Directional suppression of noise from a high-speed jet. *AIAA J.* **39** (3), 380–387.

Papamoschou, Dimitri, Morris, Philip J. & McLaughlin, Dennis K. 2010 Beamformed flow-acoustic correlations in a supersonic jet. *AIAA J.* **48** (10), 2445–2453.

Pestorius, F. M. & Blackstock, D. T. 1974 Propagation of finite-amplitude noise. In *Finite-amplitude wave effects in fluids, Proceedings of the 1973 Symposium*.

Petitjean, B. P. & McLauchlin, Dennis K. 2003 Experiments on the nonlinear propagation of noise from supersonic jets. In *9th AIAA/CEAS Aeroacoustics Conference*. Hilton Head, SC: AIAA.

Petitjean, B. P., Viswanathan, K. & McLaughlin, D. K. 2006 Acoustic pressure waveforms measured in high speed jet noise experiencing nonlinear propagation. *Intl J. Aeroacous* **5** (2), 193–215.

Phillips, O. M. 1960 On the generation of sound by supersonic turbulent shear layers. *J. Fluid Mech.* **9**, 1–28.

Potter, R. C. & Crocker, M. J. 1966 Acoustic prediction methods for rocket engines, including the effects of clustered engines and deflected exhaust flow. Cr-566. NASA.

Saxena, Swati, Morris, Philip J. & Viswanathan, K. 2009 Algorithm for the nonlinear propagation of broadband jet noise. *AIAA J.* **47** (1), 186–194.

Seiner, John M., Bhat, Thonse R. S. & Ponton, Michael K. 1994 Mach wave emission from a high-temperature supersonic jet. *AIAA J.* **32** (12), 2345–2350.

Tam, Christopher K. W. 1995 Supersonic jet noise. *Annu. Rev. Fluid Mech.* **27**, 17–43.

Tam, Christopher K. W. 2009 Mach wave radiation from high-speed jets. *AIAA J.* **47** (10), 2440–2448.

Tam, Christopher K. W. & Chen, Ping 1994 Turbulent mixing noise from supersonic jets. *AIAA J.* **32** (9), 1774–1780.

Tam, Christopher K. W., Chen, Pinc & Seiner, J. M. 1992 Relationship between instability waves and noise of high-speed jets. *AIAA J.* **30** (7), 1747–1752.

Tam, Christopher K. W., Golebiowski, Michel & Seiner, J. M. 1996 On the two components of turbulent mixing noise from supersonic jets. In *2nd AIAA/CEAS Aeroacoustics Conference*. State College, PA: AIAA.

Tam, Christopher K. W. & Hu, Fang Q. 1989 On the three families of instability waves of high-speed jets. *J. Fluid Mech.* **201**, 447–483.

Tam, Christopher K. W., Pastouchenko, Nikolai N. & Viswanathan, K. 2005 Fine-scale turbulence noise from hot jets. *AIAA J.* **43** (8), 1675–1683.

Tam, Christopher K. W., Viswanathan, K., Ahuja, K. K. & Panda, J. 2008 The sources of jet noise: experimental evidence. *J. Fluid Mech.* **615**, 253–292.

Tanna, H. K. & Dean, P. D. 1975 The influence of temperature on shock-free supersonic jet noise. *J. Sound Vib.* **39** (4), 429–460.

Tennekes, H. & Lumley, J. L. 1972 *A First Course in Turbulence*. Cambridge, MA: The MIT Press.

Tick, Leo J. 1961 The estimation of "transfer functions" of quadratic systems. *Technometrics, IEEE* **3** (4), 563–567.

Tinney, C. E., Ukeiley, L. S. & Glauser, M. N. 2008 Low-dimensional characteristics of a transonic jet. part 2: Estimate and far-field prediction. *J. Fluid Mech.* **615**, 53–92.

Troutt, T. R. & McLauchlin, D. K. 1982 Experiments on the flow and acoustic properties of a moderate-reynolds-number supersonic jet. *J. Fluid Mech.* **116**, 123–156.

Nonlinear distortion of acoustic waveforms from high-speed jets   49

VARNIER, JEAN 2001 Experimental study and simulation of rocket engine freejet noise. *AIAA J.* **39** (10), 1851–1859.

VELTIN, J., DAY, BENJAMIN J. & MCLAUGHLIN, DENNIS K. 2011 Correlation of flowfield and acoustic field measurements in high-speed jets. *AIAA J.* **49** (1), 150–163.

VISWANATHAN, K. 2004 Aeroacoustics of hot jets. *J. Fluid Mech.* **516**, 39–82.

VISWANATHAN, K. 2006 Instrumentation considerations for accurate jet noise measurements. *AIAA J.* **44** (6), 1137–1149.

VISWANATHAN, K. 2008 Does a model-scale nozzle emit the same jet noise as a jet engine? *AIAA J.* **46** (2).

WITZE, PETER O. 1974 Centerline velocity decay of compressible free jets. *AIAA J.* **12** (4), 417–418.

1. REPORT DATE (DD-MM-YYYY)	2. REPORT TYPE	3. DATES COVERED (From - To)
11/15/2012	Interim Research Performance Report	8/1/2012 - 10/31/2012

4. TITLE AND SUBTITLE	5a. CONTRACT NUMBER
Interim Research Performance Report Quarterly Report No. 5	
	5b. GRANT NUMBER
	N00014-11-1-0752
	5c. PROGRAM ELEMENT NUMBER

6. AUTHOR(S)	5d. PROJECT NUMBER
Murray, Nathan E.	
	5e. TASK NUMBER
	5f. WORK UNIT NUMBER

7. PERFORMING ORGANIZATION NAME(S) AND ADDRESS(ES)	8. PERFORMING ORGANIZATION REPORT NUMBER
The University of Mississippi Jamie Whitten National Center for Physical Acoustics University, MS 38677	

9. SPONSORING/MONITORING AGENCY NAME(S) AND ADDRESS(ES)	10. SPONSOR/MONITOR'S ACRONYM(S)
Joseph Doychak Office of Naval Research 875 North Randolph Street Arlington, VA 22203-1995	ONR
	11. SPONSOR/MONITOR'S REPORT NUMBER(S)

12. DISTRIBUTION/AVAILABILITY STATEMENT
Approved for Public Release; Distribution is Unlimited

13. SUPPLEMENTARY NOTES
In collaboration with Charles Tinney (U. of Texas at Austin), Brian Thurow (Auburn Univ.), & Raj Sinha (CRAFT Tech)

14. ABSTRACT
Enhancements to the NCPA PIV seeding system were completed and PIV measurements were acquired on the jet centerline. Auburn supported a Plenopic PIV measurement of the jet. UT Austin submitted an abstract to the 2013 AIAA Aeroacoustics meeting discussing evaluation of noise source indicators. UT Austin submitted a manuscript to JFM on nonlinear distortion of the acoustic waveforms. CRAFT Tech made significant progress on completing the LES simulations and making the data available to the group. CRAFT Tech has made advancements in their beamforming framework. Finally, NCPA hosted ONR (B. Henderson), NASA (J. Bridges), and NAVAIR (A. Aubert) for a site visit.

15. SUBJECT TERMS
Jet Noise Reduction

16. SECURITY CLASSIFICATION OF:			17. LIMITATION OF ABSTRACT	18. NUMBER OF PAGES	19a. NAME OF RESPONSIBLE PERSON
a. REPORT	b. ABSTRACT	c. THIS PAGE			Nathan E. Murray
					19b. TELEPHONE NUMBER (include area code)
				121	662-915-3190